Master's thesis

NTNU
Norwegian University of Science and Technology
Faculty of Medicine and Health Sciences
Kavli Institute for Systems Neuroscience

Karoline Opsahl

# Assessing the Electrophysiological Functionality of Place Cells in TDG-depleted Hippocampus

Master's thesis in Neuroscience
Supervisor: Jing Ye
Co-supervisor: Magnar bjørns
May 2023

NTNU
Norwegian University of
Science and Technology

Karoline Opsahl

# Assessing the Electrophysiological Functionality of Place Cells in TDG-depleted Hippocampus

Master's thesis in Neuroscience
Supervisor: Jing Ye
Co-supervisor: Magnar bjørns
May 2023

Norwegian University of Science and Technology
Faculty of Medicine and Health Sciences
Kavli Institute for Systems Neuroscience

NTNU
Norwegian University of
Science and Technology

## Abstract

When exploring new environments, animals form spatial memories that are updated with experience and retrieved upon re-exposure to the same environment. Coordinated alternation of synaptic strength in the parahippocampal-hippocampal circuitry spatial cells is thought to provide a central neural substrate for this cognitive faculty. These structural changes in neuronal motifs are suggested to rely on the regulation of gene transcription for protein synthesis by coordination of DNA methylation and demethylation. The reported role of the DNA glycosylase, TDG, in demethylation suggests a possible involvement of TDG in long-term memory formation, as this type of memory is dependent on transcriptional regulation. This study investigates the potential effect of TDG-mediated DNA demethylation in hippocampal-dependent spatial memory. More specifically, this study aims to examine the potential impact of TDG on the proportional arrangement of CA1 spatial cells and the functional plasticity of CA1 place cells in a conditional Tdg knockout mouse model. This was assessed by the following procedures. (I) I constructed microdrives wired with four intracranial tetrodes, composing 16 electrodes. These were implanted in the mouse hippocampus. (II) Then I performed in vivo electrophysiological recording of cells in the hippocampal area CA1 in freely exploring mice. I recorded the activity of hippocampal cells in four animals (two control and two TDG-depleted). Place cells were subjected to in vivo global remapping and short-term and long-term stability experiments. (III) I sorted cells from all recorded mice by the Tint cluster cutting and analysis software. (IV) Lastly, I performed population analysis to identify spatial cells and analyzed the global remapping and stability capabilities of place cells. My results suggested that CA1 from the conditional Tdg knockout mice had a higher proportion of place cells but fewer speed cells than the control mice. TDG-depleted place cells displayed lower spatial information rate and firing rate on average, but the same amount of information content compared to the control cells. Furthermore, the TDG-depleted cells had lower specificity in terms of place field peak firing rate, but the number of place fields per cell and field size was invariable across genotypes. No deviances from normality were observed in global remapping capabilities, but the conditional Tdg knockout cells were more unstable both with 50 min and 24 h inter-trial intervals. These results suggest that the functionality of TDG-depleted CA1 place cells may deviate from the functionality of cells without TDG depletion. Cells from more animals ought to be included and evaluated to make a robust conclusion.

## Sammendrag

Når dyr utforsker nye omgivelser, dannes det romlige minner som oppdateres med erfaring og hentes frem igjen ved gjeneksponering for det samme miljøet. Koordinert modifikasjon av synaptisk styrke mellom de parahippocampale-hippocampale kretsenes spatiale celler antas å gi et sentralnevralt substrat for dette kognitive fakultetet. Disse strukturelle endringene i nevrale komposisjoner antydes å være avhengig av regulering av gentraskripsjon for proteinsyntese gjennom koordinering mellom DNA-metylering og demetylering. Den rapporterte rollen til DNA-glykosylasen, TDG, i demetylering insinuerer en mulig involvering av TDG i dannelse av langtidshukommelse, da denne typen hukommelse er avhengig av transkripsjonsregulering. Denne studien undersøker den potensielle effekten av TDG-mediert DNA-demetylering på hippocampus-avhengig spatial hukommelse. Mer spesifikt har denne studien som mål å undersøke den mulige innvirkningen av TDG på den proporsjonale fordelingen av plassceller i CA1 og deres funksjonelle plastisitet i en betinget *Tdg* knockout musemodell. Dette ble evaluert gjennom følgende prosedyrer. (I) Jeg konstruerte mikrodrivere med fire intrakranielle tetroder, som til sammen komponerte 16 elektroder. Disse ble implantert i musens hippocampus. (II) Deretter utførte jeg *in vivo* elektrofysiologisk opptak av celler i hippocampusområdet, CA1, hos fritt utforskende mus. Jeg registrerte aktiviteten til hippocampale celler i fire dyr (to kontroller og to TDG-reduserte). Spatiale celler ble underlagt *in vivo* global remapping og korttids og langtids stabilitetseksperimenter. (III) Jeg sorterte celler fra alle registrerte mus ved hjelp av klusterklippe- og analyseprogramvaren, Tint. (IV) Til slutt utførte jeg populasjonsanalyse for å identifisere spatiale celler og analyserte globale remapping- og stabilitetskapasiteten til plassceller. Resultatene mine impliserte at CA1 hos de betingede *Tdg* knockout-musene hadde en høyere andel plassceller, men færre hastighetsceller enn kontrollmusene. TDG-reduserte stedsceller viste lavere gjennomsnittlig romlig informasjonsrate og fyringsrate, men samme mengde informasjonsinnhold sammenlignet med kontrollcellene. Videre hadde TDG-reduserte celler lavere spesifisitet når det gjelder plassfeltenes toppfyringsrate, men antall stedsfelt per celle og feltstørrelse var konstant på tvers av genotyper. Ingen avvik fra normalitet ble observert i globale remapping-evner, men de betingede *Tdg*-knockout-cellene var mer ustabile både med 50 min og 24 timers mellomforsøksintervaller. Disse resultatene tyder på at funksjonaliteten til TDG-reduserte CA1-plassceller kan avvike fra funksjonaliteten til celler med normale mengder TDG. Celler fra flere mus bør inkluderes og evalueres for å kunne trekke en solid konklusjon.

## Acknowledgment

I would like to express my gratitude to my main supervisor, Jing Ye, for her invaluable guidance, support, and expertise throughout the entire research process. Further, I would like to thank my second supervisor, Magnar Bjørås for the resources to make this project possible. I would also like to thank all the members of the research group who made themselves available for questions and guidance in the lab. Especially thanks to Dagny Sanden Døskeland and Vidar Langseth Saasen for their help with training, writing and analysis, constant availability for questions and discussion, and overall support. I would also like to thank Liv Støldal Nielsen, my fellow associate, for her selfless encouragement, research cooperation, help with genotyping, and friendship through this process. I am also thankful to the faculty and staff of the Norwegian University of Science and Technology (NTNU), especially IKOM and CoMed for providing a conducive academic environment and resources for performing this project. Finally, I am very grateful to my friends and family for their unwavering support, understanding, and encouragement throughout this journey.

## Table of Contents

## List of Figures

## List of Tables

## List of Abbreviations

| | |
|---|---|
| 5caC | 5-carboxylcytosine |
| 5fC | 5-formylcytosine |
| 5hmC | 5-hydroxymethylcytosine |
| 5mC | 5-methylcytosine |
| AID | Activation induced deaminase |
| AMPA | ɑ-amino-3-hydroxy-5-methyl-4-isoxazolepropionic |
| APE I | Apurinic/apyrimidinic endonuclease I |
| BDNF | Brain-derived neurotrophic factor |
| BER | Base excision repair |
| C | Cytosine |
| CA | Cornu ammonis |
| CamKIIɑ | Calcium/Calmodulin-dependent protein kinase II alpha |
| CpGs | CpG dinucleotides |
| Cre | Cyclisation Recombination |
| DG | Dentate gyrus |
| DNA | Deoxyribo Nucleic Acid |
| DNMT | DNA methyltransferase |
| EC | Entorhinal cortex |
| G | Guanine |
| GABA | Gamma-amino-butyric acid |
| HCN1 | Cation nonselective 1 |
| HD | Head direction |
| HP | Hippocampus proper |
| LoxP | Locus of Crossover P1 |
| lMC | Lateral entorhinal cortex |
| LTD | Long-term depression |
| LTP | Long-term potentiation |
| mEC | Medial entorhinal cortex |
| mGluR5 | Metabotropic glutamate receptor 5 |
| MWM | Morris Water Maze |
| NMDA | N-metyl-D-aspartat |
| PaS | Parasubiculum |
| POR | Postrhinal cortex |
| PrS | Presubiculum |
| SAM | S-adenosyl-methionine |
| sl, | Stratum lucidum |
| slm | Stratum lacunosum moleculare |
| so | Stratum oriens |
| sp, | Stratum pyramidale |
| sr, | Stratum radiatum |
| STDP | Spike-timing-dependent plasticity |
| Sub | Subiculum |
| T | Thymine |
| TDG | Thymine DNA Glycosylase (mouse protein; human protein) |
| *Tdg* | Thymine DNA Glycosylase (mouse gene) |
| *TDG* | Thymine DNA Glycosylase (human gene) |
| TET | Ten-eleven translocase |
| UDG | Uracil DNA glycosylase |

## 1 Introduction

A characteristic feature of human cognition is the capacity to reconstruct perceptual experiences into mental representations, which allows for the ability to envision past events (Tulving, 1985) as well as to strategize for future scenarios (Schacter et al., 2007). The ability to retain and retrieve these cognitive constructs is referred to as episodic memory. Episodic memory is defined as the capacity to store and recall events within a spatiotemporal context (Sugar & Moser, 2019). The neural code supporting representations of episodic memories should meet certain requirements, including information about the position of the agent, the spatial component of an event. This ability depends upon delicately altered intrinsic and extrinsic neural compositions with direct correlates to the hippocampal formation and its neighboring structures. Spatial correlates of this anatomical area and the activity of individual neurons have been extensively reported in rodents (O'Keefe & Dostrovsky, 1971; Taube et al., 1990; Hafting et al., 2005) as well as in humans (Ekstrom et al., 2003; Chai & Jacobs, 2010). The genetic expression of the neural environment seems to contribute to this fine-tuned architecture of experience-dependent alternations in synaptic strength, known as synaptic plasticity (Poon, Tse & Lim, 2020). Plastic changes in neuronal motifs are suggested to rely on the regulation of gene transcription for protein synthesis by precise coordination of DNA methylation and demethylation (Yu et al. 2011). The evident role of Thymine DNA Glycosylase (TDG) in initiating active demethylation is by recognizing and excising 5-methylcytosine (5mC) from DNA (Bochtler et al., 2016). This essential removal of the outward projecting methyl group acting as a steric interference for transcription suggests a potential contribution of TDG in formation of long-term spatial memory reliant on transcriptional regulation. Understanding epigenetic adaptive modifications in gene expression could thus be fundamental for comprehending the genetic basis of behavior and cognitive abilities. This project aims to assess the role of DNA demethylation mediated by TDG in hippocampal-dependent spatial reference memory.

In this introduction, I will first give an overview of the parahippocampal-hippocampal network, mainly focusing on the CA1, followed by an elaboration of the several spatial cells located in this brain region. This section will focus on the functionality of place cell. Thereafter, I will introduce the synaptic alternations known to provide the neural substrate of spatial memory, mainly addressing homosynaptic long-term potentiation (LTP). An outline of the epigenetic mechanisms of DNA methylation and demethylation and its suggested function in spatial memory will then be described. Finally, the main objectives and research questions of this project will be presented.

## 1.1 The Hippocampus – Anatomical Overview

The parahippocampal-hippocampal network is a complex formation of brain regions in the medial temporal lobe (Figure 1). The region is thought to be involved in the formation and retrieval of memories, particularly those related to spatial and contextual information (Tatu & Vuillier, 2014). The network composes two main structures: the parahippocampal cortex and the hippocampus (Figure 1A). The defining distinctions between the two anatomical structures are the number of present cortical layers and the overall principles of neural connectivity. The parahippocampal-hippocampal circuitry is extensively studied in rodents, but the structures appear highly evolutionary conserved across mammalian species (Witter et al., 2006).

### 1.1.1 Anatomy of the Hippocampal Formation

The hippocampal formation of the mouse is an elongated convex structure located in the temporal lobes of the brain. The structure extends from the septal nuclei of the basal forebrain rostro-dorsally, around the diencephalon, and into the temporal brain regions caudoventrally (Figure 1; Witter, 2012). This long axis, with its dorsal pole situated dorsally and rostrally, is referred to as the dorsoventral or radial axis, and its orthogonal axis is the transverse axis (Figure 1C). The hippocampal formation comprises several structures, such as the hippocampus proper (HP), the dentate gyrus (DG), and the subiculum (Figure 1B; Tatu & Vuillier, 2014; Knierim, 2015; Donkelaar et al., 2018).

The HP forms a medially oriented curve at its most rostral tip (Dekeyzer et al., 2017). This distinctive curved shape is commonly termed 'Cornu ammonis' (CA) (Knierim, 2015). This general layout holds over the full range of mammalian species. From a sagittal section, the HP is subdivided into three zones designated CA1-3 (Figure 1B). The borders of these fields can be reliably established based on chemoarchitectural features (Lein et al., 2004; Thompson et al., 2008). The CA1, the largest of the three areas, is bordered laterally by the presubiculum and medially by the CA2. Area CA2 is situated towards the DG and delimited laterally by the CA1 and medially by the CA3. Finally, the CA3 is directed towards the DG hilus and is bordered by the CA2 medially. The subiculum is situated between the HP and the entorhinal cortex (EC) (Witter, 2006). And lastly, the DG, a narrow crenated band of grey matter, is located between the fimbria hippocampi and the parahippocampal gyrus (Witter, 2006).

### 1.2.2 Anatomy of the Parahippocampal Formation

The parahippocampal composition forms the most ventral and caudal portion of the cortical mantle, wrapping around the hippocampal formation's most caudal and ventral parts (Figure 1A; Witter, 2012). In the mouse, this cortical region composes the ventroposterior convexity of the cerebral hemisphere (Witter, 2012). The parahippocampal region comprises the perirhinal, entorhinal, and postrhinal cortices, as well as the presubiculum and parasubiculum (Figure 1A; Andersen et al., 2006). Of these, is the EC the region with the most connections with the hippocampal formation, in addition to forming robust connections with other parahippocampal sub-regions (Witter, 2012).

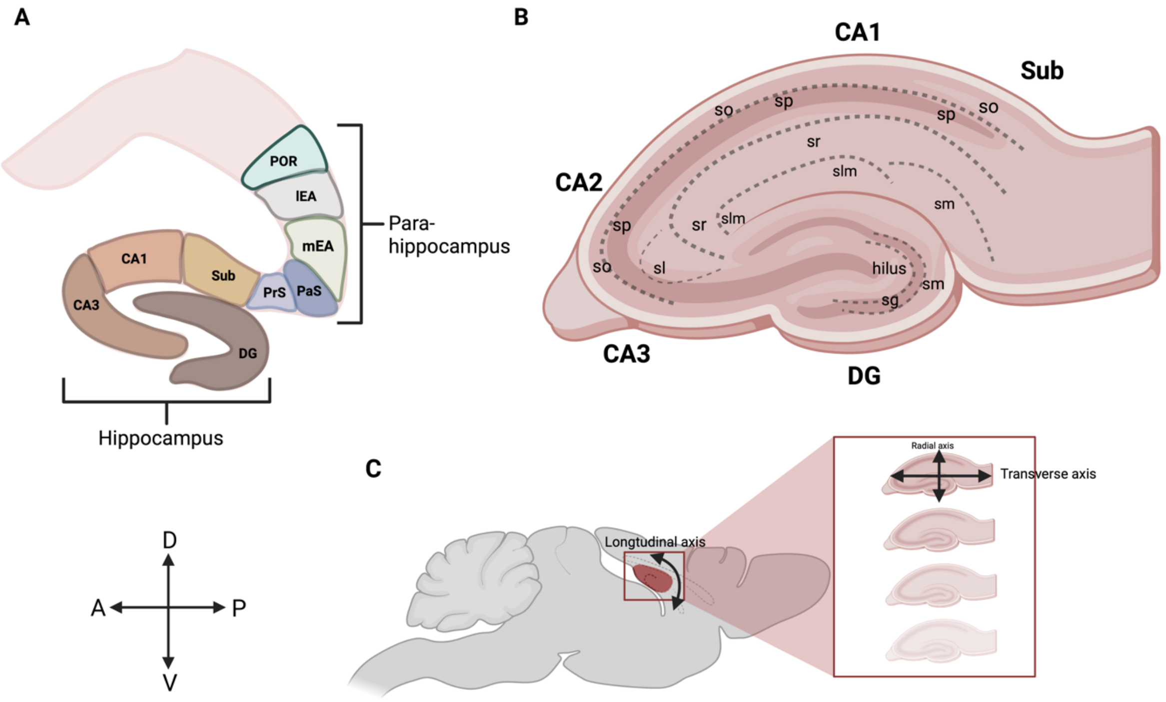

***Figure 1**. **The anatomy of the mouse parahippocampal-hippocampal formation.*** **A|** A horizontal cross-section view of the rodent hippocampal formation (consisting of the dentate gyrus (DG; dark brown), CA3 (medium brown), CA2 (not indicated), CA1 (orange), and the subiculum (Sub; yellow)) and the parahippocampal region (consisting of the presubiculum (PrS; medium blue) and parasubiculum (PaS; dark blue), the entorhinal cortex, which has a lateral medial (mEA; light green) and lateral (lEA; grey) aspect, and the postrhinal cortex (POR; dark green). **B|** A sagittal cross-section of the hippocampal formation, with subareas indicated (including CA2). Dotted lines indicate the distinctions of layered topography in the specific subregions (DG: sm, stratum moleculare; sg, stratum granulosum; hilus; CA3, CA2, CA1: so, stratum oriens; sp, stratum pyramidale; sl, stratum lucidum (exclusively in CA3); sr, stratum radiatum; slm, stratum lacunose-molecular; Sub: so; sp; sm). **C|** The red square indicates the position of the hippocampal formation in the mouse brain with three axes designated: the longitudinal axis, the transverse axis and the radial axis (superficial-to-deep/dorsal-to-ventral), perpendicular to the transverse axis. The lower left icon indicates the anatomical rotation of the sectional schemes (D-V; dorsal-ventral, A-P; anterior-posterior). The figure was made in BioRender.

### 1.1.3 Connectivity of the Parahippocampal-Hippocampal Region

The anatomical connectivity and intrinsic neural properties found in the parahippocampal-hippocampal system give rise to well-organized patterns of ensemble activity consisting of different parallel circuits. Based on the spatial distribution of sensory cortical inputs, it is hypothesized that these parallel circuits carry different types of information of importance in episodic memory (Witter et al., 2000). These distinct pathways terminate in different regions of the hippocampal formation, both along the longitudinal axis of all subfields and the transverse axis of CA1 and the subiculum (Witter et al., 2000). The anatomy of the parahippocampal-hippocampal network is specifically adapted to its critical role in memory consolidation and spatial navigation. Its complex structure represents a delicate balance of cells and connections necessary for these functions.

#### 1.1.3.1 The EC-Hippocampal Formation Circuitry

The EC is commonly assigned the main input and output structure of the hippocampal formation. The EC receives projections from numerous cortical structures, constituting a structure with eminent convergence of sensory input. The EC shares bidirectional connections with the CA1 of the HP and the subiculum and unidirectional projections innervating all other regions of the hippocampal formation (Figure 2; Witter et al., 2017). The collected EC-hippocampal circuitry is thought to act as an integrator of high-order multimodal signals (Li et al., 2020). The classical view of the information flow in this circuitry is referred to as the trisynaptic pathway. In this feedforward pathway neocortical information is converged in the EC before being transferred via the perforant path onto the DG. From there, DG neurons make connections with neurons in the CA3, followed by the CA1, and finally, the signal is conducted back to the EC via the subiculum (Witter, 2018; Chrobak et al., 2000).

The present view of the information flow in this circuitry supports a functional separation between the lateral EC (lEC) and the medial EC (mEC) (Figure 2). The mEC is thought to process spatial information (Hardcastle et al., 2017). Whereas the lEC operates on other types of information, such as time (Tsao et al., 2018; Montchal et al., 2019) and olfaction (Li et al., 2017; Xu & Wilson, 2012). Recent findings indicate recurrent interaction between the two information paths and suggest information integration between the two (Nilssen et al., 2019). Recent evidence supports the notion that CA1 pyramidal cells form two distinct sublayers along the radial axis (Mizuseki et al., 2011; Cembrowski et al., 2016; Valero et al., 2015). These cells also vary along the transverse axis with regard to the input received from the EC. mEC appears to provide spatial information to the pyramidal CA1 cells situated in the deep CA1, and the lEC transmitting non-spatial information to the more superficial CA1 pyramidal cells (Masurkar et al., 2017).

#### 1.1.3.2 CA1 input and output

The CA1 displays a more intricate input- and output architecture than previously suggested. Accumulating evidence supports bidirectional connectivity between the CA1 and the subiculum and EC (Figure 2; Nilssen et al., 2019; Naber et al., 2001). Furthermore, the subnetwork of the CA1 is considered the main output seat of the hippocampus and transmits information to the cortex as well as other non-cortical regions (Goode et al., 2020). The layers of the CA1 composes a range of different cell types with distinctive connections. The primary output of the CA1 within the hippocampus is directed toward the striatum. This projection exhibits topographical organization in its targets, forming a column in the transverse axis (Witter, 2012). The CA1 receives intrahippocampal input from both ipsilateral and contralateral CA3 regions, known as the Schaffer collaterals, as well as smaller input from the subiculum (Figure 2). In addition, various cortical and subcortical sources provide input to the CA1, mainly via the EC. The CA1 also receives input from regions such as the ventral tegmental area, locus coerulus, lateral supramamilary region, and the raphe complex. CA1 projections target several extrahippocampal regions, including the retrosplenial cortex, nucleus accumbens, ventral taenia, anterior olfactory nucleus, hypothalamus, and amygdaloid region (Witter, 2012). Although the hippocampus is connected to several other brain regions, the connections that originate within the hippocampus are the most predominant (Andersen et al., 2006).

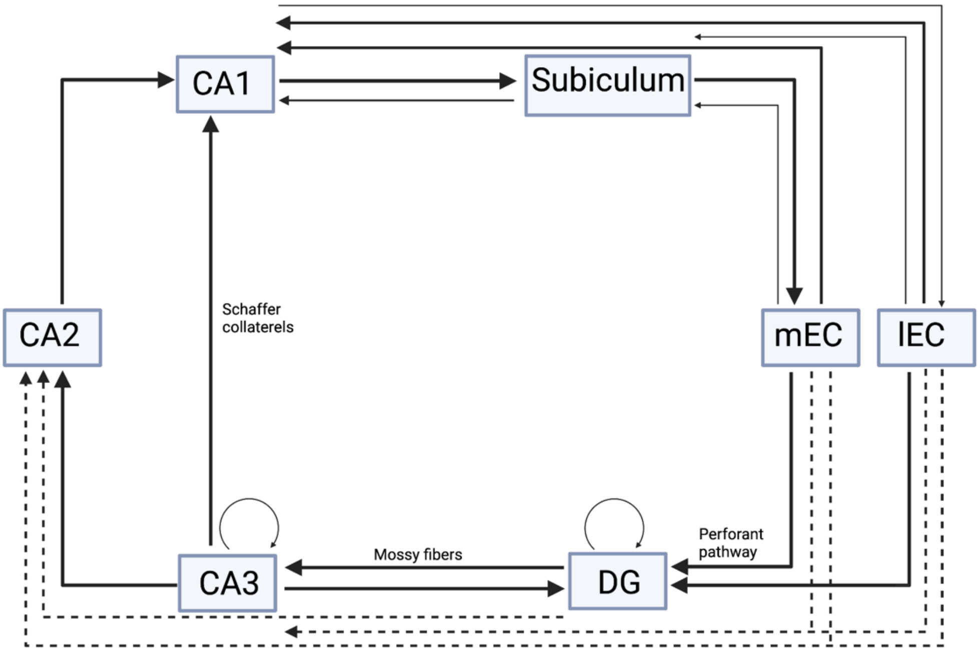

***Figure 2. Information flow in the EC-hippocampal network.*** Integrative scheme of the traditional trisynaptic (MEC/LEC →(Perforant path)→ DG →(Mossy fibers)→ CA3 → (Schaffer collaterals) CA1) and monosysnaptic (EC → CA1) pathways as well as the updated glutamatergic connections including the CA2, Subiculum, recurrent DG and CA3 connections and several revers' projections. The figure was made in BioRender.

### 1.1.4 Hippocampal Neuroanatomy

The internal hippocampal formation consists of a distinctive three-layered appearance (Mercer & Thomson, 2017). The organization of cell types in the hippocampal formation can be guided by the division of sublayers in the distinct regions (Figure 1B). The sublayers of the HP recognized by the anatomical organization of neural cells and the laminar organization are generally similar for all CA subfields (Witter et al., 2000). The pyramidal cell layer of the HP is called the stratum pyramidal, mostly composed of excitatory pyramidal neurons. The stratum oriens, located deep to the pyramidal layer, is a relatively cell-free layer, but one can locate a few inhibitory basket-cell interneurons and pyramidal axons, recurrent axon collaterals and commissural fibers. Located just above the pyramidal cell layer in the CA3 field, but not in CA2 or CA1, is a narrow noncellular zone, termed the stratum lucidum, containing the mossy fiber axons originating in the DG. At stratum lucidums distal end, the mossy fibers bend ventrally, indicating the CA3/CA2 border. Superficial to stratum lucidum in CA3, immediately above the pyramidal cell layer in CA2 and CA1, is stratum radiatum. This layer comprises apical pyramidal dendrites and some stellate cells, making up a big portion of the CA3-CA3 connections and the CA3-CA1 Schaffer collaterals. Finally, the stratum lacunosum-moleculare layer is composed of both pyramidal axons and interneurons. This is the most superficial layer and is where the perforant pathway fibers from the EC pass through and terminate (Figure 1B; Mercer & Thomson, 2017; Parmar et al., 2018; Mazher & Hassan, 2021).

The subicular structure holds the typical three-layered cytoarchitectonic features with other HP subfields (Figure 1B). The pyramidal cell layer of the subiculum displays a significantly thicker neural architecture than that of the HP. Finally, the DG is composed of three layers superficial to deep, the layers are: (I) the molecular layer, stratum moleculare, mainly containing neural bodies and granule dendrites; (II) the intermediate granular layer, stratum granulosum, is arranged by granule cells, considered the main cells of the DG; and (III) the polymorphic layer or the hilus, mainly comprising interneurons (Figure 1B).

#### 1.1.4.1 Cell Types in CA1

The CA1 region is mainly composed of pyramidal cells, which are smaller in size compared to those found in other sub-regions (Mizuseki et al., 2011). Typically, these cells have one basal dendritic tree extending into stratum oriens and one or two apical dendrites extending to the hippocampal fissure. Reports aiming to unveil gene expression patterns of pyramidal cells have revealed that the population in the CA1 is heterogeneous (Cembrowski et al., 2016). The most substantial heterogeneity is observed along the longitudinal axis. This heterogeneity is reflected in the differential projection originating from the EC. The lEC selectively targets cells in the distal CA1, while the mEC projects to the proximal CA1 (Mizuseki et al., 2011; Cembrowski et al., 2016; Valero et al., 2015;

Witter, 2018). Calcium imaging supports this observation, by implicating differences in firing properties along the radial axis of the CA1 (Danielson et al., 2016).

In addition to excitatory pyramidal cells, heterogeneous populations of gamma-amino-butyric acid (GABA) secreting interneurons can be found in all layers of the CA1. In mice, the number of these GABAergic neurons located in the CA1, increases substantially, aligning the radial axis (Jinno & Kosaka, 2006). Among these are a population of pyramidal basket cells with cell bodies located in the pyramidal cell layer (Jinno & Kosaka, 2006). These cells reside proximity to the pyramidal cells, and their axons extend transversely and innervate pyramidal cells (Meyer et al., 2002). Chandelier cells, another type of interneuron present in the CA1, does also innervate pyramidal cells via synapses that terminate on the initial pyramidal axon segment.

#### 1.1.4.2 Electrophysiological and Functional Properties of CA1 Pyramidal Cells

The electrophysiological properties of pyramidal cells in the CA1 are not consistent along the longitudinal hippocampal axis (Figure 1C). In one study, a ventrodorsally linear increase in input resistance and resting membrane potential was reported (Malik et al., 2016). Another study showed results indicating that pyramidal cells of the ventral CA1 were more excitable than those of the dorsal CA1 (Milior et al., 2016). The same study concluded that LTP, a form of synaptic plasticity elaborated in a later section, was the most pronounced in dorsal parts of the hippocampus. Taken together, these findings suggest that pyramidal neurons in the ventral aspects of the CA1 are extensively more likely to be active than their dorsal equivalents.

## 1.2 Spatial Selective Cells in the Hippocampal Formation

A number of excitatory cells in the hippocampal formation exhibit spatial selectivity, meaning that their activity pattern is tuned to specific features related to the subject’s location in the environment. These functional distinctive cell types contribute to the rodent's positional brain system (Kropff & Treves, 2008; Sargolini et al., 2006; Solstad et al., 2008) and related patterns of activity in other species, such as humans (Doeller et al., 2010; Jacobs et al., 2010; Reagh & Yassa, 2014). The first spatial tuned cells to be discovered was the place cell, located in the hippocampus. Typically, these cells display periodical activity in a single or a few areas within a given environment, referred to as the corresponding ‘place field’, and are hypothesized to support formation of a cognitive map of immediate space (O’Keefe & Nadel, 1978). The theory of cognitive maps suggests the presence of a complex internalized model of space enabling encoding, storage, and decoding of information related to the relative locations and other central qualities associated with a given spatial environment (Tolman, 1948). Place cells operate in conjunction with other types of spatial selective cells and non-spatial selective cells found in the hippocampal and parahippocampal formation to provide a complete picture of the organism's location and orientation in space (Stefanini et al., 2020). These include grid cells, head direction (HD) cells, boundary cells, object-vector cells, and speed cells. Grid cells are commonly found in the EC and exhibit a distinctive firing pattern, creating a hexagonal grid-like pattern in response to the position of an animal within an environment, providing the subject with navigation opportunities and metrics of the space (Hafting et al., 2005). The specific grid pattern of each cell remains consistent as the animal moves across various environments.

Common observations in these cells’ spatial dimensions reveal features such as pinpointed, bell-shaped tuning curves (O'Keefe, 1976), invariances (Muller et al., 1994), and recurringly repeating activity (Fyhn et al., 2004; Hafting et al., 2005). Combinations of these features along different spatial dimensions are also commonly observed (Sargolini et al., 2006; Krupic et al., 2012). As for example, speed cells are commonly invariant to location (Burgess et al., 2005), and place cells are often invariant to the movement speed of the subject (Muller et al., 1994).

Overall, the activity of distinct spatial selective cells is important for the ability to perceive and navigate in space, and compose a central part of the brain's spatial representation system.

### 1.2.1 Place Cells

Place cells display characteristic functional properties in response to locomotory input, including stability, specificity, and remapping of place fields. Spatial specificity indicates the place fields' focality and multiplicity, and frequency of fields in a constant environment. Remapping occurs when an animal moves to a novel environment, and the configuration of place fields is rearranged accordingly. Stability pertains to the temporal consistency of the place fields when the animal returns to a familiar environment. Place cell functionality is reported to vary along the hippocampal axis. Along the radial axis of the hippocampus, it appears that deeper neurons have a higher probability of having place cell characteristics than neurons found more superficial (Mizuseki et al., 2011).

#### 1.2.1.1 Specificity

The firing patterns of place cells are highly environmentally specific. Generally, these cells display a single place field each, but CA1, CA3, and DG place cells can exhibit multiple irregularly spaced fields (Park et al., 2011). The probability of multiple fields per cell increases in notion with the expansion of the recording enclosure (Park et al., 2011). It has been proposed that the specificity of the place field might relate to the developmental level of the neuron itself, with increased specificity in later developmental stages (Neunuebel & Knierim, 2012).

In 2014, Alme et al. recorded CA3 place cells in rats in 11 different recording boxes with a total of 55 comparisons of place maps in each subject. The representations showed a high correlation in repeated tests within the same room, but they remained orthogonally related across all different room combinations with minimal overlap in active cell samples across environments. While a small proportion of cells were active in multiple rooms, the firing locations of these cells were completely uncorrelated (Alme et al., 2014). This demonstrates high independent specificity of place cells in this hippocampal region, thus facilitating for high storage capacity.

The size of the place field is variable between the place cells but stable in an unchanged environment. Generally, the size of the field is larger at the ventral hippocampal pole compared to the ones at the dorsal pole. This ventral-dorsal increasement is close to linear (Kjelstrup et al., 2008). Place field size has been investigated using a cation channel knockout mouse model, as this specific hyperpolarization-activated cyclic nucleotide-gated channel 1 (HCN1) is highly expressed in grid cells and CA1 place cells. The results indicated that the knockout mice displayed a substantial increase in field size in the CA1, whereas CA3 was only moderately affected (Hussaini et al., 2011). The pronounced size variability might suggest that CA1 place cells are more reliant on local circuitry than information transfer from EC grid (Hussaini et al., 2011). Davoudi and Foster (2019) utilized a genetic approach to inhibit the release of vesicles from CA3 terminals, which correlated to an increase in place field size in the CA1. Optic flow, related to path integration, also affects place field size. Lu and Bilkey (2010) observed a decrease in place field size, when experimentally increasing the optic flow information perceived by the rat. Additionally, the number and quality of local cues available may impact place field size, considering the observation of negative correlation between the number of cues presented to the animal and related place field size (Sharif et al., 2021).

Although the peak firing rate within place fields is typically stable in invariant environments, experimental manipulations of place field size seem not to affect peak firing rate (Hussaini et al., 2011). Supporting this, when Lu and Bilkey (2010) introduced increased optic flow information, the decrease in place field size did not correlate with changes in firing rate. Thus, the peak firing rate remains independent of place field size. Furthermore, Davoudi and Foster (2019) discovered that when disrupting signals from CA3 place cells, the place field peak firing rate of CA1 place cells was not affected.

#### 1.2.1.2 Remapping

Although place cell activity remains stable in familiar surroundings, it is not rigid. The activity can change in response to alterations in environmental cues, defined by shifts in the cells' preferred firing location, this phenomenon is known as remapping (Muller and Kubie, 1987). Remapping of place fields happens both on a local and a global scale (Muller and Kubie, 1987; Latuske et al., 2018). Local scale, or partial, remapping refers to the remapping of a subset of place cells. Global remapping denotes a total remapping of the whole place cell population. Rate remapping, on the other hand, is modulation of firing rate of the place cells in response to sensory input via the EC (Rennó-Costa et al., 2010).

The role of the mEC in remapping of place fields has been thoroughly studied. A recent lesion study showed that place cells retained the ability to remap across changing environments, despite experimental impairment of the mEC (Schlesiger et al., 2018). Another recent study using an Alzheimer-prone mouse model, in which mEC cells deteriorate at a higher rate than place cells, reported that the remapping ability of the place cells was preserved in the absents of mEC input (Jun et al., 2020). On the other hand, it has been observed that global remapping in hippocampal place cells correlates with grid field reorientation in the mEC, indicating that place cell input originating from mEC grid cells, which might have a role in modulating remapping (Fyhn et al., 2007). Furthermore, when isolating the effects on CA1 place cells, Rueckemann et al. (2016) discovered that ontogenical inactivation of the mEC initiated partial remapping in CA1 cells. Adding to that, Kanter et al. (2017) reported correlation between activation of mEC neurons and remapping in CA1.

As both activation and inactivation of mEC neurons resulted in remapping, but disruption of the mEC-CA1 input pathway did not affect remapping, this might illustrate that mEC signaling assists in place cell stabilizing. The mEC-CA1 interaction might act as a synchronizer of the mEC input to the hippocampal place cells. This enables remapping of place cells in response to large changes in neural activity patterns of the mEC. A modeling study performed by Rennó-Costa and Tort (2017) supports this by demonstrating that mEC activity enhanced the place cell’s ability to retain stability in activity patterns when encountering unstable sensory input and filter out potentially inferring noise. The model supports place cell remapping as a foundation for grid realignment, consistent with Fyhn et al.'s (2007) observations. Additionally, the researchers predict the involvement of the mEC-hippocampus circuit in the creation of cognitive maps.

#### 1.2.1.3 Stability

Specific place cell tuning has been observed to remain stable over long periods of time. A recent study performed by Kinsky et al. (2018) demonstrated that when animals navigate in familiar contexts, the hippocampal spatial map display coherent rotations persistent over time. Place fields have been reported to persist stably for up to 153 days (Thompson & Best, 1990), thus supporting the idea of long-term stability in these cells.

Differentially located place cells in the hippocampal subregions display varying long-term stability. The nature of emergence of place field specificity, when introduced to a new environment, appear to be region-specific. Dong et al. (2021) carried out 2-photon calcium imaging in mice while moving in novel virtual environments. The trial-to-trial dynamics of CA1 and CA3 place cells in long-term stability paradigm were compared. Place cells in CA1 emerged more rapidly but tended to shift more backward, as well as displaying more remapping between environments, compared to CA3 place cells, which emerged more gradually but showed more stable long-term dynamics. Suggesting that the emergence of place representation in CA1 is not merely a result of direct information transfer from CA3.

In the CA1, place field stability seems to exhibit sublayer specificity. In a study by Danielson et al. (2016), it was demonstrated that the stability of spatial representations varied significantly across the radial axis of the CA1. Deeper situated place cells exhibited higher stability during a goal-oriented exploration task than during regular exploration, compared to more superficial cells. Thus, suggesting that deeper situated CA1 place cells encode the salient features of a specific environment, whereas the more superficial cells encode a more stable spatial representation.

Recent studies have produced results demonstrating that perturbation of input regions to the CA1 disrupts typical place cell stability. Lesions to the mEC in rats, along with deprivation of available sensory stimuli, obliging the rats to rely on self-motion cues, showed a reduction in place cell stability (Jacob et al., 2020). Furthermore, blocking the mEC HCN1 channels, a channel associated with the regulation of synaptic integration and the generation of grid cell firing patterns, caused an increase in grid scale but spared the ability to convey spatial signals. These observations were correlated with a disruption in long-term stability of place fields. Furthermore, the reunions and rhomboid nuclei of the ventral thalamus midline have been indicated to correlate to place cell stability (Cholvin et al., 2018). Lesions to this area triggered extensive and long-lasting disruption of CA1 field stability.

### 1.2.2 Head Direction, Speed, Boundary, and Conjunctive Cells

Cells respondent to sensorimotor information related to the animal’s path is found in all parts of the hippocampus. The hippocampal spatial cells are tuned to multiple different features relevant to the location of the animal in the environment. The succeeding section will elaborate on the following cells: head direction (HD), speed, boundary, and conjunctive cells.

HD cells respond to the animal's perceived directional heading with respect to its environment (Taube et al., 1990). These neurons fire at a stable rate above baseline when the animal's head is oriented toward the cell's preferred firing direction. HD cells are usually found outside of the hippocampus, but the information transmission from the mEC carries parts of the HD information (Winter & Taube, 2014). A limited number of robust HD cells have also been observed in the internal hippocampus (Lautgeb et al., 2000).

Cells tuned to speed measures, known as speed cells, are correlated with the pace of the animal. These cells display higher firing frequencies when the animal moves at a higher rate. They are present in both the mEC and the hippocampus (Ye et al., 2018).

Boundary cells (also known as border cells or boundary vector cells) respond to environmental boundaries at specific distances and directions from the animal. Computational models of hippocampal place cell firing patterns predicted the existence of "boundary vector cells" (O'Keefe and Burgess, 1996; Burgess et al., 2000; Hartley et al., 2000). Cells fulfilling this description have later been observed in the hippocampus (Lever et al., 2009).

A portion of spatial selective cells also shows conjunctive spatial correlates. For example, many HD cells also respond specifically to the location of the animal. This is also seen in other cells, such as speed cells and boundary cells. Conjunctive cells potentially play an integrative role in the hippocampal network, where spatial representations are refreshed by path integration signals (Moser et al., 2017).

## 1.3 Spatial Memory and Synaptic Plasticity

A striking feature of synapses in the central nervous system, particularly those in the hippocampal circuit, is the phenomenon of activity-dependent synaptic plasticity. The process allows the strength of synapses to be regulated for prolonged periods of time through various patterns of synaptic activity (Basu & Siegelbaum, 2015). This process can be either homosynaptic, meaning that the strength of synaptic communication at the same synapses that were activated is altered, or heterosynaptic, in which activity in one synaptic pathway affects the function of another pathway. Although substantial correlative evidence linking plasticity to hippocampal-dependent memory formation has been collected, the precise role of plasticity mechanisms in learning and memory formation remains indefinable (Kolb & Gibb, 2014; Abraham et al., 2019). The complexity likely emanates from the existence of a multitude of different forms of plasticity, differing in their induction activity pattern, molecular mechanisms for induction and expression, and the duration of the plastic alternation. Some of the eminent types of microscale plasticity reported from this region include LTP (Whitlock et al. 2006), long-term depression (LTD; Di Prisco et al. 2014), spike-timing-dependent plasticity (STDP; Nishiyama et al., 2000), homeostatic plasticity (Kim & Tsien, 2008) and meta-plasticity (Crestani et al., 2019). The following section will assess homosynaptic LTP.

### 1.3.1 Homosynaptic Long-Term Potentiation and the Microscale Physiology of Associative Memory

Spatial cells depend upon synaptic alternations to form short- and long-term spatial representations. Donald Hebb (1949) formulated the initial theoretical proposal addressing the importance of homosynaptic activity-dependent plasticity as a mechanism for developing neural assemblies.

> “When an axon of cell A is near enough to excite a cell B and repeatedly or persistently takes part in firing it, some growth process or metabolic change takes place in one or both cells such that A’s efficiency, as one of the cells firing B, is increased.” (Hebb, 1949).

This synaptic learning rule is thought to account for the wiring of neuronal assemblies with shared tuning properties. Additionally, Hebbian plasticity is well suited for the formation of neural ensembles encoding a given memory, such as representations of space. LTP is the most classical example of a Hebbian synaptic learning rule. Bliss and Lomo (1973) were the first to induce artificial LTP in the perforant path inputs to the DG of the rabbit. They observed that a brief and intense tetanic stimulation generated a durable increase in the potency of excitatory synaptic transmission from the perforant path to DG, persisting for hours to days. Since then, LTP has been demonstrated at nearly all hippocampal synaptic transmission sites.

LTP, in accordance with Hebb’s rules, appears at most synapses in the hippocampus. The process requires strong synaptic activity, adequate to drive postsynaptic spike firing (Figure 3; Bliss et al. 2014). Several properties of LTP make it a suitable mechanism for learning and memory formation. LTP induction is rapid and can be long-lasting. Also, it is very specific in which synapses get strengthened (Figure 3). There is also a prominent difference in the time frame and length of synaptic efficacy changes across various forms of synaptic plasticity. LTP can account for both short and long timeframes of synaptic alternations, with distinct molecular mechanisms regulating them (Pastalkova et al., 2006). Short-LTP, accounting for the temporal synaptic alternations taking place within the first two hours after synaptic activity, relies on the insertion of new receptors in already existing synapses. Long-LTP relies on the synthesis of new synapses between the pre- and post-synaptic neuron after adequate synaptic activity and can last for years, accounting for long-term memory formation (Baltaci et al., 2019). Theoretical studies support the idea that expression of different temporal phases of LTP aid to maintain stable long-term memory traces while new memories are being formed through changes in synaptic function (Fusi et al. 2005).

The induction of LTP depends on the glutamatergic receptors N-metyl-D-aspartat (NMDA), ɑ-amino-3-hydroxy-5-methyl-4-isoxazolepropionic (AMPA), and metabotropic glutamate receptor 5 (mGluR5). Activity-dependent Hebbian LTP is characterized by features determined by the properties of NMDARs. The activity of these receptors is essential for inducing LTP at several synapses, including the Schaffer collateral-CA1 synapses (Collingridge et al. 1983). NMDA is selectively permeable to $Ca2^{+}$, which initiates an intracellular signaling cascade when entering the cell. The cascade leads to the insertion of additional AMPA receptors into the synapse, in the early phase of LTP, or activation of transcription factors and associated protein synthesis to create additional synapses, in the late phase of LTP (Baltaci et al., 2019). The insertion of AMPA receptors and additional synapses strengthens the connection between the cells. mGluR5 regulates the intracellular $Ca2^+$ levels, thus having a mediating role in LTP induction (Bikbaev et al., 2008).

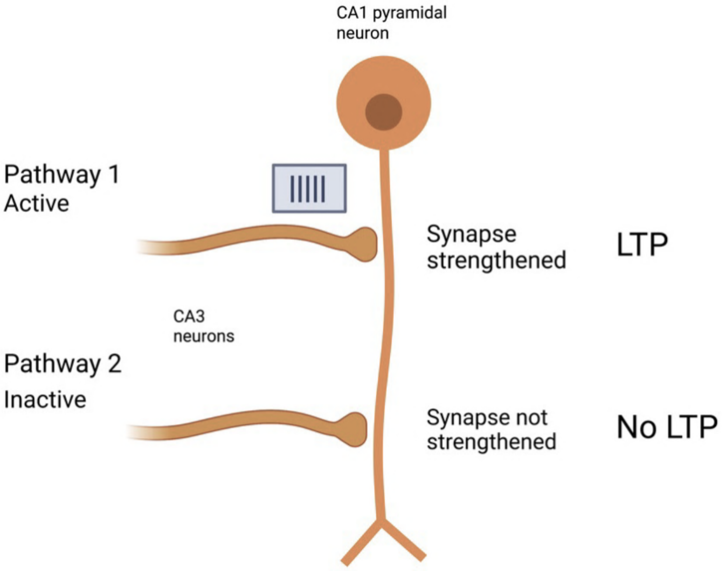

***Figure 3. Specificity of homosynaptic LTP in the schaffer collateral pathway.*** Scheme showing the Hebbian synaptic learning rule of homosynaptic specificity emerges in the CA1 microcircuit from temporally patterned activity of synaptic inputs (CA3-CA1 Schaffer collateral inputs) and the postsynaptic CA1 pyramidal neuron. The active pathway 1 is strengthened, whereas the inactive pathway 2 is not strengthened through LTP. The figure was made in BioRender.

### 1.3.2 Synaptic Plasticity in CA1 Spatial Cells

Place cells and other spatial cells are reliant on activity-dependent synaptic plasticity to rapidly encode, update, and retrieve patterns of population activity representing specific spatial information (Figure 3). Morris et al. (1986) provided the first evidential link between LTP and spatial memory by pharmacologically blocking NMDARs and demonstrating that this inhibits formation of spatial reference memory, assessed by the Morris Water Maze (MWM). The NMDAR blockade did not prevent the animal from finding a way out of the water when the platform was visible, reflecting behavior independent of the hippocampus. Thus, limiting the effects of the blockade to spatial memory. Furthermore, place field stability across two recording sessions separated by 24 h was reduced after pharmacological blockade of NMDARs (Kentros et al., 1998).

Genetic evidence correlating LTP in the CA1 region with spatial learning has been provided by studies also utilizing manipulation of NMDAR function. Mice with an NMDAR subunit (NR1) depletion in the CA1 express loss of tetanus-induced LTP at the Schaffer collateral-CA1 pathway, as well as profound deficits in the MWM task (Tsien et al. 1996). However, deletion of NR1 restricted to CA1 and DG showed no effects on spatial reference memory behavior of mice, whereas performance in spatial working memory tasks was significantly impaired (Bannerman et al. 2012). These mice did indeed display difficulties in relearning a new location of the platform in the MWM after initial training. These results suggest that NMDAR-dependent LTP in the hippocampus is critical for resolving divergence between stored information and the current sensory context, instead of encoding of paired associative memories (Bannerman et al. 2014).

*In vivo* extracellular recording experiments in rodents during learning behaviors have presented important evidence in linking hippocampal microscale plasticity to learning. In a study conducted by Whitlock et al. (2006), it was discovered that a single instance of inhibitory avoidance learning resulted in an amplification of synaptic responses when electrically stimulating the Schaffer collateral-CA1 pyramidal neuron inputs. Additionally, the behavioral changes brought about by the learning process exhibited similar alterations in AMPA receptor phosphorylation and membrane trafficking as those induced by tetanic stimulation that leads to LTP. Place cells rely on synaptic protein synthesis, much like LTP, in place field formation and long-term place field stability. Formation of new CA1 place fields can occur rapidly in an environment through LTP, in which initiation of spiking by dendritic $Ca2^+$ plateau potentials triggers an increase in weights of excitatory synaptic inputs (Bittner et al., 2015; Grienberger et al., 2017). In 2004, Agnihotri et al. conducted a study in which they administered protein synthesis inhibitors via injection into the CA1 region while simultaneously recording the activity of place cells in that area. The results showed that the intervention did not have an impact on the short-term stability of place fields, but their long-term stability was significantly disrupted. Notably, the intervention showed no effects in the retrieval of pre-existing spatial representations, indicating that protein synthesis is crucial in spatial memory encoding, but not in retrieval.

Non-Hebbian plasticity as an underlying mechanism for place field formations in the CA1 is supported by the conductance of *in vitro*, *in vivo*, and supplementary modeling data. Bittner et al. (2017) performed intracellular recordings in CA1 pyramidal cells and discovered that induction of single strong $Ca2^+$ plateau potential in the neuronal dendrites paired with spatial stimuli was adequate to generate place cells. This observation suggests that alternations in synapse strength might be critical in the formation of place fields. In addition to plastic changes at the excitatory synapses onto CA1 pyramidal neurons, several studies have documented that synapses between pyramidal cells and inhibitory interneurons also undergo activity-dependent plastic changes. One of the most significant forms of activity-dependent plasticity at inhibitory synaptic transmission is mediated by the endocannabinoid-signaling pathway (Castillo et al. 2012; Younts and Castillo 2014).

While some experimental paradigms suggest that endocannabinoids also contribute to LTD and LTP at excitatory Schaffer collateral synapses (Ohno-Shosaku et al. 2002; Peterfi et al. 2012), their primary effect is to suppress inhibition onto pyramidal cells. these observations indicate that formation of place cell spatial functionality depends upon the signaling in the local circuitry.

Given the number of input connections the CA1 receives from other subregions of the hippocampal formation, spatial representations in the CA1 could simply be obtained from upstream input (Solstad et al., 2006; Neher et al., 2017; Mankin et al., 2015). However, given the diverse forms of synaptic plasticity that have been observed at the CA1 synapses (Magee & Grienberger, 2020; Buchanan & Mellor, 2010), the complexity of CA1 dendritic computations (Sheffield & Dombeck, 2019; Sheffield et al., 2017), and the variability in CA1 interneurons (Pedrosa & Clopath, 2020), it is unlikely that CA1 activity dynamics are purely inherited. The findings of Dong et al. (2021) support this by illustrating that place fields of CA1 emerge more rapidly than the ones in CA3 and show less stable dynamics. Thus, supporting those alternations in synaptic weight in the local CA1 circuitry is of importance for the formation of spatial cell functionality.

### 1.4 Epigenetic Gene Regulation

Traditional neuroscience has largely been focused on understanding how learning and memory manifest at a cellular and molecular level. In the last decade, there has been a shift towards exploring the epigenetic mechanisms that underlie the changes in gene activity responsible for memory formation and maintenance. Epigenetic gene regulation involves physical marking of DNA or associated proteins to induce enduring modifications in gene activity (Yu et al., 2011). Although all cells in an organism fundamentally share the same genetic information, cell type, and function differ greatly due to quantitative and qualitative differences in gene expression (Chi & Bernstein, 2009; Kaminsky et al., 2009). Epigenetics refers to processes that can cause stable changes in cell function and specificity through regulating gene expression, without causing changes to the DNA sequence itself. Epigenetic mechanisms, such as DNA methylation, have been shown to play an important role in learning and memory (Rumbaugh & Miller, 2011; Poon et al., 2020).

#### 1.4.1 DNA Methylation

DNA methylation refers to the process of adding a methyl group from the cofactor S-adenosyl-methionine (SAM) to the 5th carbon of the cytosine (C) residue to form 5mC (Figure 4) (Duan and Lu, 2020; Lubin, 2011). Primary, this takes place on a C positioned preceding guanine (G), forming CpG dinucleotides. Areas rich in CpG nucleotides are referred to as CpG islands and are characteristically hypomethylated (Qazi et al., 2018;

Zusso et al., 2018). Both the initial catalysis and the maintenance of C methylation depend on DNA methyltransferases (DNMTs) (Duan and Lu, 2020). DNMT3A and DNMT3B regulate the *de novo* methylation of CpG sites. DNMT1 is involved in maintenance of previously established methylation patterns (Figure 4) (Bali, Im, & Kenny, 2011). The addition of an outward projecting methyl group acts as a steric interference, preventing the binding of RNA polymerase (Landgrave-Gomez et al., 2015). The hypermethylation of a promoter region is often associated with the suppression of gene expression and more indirectly an increase in heterochromatin formation. Expression of downstream proteins associated with the specific gene is thereby repressed (Landgrave-Gomez, Mercado-Gomez, Guevara-Guzman, 2015).

### 1.4.2 DNA Demethylation

Despite DNA methylation’s role in long-term gene silencing, studies over the last decades have revealed that this epigenetic mark is not as stable as previously assumed (Bochtler et al., 2017). Regardless of chemical and genetic stability, 5mC can be converted back to an unmodified state, a process called DNA demethylation (Bochtler et al., 2016). This process can happen both passively and actively. Passive DNA demethylation refers to replication-dependent dilution of 5mC resulting from the absence of functional DNA methylation maintenance machinery, for example, DNMT1 (Figure 4; He et al., 2017; Inoue & Zhang 2011). Active DNA demethylation involves the enzymatic removal of methyl groups (Figure 4). Among the proposed mechanisms for active demethylation, the hypothesizes suggesting the base excision repair (BER) pathway appears to be the most evident (Xue et al., 2022.; Müller et al., 2014.; Cortellino et al., 2011). These include the following pathways: (I) the spontaneous deamination demethylation pathway, and (II) the oxidation-mediated demethylation pathway (Moore, Le & Fan, 2013).

*(I) The Deamination-Based Demethylation Pathway.* Activation-induced deaminase (AID) spontaneously deaminates 5mC to thymine (T) by simple hydrolysis, resulting in the mispairing of T and G (Bochtler et al., 2017). The process of recognizing and removing mispairing is carried out by TDG, which specifically targets mismatches and creates an abasic site. This site is then repaired by downstream factors involved in the BER pathway (Schuermann et al., 2016). BER is the primary mechanism for correcting small base lesions resulting from processes such as oxidation, deamination, or alkylation (Krokan & Bjørås, 2013). Marking the initial stage of BER, a DNA glycosylase enzyme recognizes and removes damaged or mismatched nucleotide bases, forming an abasic site. This site is then repaired by apurinic/apyrimidinic endonuclease I (APE I), generating a 3'OH group at the damage site. Subsequently, DNA polymerase account for repair synthesis and nick sealing completed by a DNA ligase (Krokan & Bjørås, 2013; Schuermann et al., 2016. The process

of BER ensures the accurate substitution of the missing nucleotide and replaces the initial 5mC with a non-modified C.

*(II) The Oxidation-Mediated Demethylation Pathway.* Biochemical and genetic studies suggest a central role of TET in DNA oxidative demethylation (Tahiliani et al., 2009; Dawlaty et al., 2014). TETs oxidize methyl groups and act on modified C. 5mC is converted into 5-hydroxymethylcytosine (5hmC), 5hmC to 5-formylcytosine (5fC), and 5fC to 5-carboxylcytosine (5caC) (Tahiliani et al., 2009; Kriaucionis & Heintz 2009; Ito et al., 2011). 5hmC can be depleted passively through DNA replication or actively transformed into C by undergoing successive oxidation by TET and TDG-initiated BER. TDG-initiated BER can effectively recognize and eliminate both the oxidized substrates, 5fC and 5caC (Maiti & Drohat, 2011). Previous studies have demonstrated that TDG depletion in embryonic stem T-cells and cells correlates with the accumulation of TDG-recognized substrata 5caC and 5fC (Schwarz et al., 2020; Onodera et al., 2021). Altogether, TDG's role in the deamination-based and oxidative DNA demethylation pathways, suggests an important role of TDG in the dynamic regulation of methylation patterns, and thus transcriptional regulation, through its function in demethylation.

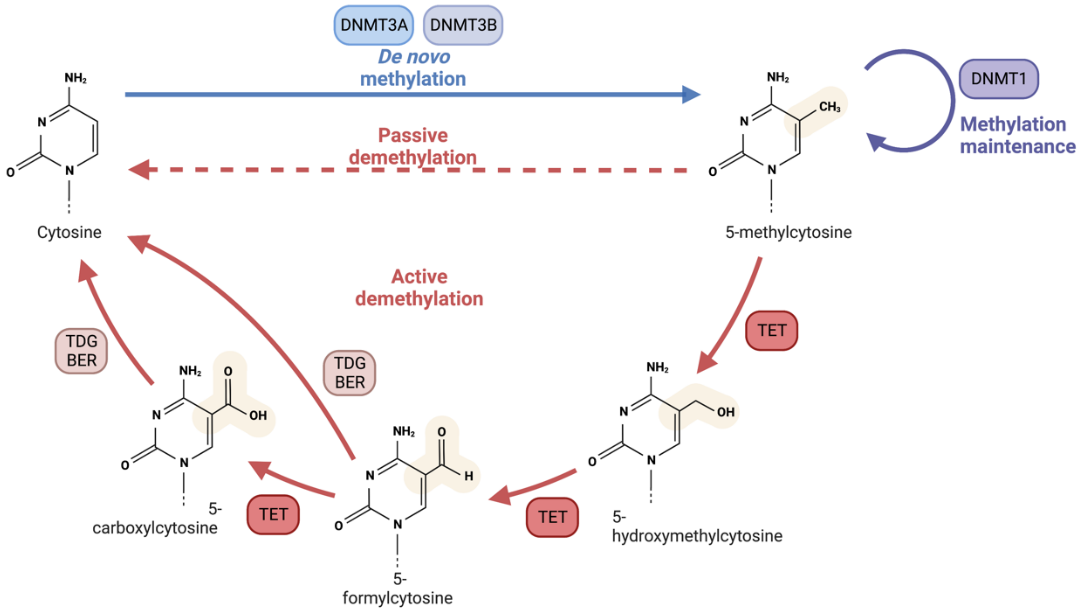

***Figure 4. The cycle of DNA methylation and demethylation****. De novo* methylation (blue) by DNMT3A and DNMT3B converting Cytosine (C) to 5-methylcytosine (5mC). Methylation maintenance (purple) of 5mC requires DNMT1. Demethylation (red) of 5mC occurs either by passive mechanisms (red dotted lines) or by actively (red solid lines) by TET-facilitated conversion of 5mC into 5-hydroxymethylcytosine (5hmC), from 5hmC to 5-formylcytosine (5fC), and from 5fC to 5-carboxylcytosine (5caC), followed by TDG-BER coupled conversion of 5caC to C or by replication-dependent TDG and BER processes converting 5fC to C. The figure was made in BioRender, by modifying an existing template.

### 1.4.3 Thymine DNA Glycosylase – Gene and Function

The human *TDG* gene is situated on chromosome 12q23.3, comprising a coding sequence of 3,551 bp, consisting of 10 exons, encoding a full-length protein (NCBI Gene ID: 6996). The mouse counterpart of this gene, *Tdg*, which is orthologous to the human *TDG*, is located at 10 C1; 10 39.72 cM (NCBI gene ID: 21665). *TDG* shows general nuclear expression in humans, but its expression patterns in the brain are not reported. However, The Human Protein Atlas reports *TDG* to display low regional expression specificity, with predominantly robust expression in neurons (Uhlén et al., 2015).

TDG was originally discovered for its function in repair of TxG mismatches. The coded protein belongs to the uracil DNA glycosylase (UDG) superfamily of DNA repair enzymes (Cortázar et al., 2007). TDG plays a crucial role in initiating the BER pathway by recognizing and removing erroneous T×G and U×G mispairs, arising due to spontaneous C and 5mC deamination (Smet-Nocca et al., 2008). Specifically, TDG hydrolyzes the N-glycosidic bond of T and U when mispaired with G, excising the mispaired base and creating a non-destructive DNA lesion (abasic site), which inhibits further DNA polymerase activity and potentially error-prone synthesis (Steinacher & Schär, 2005). In addition, TDG was the first enzyme found to be capable of excising 5fC and 5caC, implying its prominent function in DNA demethylation (Maiti & Drohat, 2011; He et al., 2011; Bochtler et al., 2016). Moreover, TDG interacts directly with transcription factors. Studies have shown that TDG interacts with the CREB binding protein, a coactivator responsible for triggering transcription activation by chromatin remodeling (Malfatti et al., 2021). In this way, the enzyme regulates gene expression not only indirectly through regulating the methylation patterns and chromatin remodeling factors but also directly through the interaction with transcription factors.

Compared to other DNA glycosylases, TDG appears to have a unique function in embryonic development, playing a crucial role in the regulation of developmental genes (Cortázar et al., 2011). Studies have demonstrated that mouse embryos lacking TDG do not survive past E11.5. Furthermore, mouse embryonic fibroblasts derived from TDG-deficient embryos exhibit histone modification imbalance, abnormal CpG methylation, and impaired gene regulation in the affected gene promoters (Cortázar et al., 2011). The collective body of evidence supporting the involvement of TDG in active DNA demethylation underscores the functional role of TDG in connecting DNA repair, epigenetic DNA modifications, and gene expression regulation.

### 1.4.4 DNA Methylation and Demethylation in Learning and Memory

One might ask how DNA modification in the nucleus, which has a cell-wide impact, could be involved in forming and maintaining a very specific spatial memory. A single neuron shares thousands of synapses with numerous other neurons, thus, it is reasonable to assume that one neuron contributes to multiple different memory formations through diverse synapses. If so, unaided genetic CpG methylation cannot differentially influence every respective synapse of a neuron without synapse-specific changes. A possible mechanism for storing multiple memories in a single neural population is a balance between methylation and demethylation activity (Miller et al., 2010). Following a learning experience, the profile of synaptic weights or intrinsic properties of the participating neurons would undergo adjustments (Figure 5). In order to preserve this modified network of connections, neurons must hold certain levels of their gene products. The gene products can be systematically balanced at the transcriptional level by specific DNA methylation patterns at the respective regulatory genetic element.

The interplay between upregulation and downregulation of genes by active DNA methylation and demethylation pathways in memory formation and maintenance has been identified in multiple brain circuits (Miller and Sweatt 2007; Feng et al. 2010; Miller et al. 2010; Day et al. 2013; Kaas et al. 2013; Rudenko et al. 2013). Thereby, suggesting a conserved functional role of balanced regulation gene expression in neuronal information storage across a variety of neural classes (Figure 5).

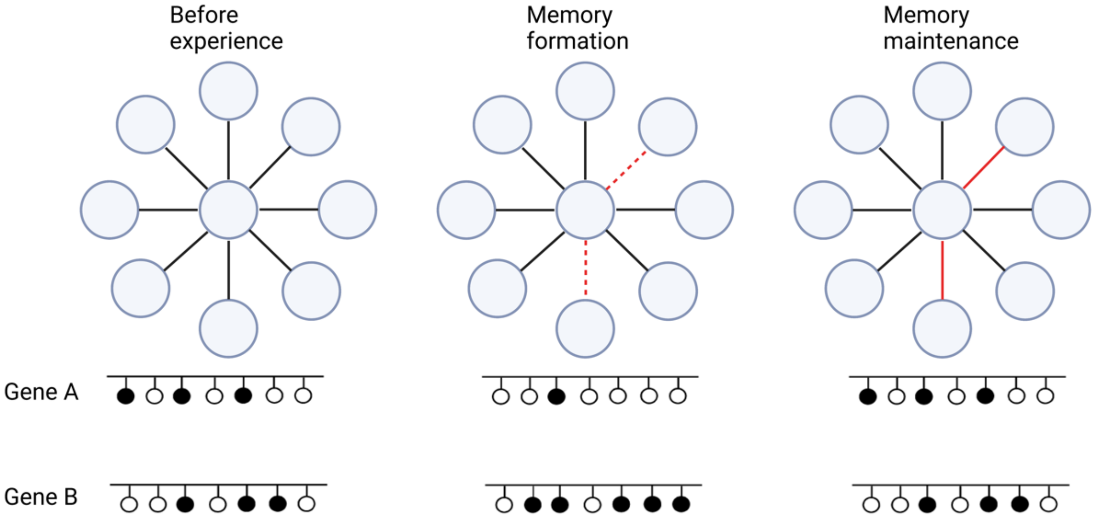

***Figure 5. DNA methylation in learning and memory.*** Upper: a neuron (central blue circle) shares connections with other neurons (peripheral blue circles). Lower: Every circle represents a CpG site in a regulatory element of the gene sequence. Methylated CpGs are indicated by filled black circles and unmethylated CpGs by white circles. When an animal experiences something unfamiliar ("Memory formation" state), some of the present connections are activated (red dashed lines). Memory formation requires a temporary series of gene upregulation or downregulation, which may be facilitated by DNA methylation and demethylation modifications over time. The transcription of memory suppressor genes (Gene B) is downregulated by DNA methylation, while genes inducing plasticity (Gene A) are upregulated by demethylation. After memory consolidation, the gene's methylation states are restored to baseline. In the "Memory maintenance" state the neurons exhibit altered connection strengths, compared to the connection profile in the "Before learning" state (upper panel). The gene expression profile in the neurons are different after learning, in order to maintain the modified connection strength combinations. The figure is adapted, including some modifications done in BioRender, from Yu et al. (2011).

### 1.4.4.1 DNA Methylation and Memory

In 2020, Poon et al. provided a detailed account of the functions performed by major enzymes (MeCP2, DNMT3a, and DNA demethylases) central in carrying out the DNA methylations or demethylations recognized as the basis of memory formation. To my knowledge, the distinct role of TDG in memory has not yet been assessed, but in the following some of the current data connecting DNA methylation and demethylation to hippocampal-dependent learning and memory will pe presented.

Fear conditioning, an associative memory task where a context is paired with aversive stimuli, has long been utilized to investigate the relationship amongst DNA methylation and memory. Early on, Miller and Sweatt (2007) discovered that after fear conditioning, rats showed upregulated levels of DNMT3a and DNMT3b gene expression in the hippocampus. Following fear conditioning, animals typically show greater levels of freezing behavior even in the absence of aversive stimulation in the given context. However, the administration of DNMT inhibitors zebularine or 5-aza-2'-deoxycytidine right after fear conditioning resulted in decreased learning measured in reduction of freezing behavior. When these treated rats were trained again 24 hours later, they performed just as well as the non-treated rats. This supports that DNMTs have a central role in learning. A more recent study assessing widespread genomic alternations also found a correlation between DNA methylation and hippocampal-dependent learning (Duke et al., 2017). The study reported coordinated increasing DNA methylation changes in CA1 from 1 h to 24 h after fear conditioning. These results indicate the importance of dynamic alterations in methylation status in forms of long-term hippocampal-dependent memory formation.

Since stability and persistency are defining features of memory, the role of methylation in memory maintenance has been assessed. Miller et al. (2011) reported that when inducing persistent, gene-specific hypermethylation in the rat cortex employing a single hippocampus-dependent contextual fear conditioning, followed by pharmacological inhibition of methylation after 30 days, remote memory was impaired. This supports that the adult brain relies on DNA methylation in maintaining memories over long periods of time.

The indirect role of TDG in transcription of memory-associated genes has been reported in a series of studies. For example, did Levenson et al. (2006) find that when employing general DNMT inhibitors, DNA methylation in the adult brain was altered, as well as the DNA methylation profile of the plasticity-promoting genes brain-derived neurotrophic factor (BDNF) and reelin. Furthermore, mechanisms of DNA modification underlying synaptic plasticity in the hippocampus is central in linking TDG to neural memory correlates. LTP and LTD in Schaffer collateral-CA1 synapses have been assessed in the context of methylation. In 2010, Feng et al. generated a mouse model with a double conditional knockout (DKO) for DNMT3a and DNMT1 genes. The mice had was reported to have significantly weakened hippocampal LTP, as well as being more susceptible to LTD induction, than wild type mice. The DNMT3a/DNMT1 DKO mice also showed impaired MWM performance. Single knockout mice (SKO) for either DNMT3a or DNMT1 executed the task as expected. Furthermore, the DKO mice showed impaired memory consolidation after fear conditioning. Suggesting that DNMT3a and DNMT1, and thus methylation, play important roles in synaptic memory regulation in the hippocampus.

#### 1.4.4.2 DNA Demethylation and Memory

DNA methylation might be necessary for inhibiting transcription of genes related to memory formation. Thus, DNA demethylation might support activation of gene expression associated with neural plasticity correlates for learning and memory (Figure 5). Sweatt and Miller (2007) observed that reelin, involved in LTP induction, showed a reduced methylation profile and increased reelin expression in the hippocampus in fear-conditioned rats compared to control rats. Furthermore, the plasticity-promoting gene, BDNF, is less methylated and show increased transcription in animals after being presented with learning conditions (Day & Sweatt, 2010). These findings illustrates the importance of demethylation of memory-associated genes in memory formation.

The demethylation enzyme TET1 has been investigated in relation to hippocampal memory formation. Kaas et al. (2014) utilized a viral-mediated approach to overexpress the TET1 enzyme in the hippocampus to test regulation of 5hmC level through demethylation and its potential involvement in neural plasticity. The data showed that *Tet1* acts as a regulatory gene for neural activity and that its overexpression correlates with changes in global adapted C levels. In addition, using an adeno-associated virus-mediated method to overexpress the catalytic domain of *Tet1* or the catalytically inactive mutant variant (*Tet1m*), specifically in the hippocampus, it was discovered that the active *Tet1* facilitated hydroxylation of 5mC, leading to active demethylation *in vivo*. Overexpression of *Tet1* or *Tet1m* resulted in an increase in the expression of numerous immediate early genes related to memory, and a specific impairment in the long-term contextual fear memory was observed.

Furthermore, Rudenko et al. (2015) discovered that *Tet1* knockout mice (*Tet1*KO) exhibited significantly lower levels of multiple neuronal activity-regulated genes, including *Npas4*, *c-Fos*, and *Arci,* compared to control mice. The *Tet1*KO model showed atypical hippocampal LTD. Further analysis indicated that the promoter region of *Npas4*, enclosing numerous CpG dinucleotides, was hypermethylated both in naïve *Tet1*KO mice and after memory extinction training. This may account for the impairing transcriptional programs underlying memory processes.

Overall, these studies indicate that the dynamic nature of DNA methylation and demethylation might be essential for hippocampal-dependent memory formation as it is involved in controlling the expression of genes related to synaptic plasticity. The role of TDG in spatial memory formation is still elusive, and more research is needed to fully understand the complete role of DNA glycosylases in memory. Based on experimental evidence of DNA methylation and demethylation in learning and memory and the established role of TDG in active DNA demethylation, it is plausible to assume that this enzyme may be involved in epigenetic modifications critical for the formation and maintenance of spatial learning and reference memory. It is, therefore, of interest to investigate the role of TDG in spatial learning and memory.

### 1.5 Aims and Research Questions

The main aim of this study is to elucidate whether TDG has an impact on the functional plasticity of place cells in the hippocampal CA1 area. This is examined by assessing the following set of research questions.

I. Whether TDG impacts the distributive proportion of place cells in CA1.

II. Whether TDG has an impact on the spatial specificity of CA1 place cells.
III. Whether TDG has an impact on the spatial global remapping of CA1 place cells.
IV. Whether TDG has an impact on the spatial stability of CA1 place cells.

# 2. Materials and Methods

## 2.1 Animal Work

### 2.1.1 Animal Work and Ethical Statements

All animal work performed in relation to this project were carried out in compliance with the Animal Welfare Act and the guidelines directed by the Norwegian Food Safety Authority (Mattilsynet). The experimental procedures were approved in "forsøksdyrforvaltningens tilsyns- og søknadssystem" (FOTS). For details, see FOTS application 24310. All animal work was executed in concession with the principles of the three Rs (replacement, reduction, and refinement; Russell and Burch, 1959), for example, by reducing the number of subjects by extracting as much data as ethically contemplated from each animal. The use of research animals was considered inevitable in this research context. As to my knowledge, there was a lack of sufficient data on the effects of TDG on the hippocampal memory system to simulate comprehensive experiments, to my current knowledge.

Housing, handling, and experimentation involving animals took place in an approved animal facility, the Comparative Medicine Core Facility (CoMed) at St. Olavs Hospital. The mice were housed in a specific pathogen-free unit (SPF) with a 12 h reversed light/dark cycle (light 18:00-06:00), with 55-65% relative humidity and 23 ± 2°C. The animals were housed individually in ventilated cages with enriched environments and free access to food (Ssniff) and water. Physical health and well-being were assessed daily.

### 2.1.2 Mouse Model

The transgenic mouse model used in these experiments was developed from the initial female CamKIIα-Cre mice (Schwarz et al., 2020) from the Jackson laboratory (T29-1, stock #005359) by a colleague in the research group. The mouse model was developed by a CamKIIα promoter to achieve a conditional knockout of *Tdg*. This promoter exclusively regulates the gene expression in excitatory neurons, mainly in the pyramidal layer of the hippocampal area CA1 (Wang et al., 2013). The establishment of an adult Cre/loxP recombination pattern appears by p29 (Eagle et al., 2016). Upon introduction of Cre-recombinase, the mini*Tdg* gene and the GFP stop codon, were excised. The transgenic mouse model (CamKIIα-*Tdg*$^{-/-}$) used in this study contains a loxP flanked mini*Tdg* and enhanced GFP (eGFP) sequence following a LoxP-STOP-LoxP cassette. Additionally, the mouse model contains a CamKIIa promoter controlling Cre expression in hippocampal neurons at p29 (Eagle et a., 2016). This enables a conditional knockout of the flanked mini*Tdg* gene in adult animals. Another second-generation genetic outcome, without Cre-recombinase, was used as controls (mini$Tdg^{+/+}$, Wt-$Tdg^{-/-}$, and CamKIIα-$Cre^{-/-}$). All included mice were adult (3-6 mnd.) males.

### 2.1.3 Genotyping

Initial genotyping of mice was verified by Polymerase chain reaction (PCR), using genomic DNA from ear biopsies. The mouse ear samples were firstly lysed with lysis buffer (10 mM Tris, 1M KCl, 0,4% NP-40/lgepal CA630 Sigma, 0,1% Tween20) and protein kinase K (10 mg/ml), and secondly incubated at 60°C overnight. The samples were then heated at 95°C for 30 min following 14000rpm centrifugation for 20 min. Preparations (diluted 1:10 in $ddH_2O$) were subsequently combined with $ddH_2O$, Taq 2x Master Mix (10x PCR buffer, 5U/µl paq5000, 2.5 mM dNTPs, 50 mM $MgCl_2$), and 0,5 µm of each primer pair, depending on strain analyzed. The total volume of the solution was 10 µl. A list of primers is presented in Appendix C. The PRC parameters were set to 3 min at 95°C before 42 cycles comprising 30 sec at 95°C, 30 sec at 64°C, and 30 sec at 72°C, followed by a 5-minute extension at 72°C before samples were confined at 4°C ∞. PCR products were subsequently separated using 2% (w/v) agarose gel electrophoresis, arranged with agarose (BioNordika LE Agarose), 0,001% SybrSafe (Thermoficher/Invitrogen), and TAE buffer (Tris base, Glacial Acetic Acid, 0,5 EDTA). A 100bp DNA ladder was used to determine the PCR product size. The PCR reaction supplemented with 6x DNA loading dye (New England Biolabs) was loaded into the gel and run at 120V electrophoresis for 40min. Results were visualized by UV exposure image acquisition using a ChemiDocäMP system (BIORAD).

## 2.2 Electrophysiology

### 2.2.1 Microdrives

MDR-xx Microdrives from Axona (Axona Ltd.) were wired with 4 tetrodes, each consisting of 4 platinum and 10% iridium alloy wire electrodes (California Fine Wire Co., USA) making a 4x4 electrode composition. The coiled connections between the drive wires and the electrodes were coated with electrically conductive silver paint (Electrolube) and insulated with nail polish (HM; Figure 6). The tetrodes were cut to a length of between 5 and 7 mm and subsequently plated with platinum (Neuralynx) using electrolysis, generated with a 10 MHz pulse generator (Thurlby Tandar Instruments), and amplified by Axona DasqUSB stimulus isolator (Axona Ltd.). The impedance was adjusted to approximately Z = 200kΩ, measured by a multimeter (Escort Instrument Corporation) using a 1k Hz measuring frequency. Short-circuits were controlled for by measuring the resistance between each pin on the connector of the drive with a multimeter (Fluke).

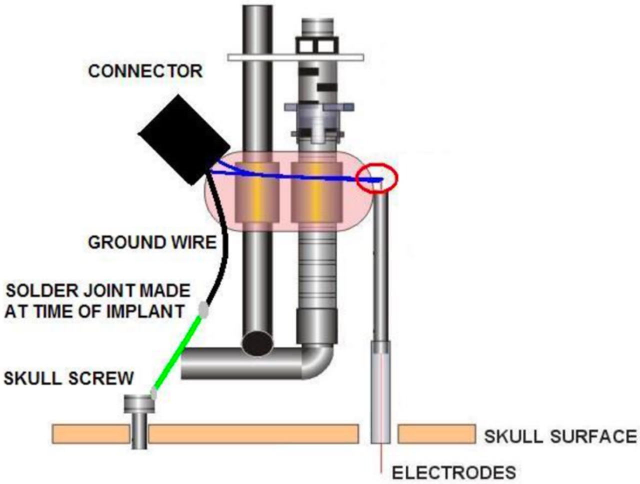

***Figure 6. Illustration of implanted Microdrive.*** Illustration of a fully constructed microdrive implanted in a scull. The figure was obtained from the AXONA Ltd. MDR-xx Microdrive User Guide (Axona Ltd.).

### 2.2.2 Surgical Electrode Implantation

Prior to implantation of tetrodes, animals were deeply anaesthetized (isoflurane 1,5-2%, $O_2$ 2%). Local analgesia was administered with a subcutaneous injection of Marcain (0,04 ml/20 g) and systemic analgesia via intraperitoneally injection of Temgesic (0,03 mg/ml) and Metacam (0,5 mg/m). Anaesthesia was upheld by sustained administered isoflurane (0.6% in pure $O_2$) throughout the surgery. Anaesthesia depth was controlled by monitoring respiratory rate. The mouse was fixed with a stereotaxic instrument and kept on a heating pad at 37 °C, to avoid hypothermia during the surgerical procedure. The eyes were protected by Viscotears eye gel (BAUSCH+LOMB). A 2 cm incision was made, exposing the skull, before excess skin and debris covering the area were removed. Two cranial boreholes were drilled, for the grounding screw and for tetrode insertion, following stereotactic coordinates relative to the bregma: AP[Bregma]: 0.2 mm, ML: 0.5 mm and AP[Bregma]: -2 mm, ML: -1.8 mm, respectively. The hole for the tetrodes were covered with a saline-soaked haemostatic gelatine sponge (ETHICON), as the surface of the cranial bones were scratched with a 19G needle and coated with histoacryl (B|BRAUN). After removing the sponge, small parts of the dura mater were removed to allow penetration of the tetrodes. The tetrodes implanted at the relative coordinates: AP[Bregma]: -2 mm, ML: -1.8 mm, DV: -0.8 mm. The cannula sleeve was lowered and covered with a layer of sponge to protect the exposed tetrodes (Figure 6). The revealed skull was subsequently covered with dental acrylic, which served as a fundament for the microdrive. After surgery, the animals were administered Metacam (2 mg/kg) and Baytril (2 mg/kg) for two days and monitored daily until euthanasia.

### 2.2.3 Electrophysiological Recording

Extracellular *in vivo* electrophysiology was performed to assess spatial cell properties of CamKIIα-*Tdg*$^{-/-}$ mice. The screening for cells began approximately one week after implantation surgery. All recordings were performed in a soundproof, dimly lit room with the recording set-up elevated on a table enclosed by lightproof curtains. Recordings took place during the dark cycle, starting at least a week after the mice were introduced to the reversed light cycle. The main recording box (50Lx50Wx30H) had black walls with a white cue card on one of the walls and was placed on a black antistatic mat. To reduce olfactory cues, equipment exposed to the animals was cleaned with lemon-scented soap and water between trials. A counterbalanced cable was suspended above the recording box connecting the headstage (Axona Ltd.) to the microdrive. The signal was amplified (100x amp) in a preamplifier (Axona Ltd.) a system unit (Axona Ltd.) and recorded in DacqUSB (Axona Ltd.).

Raw unit activity was monitored for each channel and filtered with a bandpass filter (300-7000 Hz). Gain and threshold were based on individual channel signal for each trial. Reference channels for each distinct trial were selected based on signal and channel activity. A Bessel lowpass filter was applied to the EEG signal rejecting frequencies over 1000 Hz and reference channels were set to channels with high spiking frequency.

Points were stored when signals exceeded the given threshold (a presumptive spike), and each spike event was labelled with relative time and the position of the animal. A video camera (CBC co., Ltd.) was fixed above the recording box and monitored subject location during unit recording. To enable HD recording and path tracking the headstage was mounted with two LEDs. Locations were converted into x, y coordinates by the tracking system (Axona Ltd.).

The tetrodes were initially advanced by >50 µm daily and recordings were performed in time intervals of 10 min. When hippocampal ripples and sharp waves appeared, tetrode advancements decreased to 25 µm increments to monitor new CA1 cells. When place cells were isolated, recordings were performed in 20 min time intervals. Crumbs of a chocolate flavored cereal (Weetabix) were spread out in the box to motivate the mice to move.

### 2.2.4 Analysis of Place Cell Activity

Initial analysis of cell activity to determine the identity of cells were performed offline in a cluster-cutting program (Tint, Axona Ltd.). Collected waveforms were displayed as clusters, plotting each spike’s peak amplitude on one electrode against each of the other three. The clusters were separated by hand, based on manual cut derived parameters or by implementing an automatic clustering algorithm provided by the software (see e.g. in Figure 10A-C).

To determination place field and cell activity correlates, the captured recoding area was divided into a 64x64 grid. Each spike point was located at the center of a square bin. Place fields was defined as regions of location specific firing related to clearly isolated cell clusters and were only analyzed if the specific firing pattern was stable over several trials in the same condition.

### 2.2.5 Remapping and Stability Testing

To enter the remapping and stability recoding analysis, a screened cell had to hold the properties of a stable place cell, that is, a completely isolated cluster with firings restricted to one or several localized regions of the given environment. Subsequently after recognition of a place cell, remapping and short-term stability experiments were performed. The paradigm consisted of recordings in two open field boxes, henceforth referred to as box A and B. Box A was the same as the one used for the initial unit recordings and box B had corresponding properties, but white walls and a black cue card placed on a different wall. The mice were recorded for 20 min in box A, followed by 20 min of recording in box B for two succeeding trials, before a 20-minute recording in box A (Figure 7A.). Cell remapping recordings were alternated in two-trial blocks, in box B, to confirm remapping and check that apparent activity patterns were not due to electrode movement. In between trials the mouse was held in its housing cage for 3 min. Long-term stability was assessed with a recording interval for 20 min in box A, 24 h after the second recoding in box A (Figure 7B). All concurrent trials were performed at the same tetrode depth and with identical software set-up.

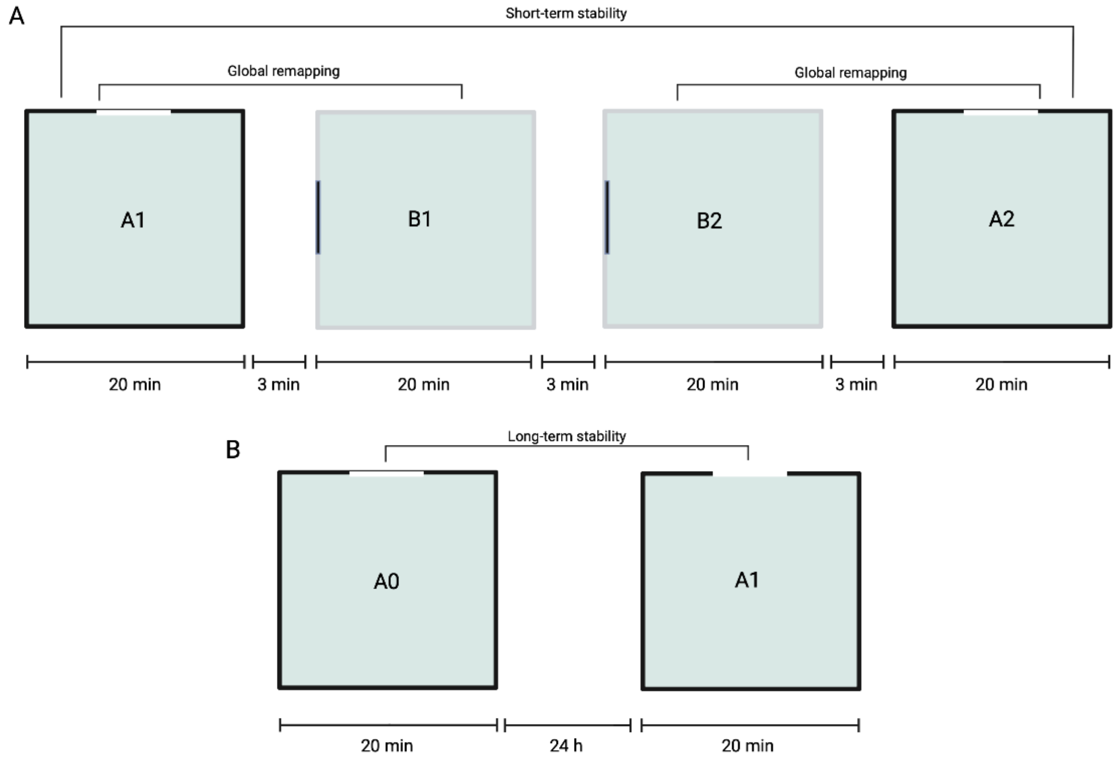

***Figure 7. Experimental design of the remapping and stability paradigm*. A|** Open field area used for the global remapping and short-term stability experiments. A Arenas (A1, A2) are indicated with black walls and a proximal white cue card and B arenas (B1, B2) with white walls and a proximal black cue card, monitoring remapping with identical intertrial intervals (3 min) between A and B environments. Stability is monitored using same boxes (A1 and A2 or B1 and B2). **B|** Open field area used for long-term stability testing between A0 and A1 with 24 h intertrial interval. The figure was made in BioRender.

## 2.3 Perfusion

Animals were perfused with 0.9% saline before the brain was extracted for further experimental analyses. During the procedure mice were firstly anaesthetized with isoflurane and subsequently intraperitoneally administered pentobarbital (100 mg/ml, 0.01 ml/g; Norges Apotekerforening). Evaluation of paw and tail pain reflexes indicated appropriate anaesthetic depth. The mouse was then fixed in a supine position and a thoracic incision aligning the midline, opening the anterior chest wall was made, exposing the sternum. Afterwards, the sternum and surrounding ribcage were cut, creating an open chest cavity to uncover the heart. Descending aorta was subsequently clamped shut using a hemostatic clamp, before puncturing the right atrium. Successively, 60 ml of 0.9% saline solution was gradually injected with a needle (18G) attached to a three-way stopcock (Braun), into the left heart ventricle.

For the mice with implanted microdrives, the head was decapitated after perfusion and suspended in 4% paraformaldehyde/PBS solution for at least 24 h. The tetrodes were elevated out of the brain tissue, and all external tissue and cranial bones were removed ventral to dorsal, following extraction of the brain which was fixed in 4% paraformaldehyde (PFA) in PBS.

## 2.4 Cryo-Sectioning

After perfusion, the right hemisphere was fixed in 4% paraformaldehyde (PFA)/PBS for at least 48 h. The tissue was then frozen with aerosol freezing spray (PRF 101/502 ML GREEN NFL) before being cut into sagittal sections (30 µm), using a cryostat (CryoStar NX40, Thermo Fischer) with object and chamber temperature at -20°C. The tissue was cryogenically conserved during the procedure. Medial and lateral sections were mounted directly on to histological glass slides and stored at -20°C.

## 2.5 Histology and Axioscan Microscopy

Mounted brain sections were stained using a modified cresyl violet procedure a week after cutting. The slices were firstly soaked in distilled water for 2 min, before dehydrated them by sequentially dipping the mounted slices 10 times up and down in ethanol solutions (70% - 80% - 90% - 100%), made of diluting absolute ethanol (VWR Chemicals) and distilled water. Subsequently, the slices were placed pure xylene (Sigma-Aldrich) for 2 min before being rehydrated in ethanol solutions (100% - 90% - 80% - 70%) sequentially, and places in differentiation solution (0.5% acetic acid and 70% ethanol) for 5 min. Afterwards, the slices were cleaned in distilled water, before they were stained in cresyl violet solution (30 ml of a stock solution (0.2 g cresyl violet-acetate (Sigma-Aldrich) in 150 ml distilled water and 300ml pH 3.5 buffer solution (282 ml of 0.1 M acetic acid (Sigma- Aldrich)) and 18 ml of 0.1 M sodium acetate (Sigma-Aldrich)) for 8 min. The slices were rinsed by alternating dripping them into water and differentiation solution until appropriate color contrasts. The slides were then dehydrated in ethanol solutions (70% - 80% - 90% - 100%) subsequently and placed in xylene for 10 min. finally the mounted slices were sealed with cover glass, using Eukitt mounting oil.

## 2.6 Statistical Analysis

All data was organized in Microsoft Excel. The pre-processing of cell physiology data was performed in MATLAB (Mathworks) emplying the Behavioural Neurology Toolbox (BNT) toolbox, developed at the Kavli Institute of Systems Neuroscience (NTNU). The pre-processing of cell physiology data was performed by a fellow colleague in the research group. Using the BNT toolbox, spatial information content, spatial information rate, average firing rate, Pearson correlation coefficient of within-session spatial stability, HD scores, speed scores, place field size, place field peak firing, number of fields for each cell, rate maps, shuffling, and Pearson correlation coefficient of rate maps between sessions was extracted. All statistical analyses were performed in SPSS Statistics (IBM). Plots was created in GraphPad Prism 9 and SPSS Statistics (IBM).

### 2.9 Key Resources

***Table 1. Summary of used resources***

| **RESOURCE** | **SOURCE** | **IDENTIFIER** |
|---|---|---|
| **Chemicals** | | |
| Acetic acid | Sigma-Aldrich | CAS 64-19-7 |
| Cresyl Violet Acetate | Sigma-Aldrich | CAS 10510-54-0 |
| Ethanol absolute | VWR Chemicals | CAS 64-17-5 |
| Eukitt Mounting Medium | Sigma-Aldrich | CAS 25608-33-7 |
| PBS | VWR Chemicals | E404-100TABS |
| Sodium acetate | Sigma-Aldrich | CAS 6131-90-4 |
| Xylene | Sigma-Aldrich | REACH 01-2119488216-32-XXXX |
| **Mouse models** | | |
| CamKIIα-*Tdg*$^{-/-}$ | Bred by the research group | |
| LoxP-*miniTdg* | Bred by the research group | |
| **Surgical materials** | | |
| Eye Gel | | https://www.medicines.org.uk/emc/product/2310/smpc |
| Haemostatic gel sponge | Ethicon | https://www.jnjmedtech.com/en-EMEA/product/spongostan-absorbable-haemostatic-gelatin-sponge |
| Histoacryl | B\|Braun | https://www.bbraun.com/en/products/b/histoacryl.html |
| MELIODENT Rapid repair liquid | Kulzer GmbH | https://www.kulzer.com/int2/en/products/meliodent-rr.html |
| MELIODENT Rapid repair powder | Kulzer GmbH | https://www.kulzer.com/int2/en/products/meliodent-rr.html |
| Saline 0.9% | B\|Braun | https://www.bbraun.com/en/products/b0/nacl-0-9-b-braun.html |

| **Drugs** | | |
|---|---|---|
| Baytril | Bayer Animal Health GmbH | https://www.felleskatalogen.no/medisi n-vet/baytril-vet-bayer-animal-health-gmbh-546731 |
| Isoflurane | Baxter | ATC N01A B06 |
| Marcain | Aspen Pharma | https://www.felleskatalogen.no/medisin/pasienter/pil-marcain-aspen-561225 |
| Metacam | Boehringer Ingelheim | https://www.boehringer-ingelheim.com/animal- health/livestock-products/metacam |
| Pentobarbital NAF | Norges Apotekerforening | ATC QN51AA01 |
| Temgesic | Indivior | https://www.felleskatalogen.no/medisin/temgesic-indivior-564488 |
| **Software** | | |
| ANY-maze | Stoelting Co. | https://www.any-maze.com/ |
| BioRender | BioRender | https://biorender.com/ |
| dacqUSB | Axona Ltd. | https://www.axona.com |
| Excel v.2201 | Microsoft | https://www.microsoft.com/en/ |
| MATLAB R2021a | Mathworks | https://se.mathworks.com/ |
| Tint graphical clustering software | Axona Ltd. | https://www.axona.com |
| GraphPad Prism 9 | | |
| SPSS Statistics (IBM). | | |
| **Hardware** | | |
| Axioscan | Zeiss | https://www.zeiss.com/ |
| dacqUSB Preamp | Axona | https://www.axona.com |
| dacqUSB System Unit | Axona | https://www.axona.com |
| Elc-131d LCR meter | Escort Instruments Co. | |
| GANZ CCD color camera | CBC Co. Ltd | |
| Headstage | Axona | https://www.axona.com |

|  |  |  |
|---|---|---|
| MDR-xx Microdrives | Axona | https://www.axona.com |
| Platinum and 10% iridium alloy wire | California Fine Wire Co. | https://calfinewire.com/ |
| Pulse Generator TGP110 10MHz | Thurlby Tandar Instruments | https://www.ttid.co.uk/pulse-generators/aim-tti/tgp110 |
| Stimulus isolator | Axona | https://www.axona.com |
| **Other** |  |  |
| Cold spray | Taerosol | 101 Cold spray Green Non-flammable - Taerosol |
| Platinum plating solution | Neuralynx | https://neuralynx.com/hardware/platinum-black-plating-solution |
| Silver Conductive paint | Electrolube | https://electrolube.com/ |
| V1536 | Ssniff | https://www.ssniff.com/index.php?pcid=9&pdid=15 |
| Wheetos Choco | Weetabix | https://weetabix.no/our-products/weetos/weetos/ |

## 3 Results

To evaluate whether TDG is associated with the spatial representational system in the mouse hippocampal area CA1, a series of analyses of the electrophysiological recording data was conducted. The following section will report the results derived from data collected by electrophysiological recordings.

### 3.1 Verification of genotype

The mouse model, CamKIIα-*Tdg*$^{-/-}$ was used to investigate the effect of TDG in spatial cell properties of the hippocampal CA1. This particular mouse strain has a conditional *Tdg* knockout (KO) specifically affecting excitatory neurons, mainly concentrated in the CA1, but also other hippocampal subareas. The model was generated by a fellow associate in the research group, derivate from the Tg(CamKIIα-Cre)T29 mice strain from the Jackson laboratory (T29-1, stock #005359) (Schwarz et al., 2020). The resulting offsprings used as the CamKIIα-*Tdg*$^{-/-}$ (knockout) mouse model had genetic markers for mini*Tdg*$^{+/+}$, Wt-*Tdg*$^{-/-}$, and CamKIIα-Cre$^{+/-}$. The model used as controls (LoxP-miniTdg) had the genetic information of mini*Tdg*$^{+/+}$, Wt-*Tdg*$^{-/-}$, and CamKIIα-Cre$^{-/-}$. Specific genotypical markers were confirmed with PCR and gel electrophoresis. Of the mice used for electrophysiological recordings, 4 were confirmed to have genetic markers for the

CamKIIα-*Tdg*$^{-/-}$ strain, and 4 were confirmed to have markers for the control strain (LoxP-mini*Tdg*). Of these, cells from 2 control mice and 2 CamKIIα-*Tdg*$^{-/-}$ mice were included in the following electrophysiological data analysis.

### 3.1 Microdrives

In total, 10 MDR-xx Microdrives (Axona Ltd.) were successfully wired (e.g. in Figure 8), and 8 of these were implanted and used for electrophysiological recording. Among the mice implanted with drives (*n* = 8), 1 was terminated due to issues with the electrical signal. 4 of the mice (*n* = 4) with microdrive implants were included in the current analysis. The tetrodes wired to the drives used in the mice included in the analysis (*n* = 4) were 5-6 μm in length. No short circuits between electrodes were detected and all channels had good electrical conductance, with impedance (resistance) varying from Z = 120 kΩ to Z = 280 kΩ in each electrode in each included drive. The resistance of each electrode was justified to be approximately the same value. Larger resistance differences were seen between tetrodes (for exact resistance measurements, see Appendix A). Over the course of recording, one of the drives implanted in the mice included in the following analysis (*n* = 4) acquired an impaired electrode (drive 2, channel C; see Appendix A). This drive was implanted in a control mouse.

***Figure 8. Microdrive.*** Picture of a completed microdrive.

### 3.2 Determining Tetrode Trajectory

Scanning of stained brain slices was performed successfully, but a formal confirmatory analysis of tetrode trajectory and location was not conducted due to time constraints.

### 3.3 Cell Physiology

In order to examine the effects of TDG on the quantity and functional features of cells in the hippocampus, I recorded the activity of CA1 neurons in mice (*n* = 4 control and *n* = 4 CamKIIα-*Tdg*$^{-/-}$ mice) when exploring in an open-field environment (50x50 cm). Due to time constraints, cells from 4 of the implanted mice (*n* = 8) were included in the analysis. Of these, 2 were control mice and 2 were CamKIIa-*Tdg*$^{-/-}$ mice. The normal distribution of all samples was investigated using a Shapiro-Wilk test (if $N < 50$) or a Kolmogorov-Smirnov test (if $N > 50$). Arithmetic mean (*M*) and standard deviation (*SD*) are reported for all tests.

#### 3.3.1 Cell Clustering

In order to separate and cluster spikes from different cells in the recorded animals, I used the offline graphical clustering software Tint (Axona Ltd). The recorded data points, each point representing a single spike, were distributed across a two-dimensional feature space (Figure 9A). I sorted the spikes into clusters based on various parameters, including the distance between the peak and the trough of the waveform, voltage as a function of time, amplitude of the peak and trough, time of peak and trough, or I used principal components derived from a principal components analysis (PCA) performed by Tint in particularly challenging feature space distributions. See Figure 9 for an example of the clustering procedure.

Using the feature space, I manually grouped the data points into cell clusters. These clusters were subsequently examined for divergence in waveforms and cleaned for potential noise and spikes belonging to other cells (Figure 9B). The temporal characteristics of the electrical activity were also examined based on an autocorrelation of a given clustered cell (Figure 9C). The absolute refractory period of 2 ms, during which a given neuron cannot fire another action potential, was taken into consideration. A cell cluster including spikes occurring less than 2 ms apart, required more cleaning. An example of the waveforms obtained through the clustering process is presented in Figure 9B. Following spike sorting, a rate map, a trajectory map, and a polar map of each cell's activity were generated in Tint (Figure 9D). These maps provided a visual indication of whether the cell was spatially tuned. In total, 254 cells from the two control mice and 252 cells from the two CamKIIα-*Tdg*$^{-/-}$ mice were clustered for further analysis.

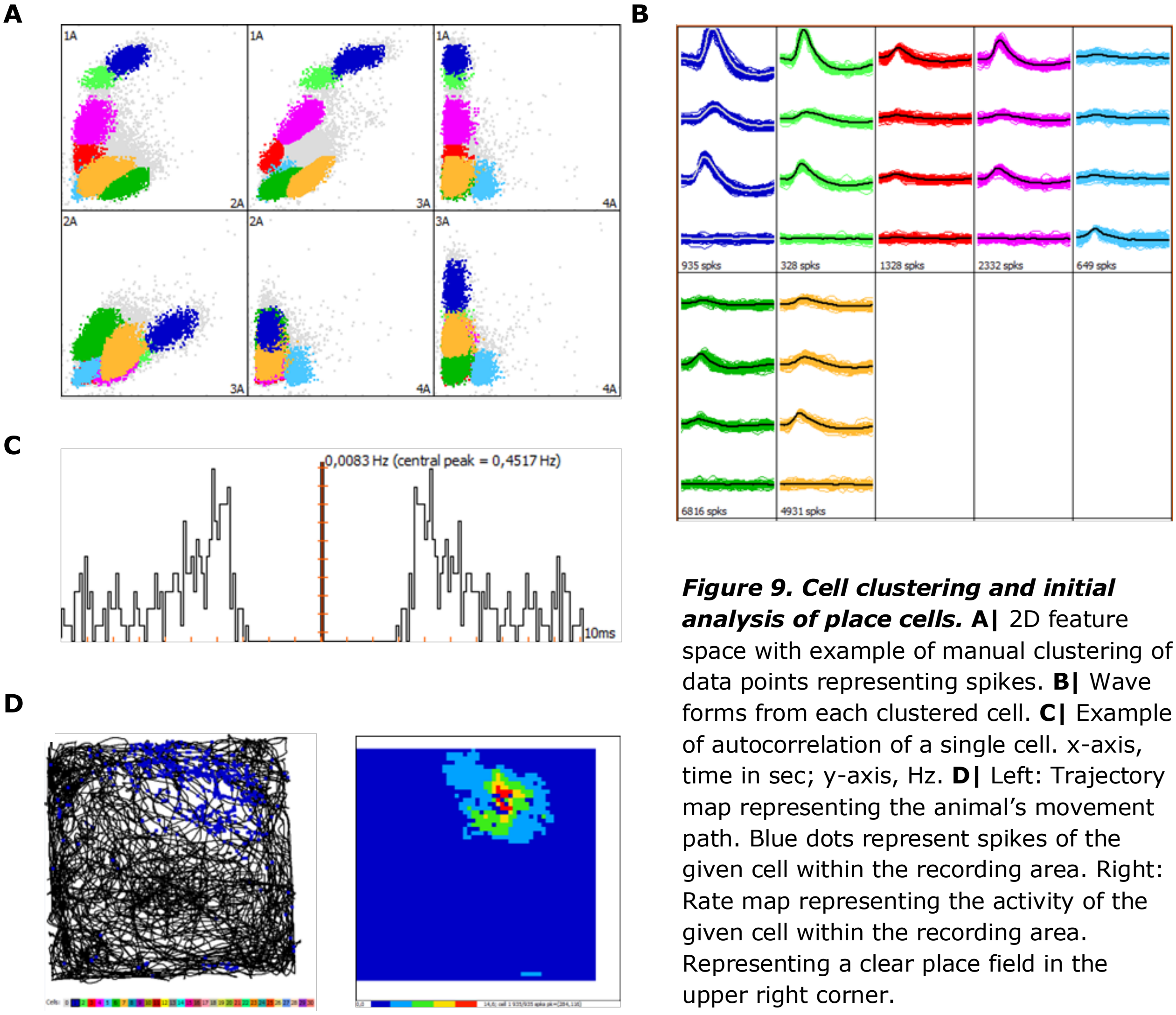

***Figure 9. Cell clustering and initial analysis of place cells.*** **A|** 2D feature space with example of manual clustering of data points representing spikes. **B|** Wave forms from each clustered cell. **C|** Example of autocorrelation of a single cell. x-axis, time in sec; y-axis, Hz. **D|** Left: Trajectory map representing the animal's movement path. Blue dots represent spikes of the given cell within the recording area. Right: Rate map representing the activity of the given cell within the recording area. Representing a clear place field in the upper right corner.

### 3.3.2 Cell Type Classification and Distribution

A total number of 506 recorded CA1 cells from 2 control mice and 2 CamKIIα-*Tdg*$^{-/-}$ mice were included in this analysis. 50.2% ($n$ = 254) of these belonged to the mice of the control group and 49,8% ($n$ = 252) belonged to the mice of the CamKIIα-*Tdg*$^{-/-}$ group. A series of different variables were used as inclusion criteria for each category of cells. Included CA1 cells from control and CamKIIα-*Tdg*$^{-/-}$ groups were analyzed as separate populations. A summary of statistics for the classification and distribution of cell types is presented in Table 2. Parameters used for classification of cell types are presented in Appendix G.

#### 3.3.2.1 Place Cells

Information metrics for spatial coding by neuronal spikes were studied to identify place cells. Place cells were classified by first calculating the spatial information content, a measure of the amount of information about the animal's location that is carried out by the firing properties of the cell. This calculation was based on the information theoretic approach formulated by Skaggs, McNaughton, and Gothard (1992). The information content equation is:

$$I = \sum p_x \left(\frac{\lambda(x)}{\lambda}\right) \log_2 \left(\frac{\lambda(x)}{\lambda}\right)$$

I = the information content in bits per spike for each cell
x = the bin number
P(x) = the probability for the mouse being at bin x
$\lambda(x)$ = the mean firing rate when the mouse is at x
$\lambda$ = the total mean firing rate of the cell.

Afterward, the data was shuffled by randomly redistributing the spikes of a cell across the path of the animal. Each shuffle iteration was completed 100 times. For shuffled and observed values of the spatial information content, see Appendix E. Then, the cell activity in which the animal was moving less than 2 cm/sec and above 100 cm/sec, the cells with fewer than 100 spikes, the cells with firing rates lower than 0.1 Hz and higher than 7 Hz, and the cells without a clear place field were filtered out. The remaining cells passing a 95th percentile cut-off criteria for spatial information content were categorized as place cells. Rate maps of the place cells were calculated by adding up the spikes correlating with each location within the A1 recording arena divided by the amount of time the mouse spent in the given location. Locations were binned in 2.5 cm bins. The maps were subsequently smoothed by a Gaussian distribution in each bin center. A total of 59 (11.66% of the total cell number) cells were classified as place cells, of these, 33.9% (*n* = 20, 7.87% of the total cell number in this condition) belonged to the control group and 66.10% (*n* = 39, 15.48% of the total cell number in this condition) to the CamKIIα-*Tdg*$^{-/-}$ group, as shown in Table 2 (Figure 10A). I conducted a Pearson Chi-Square test to examine the difference between the number of place cells in the control group (*M* = .08, *SD* = .27) and in the CamKIIα-*Tdg*$^{-/-}$ group (*M* = .15, *SD* = 36). Results indicated a significant difference in the proportion of place cells between the groups, $X^2(1, N = 506) = 7.10, p = .008$.

Furthermore, the stability of place fields was calculated by correlating the rate maps between the first half (10 min) and the second half (10 min) of the recording session, defined as within-session stability. Normal place cells are expected to have a high correlation (between ± .50 and ± 1.00) between the two halves (Kunath et al., 2021). The total amount of place cells (*N* = 59) had a moderate within-session spatial stability score of .34, with a standard deviation of .30. A Mann-Whitney U test was performed as the distributions were not normal. The test revealed that there was not a significant difference between the control group (*n* = 20, M = .32, SD = .33) and the CamKIIα-*Tdg*$^{-/-}$ group (*n* = 39, M = .34, SD = .29), *U* = 401.00, *p* = .860. 40% (*n* = 8) of the cells from the control group and 30,77% (*n* = 12) of the cells from the CamKIIα-*Tdg*$^{-/-}$ group had strong within-session spatial stability scores (*r* > .50; Figure 10B). A one-way ANOVA was performed and significant differences between the control cells displaying high within-session stability score (*n* = 8, *M* = .71, *SD* = .12), control cells with low-moderate within-session stability score (*n* = 12, *M* = .07, *SD* =.05), CamKIIα-*Tdg*$^{-/-}$ cells with high within-session stability score (*n* = 12, *M* = .71, *SD* = 12), and cells with low-moderate within-session stability score (*n* = 27, *M* = .18, *SD* = .16) was detected, *F*(3, 55) = 79.86, *p* < .001. A Tuckey HSD post hoc test identified significant differences between control cells with high and low-moderate within-session stability correlation scores, *p* < .001, between CamKIIα-*Tdg*$^{-/-}$ cells with high and low-moderate scores, *p* < .001, and between control cells with low-moderate scores and CamKIIα-*Tdg*$^{-/-}$ cells with high scores, *p* < .001. Between the control cells with low-moderate within-session stability scores and the CamKIIα-*Tdg*$^{-/-}$ cells with low-moderate scores, the difference was also significant, in which the CamKIIα-*Tdg*$^{-/-}$ cells displayed lower mean correlation, but higher within-group variability, *p* = .011. A significant difference was not detected between the control cells with high within-session stability scores and the CamKIIα-*Tdg*$^{-/-}$ with high scores, but the variability for the CamKIIα-*Tdg*$^{-/-}$ group was higher than the control group, *p* = 1.000. A small deviation from normality was observed in one of the groups, but this was not adequate to warrant a non-parametric test. Examples of place cell rate maps, smoothed rate maps, and trajectory maps are presented in Appendix F.

In summary, significantly more place cells were recorded and clustered from the CamKIIα-*Tdg*$^{-/-}$ mice than from the control mice. Cells from both groups displayed moderate within-session stability, slightly deviating from what is expected from normal place cells. Both cell groups had a higher proportion of cells with low-moderate within-session stability than high stability. The CamKIIα-*Tdg*$^{-/-}$ cells had significantly lower stability scores in the low-moderate correlation interval than the control cells.

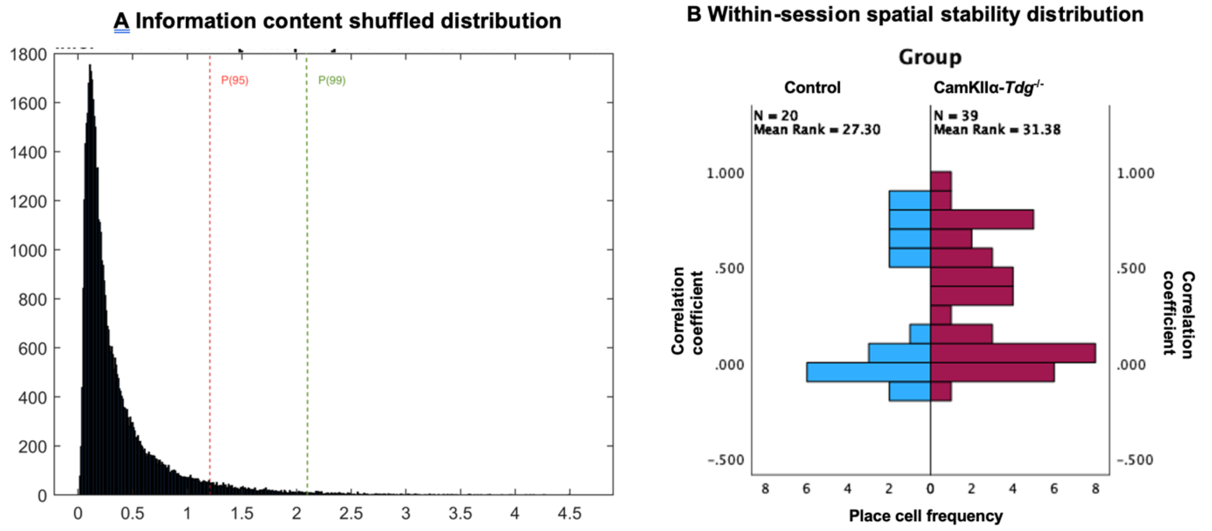

***Figure 10. Place cell distributions as a function of information content and within-session stability.*** **A|** Distributions of the randomly shuffled spatial information scores for the entire cell sample recorded in control and CamKIIα-*Tdg*$^{-/-}$ CA1. The 95th and the 99th percentile of the shuffled distribution are indicated by the red and green dotted lines. The 95th percentile was used as a threshold to define place cells. The figure was made in MATLAB. **B|** Distributions of the place cells in the control group (blue) and the CamKIIα-*Tdg*$^{-/-}$ group as a function of within-session correlation. The figure was made in SPSS.

### 3.3.2.2 Other Spatial Cells

To categorize HD cells, the direction of the mouse head from the relative angle of the headstage LEDs was calculated. To compute the HD score, the HD of the animal as a function of the cell spike was binned into 120 3-degree bins. The mean length of the neural activity vector modulated by head direction was calculated as the head direction score. This score provides an indication of how accurately the spikes are tuned to the preferred angle of the cell. Then, the HD scores were shuffled in the same manner as the information content shuffling. A 95th percentile cut-off was added to the shuffled data. Cells passing this cut-off were classified as HD cells. For shuffled and observed values for the HD scores, see Appendix E. A total of 40 (7.91% of the total cell number) cells were classified as HD cells, of these, 40% ($n$ = 16) belonged to the control group ($M$ = .06, $SD$ = .24), and 60% ($n$ = 24) to the CamKIIα-*Tdg*$^{-/-}$ group ($M$ = .10, $SD$ = .29), as shown in Table 2. A Pearson Chi-Square test showed no significant difference in the amount of HD cells between the genotypes, $X^2(1, N = 506) = 1.81, p = .179$. The distribution of HD cells is presented in Table 2. For examples of polar maps, see Appendix F.

Classification of speed cells was performed by first calculating the speed score by binning the recorded speed from 5 to 100 cm/s to 2 cm/s bins. Then, the bins were correlated with the firing data. The data was then shuffled in an identical manner as the information content and the HD score. A 95th percentile cut-off was applied to classify the speed cells. For shuffled and observed values for the speed scores, see Appendix E. A total of 143 (28.26% of the total cell number) cells were classified as speed cells, of these 75.52% ($n = 108$) belonged to the control group and 24.48% ($n = 35$) to the CamKIIα-*Tdg*$^{-/-}$ group, as shown in Table 2. A Pearson Chi-Square test detected a significant difference between the amount of speed cells in the control group ($M = .43$, $SD = .50$) and in the CamKIIα-*Tdg*$^{-/-}$ group ($M = .14$, $SD = 35$), $X^2(1, N = 506) = 51.15, p < .001$. The distribution of speed cells is presented in Table 2.

Boundary cells were classified using a border score, calculated in accordance with the method used by Solstad et al. (2008). A flawless border score (+1) reflected a thin line (1 px, bin) lying along and fully covering one of the bordering walls of the firing map. The data was then shuffled in an identical manner as for the information content, the HD score and the speed score. A total of 68 (13.44% of the total cell number) cells were classified as boundary cells, of these, 41.18% ($n = 28$) belonged to the control group ($M = .11$, $SD = .31$) and 58.82% ($n = 40$) to the CamKIIα-*Tdg*$^{-/-}$ group ($M = .16$, $SD = .37$), as shown in Table 2. A Pearson Chi-Square test revealed that the difference in proportion was not significant $X^2(1, N = 506) = 2.56, p = .110$. The distribution of boundary cells is presented in Table 2.

To be classified as a conjunctive cell, the cell had to be categorized as a place cell as well as fulfill the criteria of one or multiple other cell groups. A total of 1 (0.2% of the total cell number) cells were classified as place and boundary conjunctive cells, belonging to the CamKIIα-*Tdg*$^{-/-}$ group (0.40% of the total cell number in this condition). A total of 16 (3.16% of the total cell number) cells were classified as place and HD conjunctive cells, of these, 25% ($n = 4$, 1.57% of the total cell number in this condition) belonged to the control group and 75% ($n = 14$, 5.56% of the total cell number in this condition) to the CamKIIα-*Tdg*$^{-/-}$ group. A total of 5 (0.99% of the total cell number) cells were classified as place and speed conjunctive cells, of these 40% ($n = 3$, 1.18% of the total cell number in this condition) belonged to the control group and 60% ($n = 2$, 0.79% of the total cell number in this condition) to the CamKIIα-*Tdg*$^{-/-}$ group. A total of 1 (0.02% of the total cell number) cells were classified as place, HD, and speed conjunctive cells. This cell ($n = 1$, 0.40% of the total cell number in this condition) belonged to the CamKIIα-*Tdg*$^{-/-}$ group. A total of 2 (0.4% of the total cell number) cells were classified as place, boundary, and HD conjunctive cells, of these, 50% ($n = 1$, 0.40% of the total cell number in this condition) belonged to the control group and 50% ($n$ = 1, 0.40% of the total cell number in this condition) to the CamKIIα-*Tdg*$^{-/-}$ group. A total of 0 cells were classified as place, boundary, and speed conjunctive cells. The distribution of conjunctive cells is presented in Table 2.

Overall, the cells were classified into 10 categories. The CamKIIα-*Tdg*$^{-/-}$ genotype group had significantly more place cells, but fewer speed cells than the control group. These findings are of particular importance. The following section will present findings related to the functional properties of the reported place cells.

**Table 2**

*Summary of cell type classification and distribution.*

|  | Control | CamKIIa-*Tdg*$^{-/-}$ |
|---|---|---|
| Spatial Information Content Shuffled (P95) | 20 (7.87 %) | 39 (15.48 %) |
| Spatial Information Content Shuffled (P99) | 6 (2.36 %) | 8 (3.17 %) |
| Number of place cells (P95; *n* (% of total)) | 20 (7.87 %) | 39 (15.48 %) |
| Within-session Spatial Stability (*M* ±*SD*) | .26±.39 | .31±.32 |
| Head Direction Score Shuffled (P95) | 16 (6.30 %) | 24 (9.52 %) |
| Head Direction Score Shuffled (P99) | 1 (0.40 %) | 2 (0.79 %) |
| Number of head direction cells (P95; *n* (% of total)) | 16 (6.30 %)** | 24 (9.52 %)** |
| Speed Score Shuffled (P95) | 108 (4.25 %) | 35 (13.89 % ) |
| Speed Score Shuffled (P99) | 53 (2.13 %) | 8 (3.17 %) |
| Number of Speed Cells (P95; *n* (% of total)) | 108 (4.25 %)*** | 35 (13.89 % )*** |
| Border Score Shuffled (P95) | 28 (11.02 %) | 40 (16.87 %) |
| Border Score Shuffled (P95) | 15 (5.90 %) | 21 (8.33 %) |
| Number of Boundary cells (P95; *n* (% of total)) | 28 (11.02 %) | 40 (16.87 %) |
| Conjunctive Place and Boundary Cells (*n*, (% of total)) | 0 (0.00 %) | 1 (0.40 %) |
| Conjunctive Place and Head Direction Cells (n, (% of total)) | 4 (1.57 %) | 14 (5.56 %) |
| Conjunctive Place and Speed Cells (n, (% of total)) | 3 (1.18 %) | 2 (0.79 %) |
| Conjunctive Place, Head Direction and Speed Cells (n, (% of total)) | 1 (0.40 %) | 0 (0.00 %) |
| Conjunctive Place, Boundary and Head Direction Cells (n, (% of total)) | 1 (0.40 %) | 1 (0.40 %) |
| Conjunctive Place, Boundary and Speed Cells (n, (% of total)) | 0 (0.00 %) | 0 (0.00 %) |
| Cells in total (*N*) | 254 | 252 |

*Note.* % of the total refers to the proportion of cells compared to the total number of cells in the given condition.

*Note. M* = arithmetic mean, *SD* = standard deviation

* *p* < .050 ** *p* < .010, *** *p* < .001

### 3.3.3 Functional Properties of Place Cells

To explore potential differences in the mutual information carried out by the place cells of the two groups, a series of inferential tests were conducted based on the measures of the spatial information content, the spatial information rate, and the speed filtered average firing rate of the place cells. The following analysis only includes cells classified as place cells (*N* = 59) at an earlier stage of analysis. A Shapiro-Wilk test was performed to control for normal distributions of the samples. For relevant statistics, see Appendix B.

An independent samples t-test reported that there was not a significant difference in mean spatial information content (bits/spike) between the CamKIIα-*Tdg*$^{-/-}$ group (*n* = 38, *M* = 1.22, *SD* = .52) and the control group (*n* = 20, *M* = 1.10, *SD* = .54), *t*(56) = -.78, *p* = .439 (Figure 11A). A single outlier was identified using Tuckey's method and removed from the CamKIIα-*Tdg*$^{-/-}$ group, resulting in a normal distribution, confirmed by a Shapiro-Wilk test.

Further, I calculated the spatial information rate, a measure of how much information about the animal's location the cell transmits per second (Skaggs et al., 1992). The mean spatial information rate is a measure of the amount of information about the animal's location that is carried out by the activity of the cell as a function of time. This measure is closely related to the spatial information content. The spatial information rate was calculated using the following equation:

$$I = \int_x \lambda(\mathrm{x}) \log_2 \frac{\lambda(\mathrm{x})}{\lambda} p(x)\, dx$$

I = the information rate in bits per second for each cell
x = the animal's location in space
p(x) = the probability for the mouse being at x
$\lambda(x)$ = the mean firing rate when the mouse is at x
$\int_x \lambda(x)p(x)dx$ = the total mean firing rate of the cell

The mean spatial information rate (bits/sec) was higher and more variable for the control group (*n* = 20, *M* = .29, *SD* = .38) compared to the CamKIIα-*Tdg*$^{-/-}$ group (*n* = 39, *M* = .09, *SD* = .12), presented in Table 3. An independent samples t-test confirmed that the difference was significant between the genotypes *t*(2082) = 2.25, *p* = .035 (Figure 11B). For relevant statistics, see Table 3.

To examine the average firing rate of the cells, a speed filter of 2 cm/s was applied, excluding cell firing from when the mouse was standing still. A significant difference in the mean firing rate between the control group (*n* = 20, *M* = .26, *SD* = .34) and the CamKIIα-

*Tdg*$^{-/-}$ group (*n* = 39, *M* = .10, *SD* = .10) was detected using an independent samples t-test, *t*(20.66) = 2.09, *p* = .050. (Figure 11C). For relevant statistics, see Table 3.

In summary, the mean spatial information rate and the average firing rate were higher and more variable for the control group than for the CamKIIα-*Tdg*$^{-/-}$ group. This might be an indication that mutual information carried by the place cells of the CamKIIα-*Tdg*$^{-/-}$ is lower than expected from a normal population. The spatial information carried out per spike was similar for the two groups, which is incompatible with what is observed for the spatial information carried out per second for the two groups.

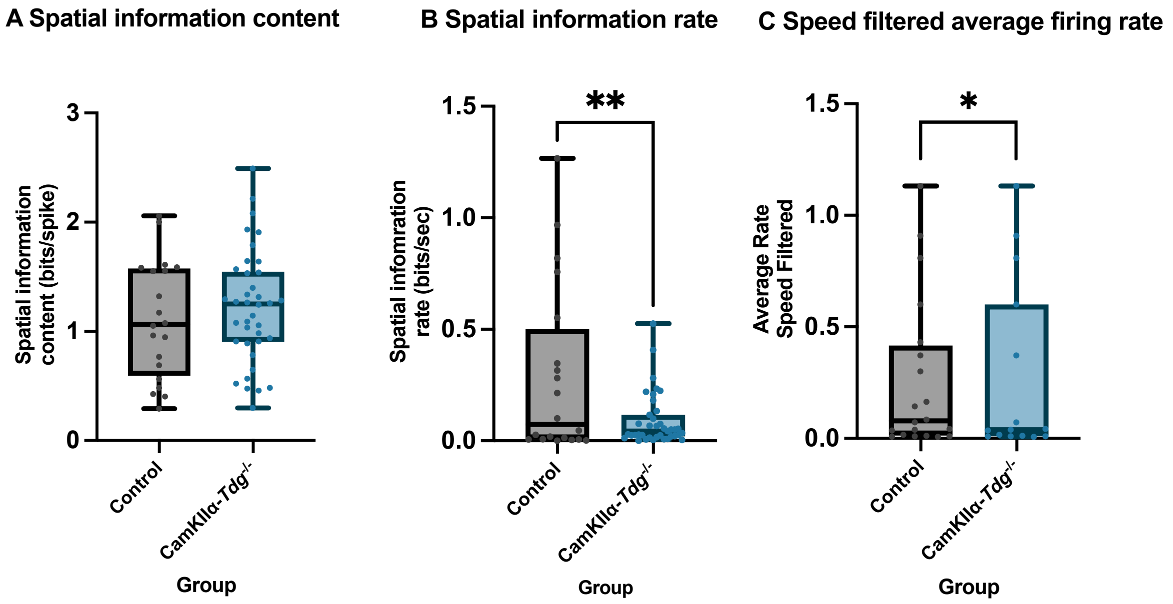

***Figure 11. Boxplot presenting different measures of the mutual information of place cells.*** **A|** Spatial information content (bits/spike) of the control group (grey) and the CamKIIα-*Tdg*$^{-/-}$ group (blue). **B|** Spatial information rate (bits/sec) of the control group (grey) and the CamKIIα-*Tdg*$^{-/-}$ group (blue). **C|** Speed filtered average firing rate of the control group (grey) and the CamKIIα-*Tdg*$^{-/-}$ group (blue). Single samples as represented by dots, in the color of their respective group. Results are presented as arithmetic mean and standard deviation. * = p < .05; ** = p < .01; *** = p < .001. The figure was made in GraphPad Prism.

#### 3.1.4.1 Specificity

To assess the specificity of place cells between the two genotype groups, I used the number of cells with multiple fields, the average size of the place fields, and the peak firing rate within the fields were analyzed as measurements. A Shapiro-Wilk test was performed to control for normal distributions of the samples.

The number of cells with more than one place field was counted. A Pearson Chi-Square test revealed that the proportional difference in cells with multiple place fields (*n* = 2, 12% of place cells in this condition) from the CamKIIα-*Tdg*$^{-/-}$ group (*M* = .05, *SD* = .22) and the proportion of cells with multiple place fields (*n* = 2, 10.0% of place cells in this condition) from the control group (*M* = .10, *SD* = .31) was not significant, *$X^2$(1, N = 59) = .50, p = .481.* For relevant statistics, see Appendix B.

An independent samples t-test revealed that there was no significant difference in the mean place field size (mm$^2$) between all place fields (*n* = 22) from cells in the control group (*M* = 106.53, *SD* = 182.56) and all place fields (*n* = 41) from cells the CamKIIα-*Tdg*$^{-/-}$ group (*M* = 110.53, *SD* = 150.06), *t*(36.47) = 1.10, *p* = .278 (Figure 12A). The control group cells displayed n = 13 fields categorized as small of size (< 150; M = 35.11, SD = 54.89, 4 medium (150 ≤ x ≤ 300; M = 201.60, SD = 35.87) sized fields, 3 large sized (300 ≤ x ≤ 450; M = 406.27, SD = 22.56) fields, and 4 very large fields (> 450; M = 525.05, SD = 26.52). The CamKIIα-*Tdg*$^{-/-}$ cells exhibited 26 small fields (M = 1154, SD = 40.76), 7 medium fields (M = 197.57, SD = 43.40), 7 large fields (M = 333.94, SD = 59.50), and 1 very large field (525 mm$^2$; Figure 13A). Intervals are defined based on the distribution of the two genotype place cell samples. A non-parametric test was used to investigate the differences in the rank total field size intervals, as deviations from normality were detected with a Shapiro-Wilk test. An independent-samples Kruskal-Wallis test confirmed that there were differences in field size distribution across the intervals, *H*(7) = 55.05, *p* < .001. An all-pairwise post hoc test was performed to compare the average rank field sizes. Only relevant comparisons are reported. Adjusted significance values are indicated in Figure 13B, for complete compartment statistics, see Appendix B. No significant differences were detected between the equivalent field size intervals for the control group and the CamKIIα-*Tdg*$^{-/-}$ group, *p* > .050. Statistically significant differences were observed between the group of small CamKIIα-*Tdg*$^{-/-}$ fields and the groups of medium, *p* < .001, large, *p* < .001 and very large, *p* = .012, CamKIIα-*Tdg*$^{-/-}$ fields. No significant differences were detected between the medium CamKIIα-*Tdg*$^{-/-}$ fields and the large CamKIIα-*Tdg*$^{-/-}$ and very large CamKIIα-*Tdg*$^{-/-}$ fields, *p* > .050. This was also true for the large CamKIIα-*Tdg*$^{-/-}$ and the very large CamKIIα-*Tdg*$^{-/-}$ field intervals, *p* > .050. Furthermore, the differences in rank field size between the interval group of small control fields and the medium control, *p* = .015, and large control fields, *p* < .001, were all significant. This was not true for the difference in rank field size for the medium control and very large control fields, *p* = .284. Differences between medium control fields and large and very large control fields and between large control fields and very large control fields were non-significant *p* > .050.

The place fields of the control group cells displayed a higher mean and variability in peak firing rates than the CamKIIα-*Tdg*$^{-/-}$ group cells. The difference in mean place field peak firing rates (Hz) was significant between the place cells (*n* = 22) of the control group (*M* = 3.03, *SD* = 4.06) and the place cells (*n* = 41) of the CamKIIα-*Tdg*$^{-/-}$ group (*M* = .98, *SD* = 1.56), estimated with an independent samples t-test, *t*(24.36) = 2.29, *p* = .031 (Figure 12B). For relevant statistics, see Appendix B.

In summary, the CamKIIα-*Tdg*$^{-/-}$ group of place cells displayed a lower mean and variability in peak firing rates than the control group. This might indicate impaired spatial specificity of the CamKIIα-*Tdg*$^{-/-}$ mice, given the correct location of tetrodes in all mice. The place fields from both groups were mainly concentrated within the range of $0 \leq x \leq 150$, categorized as small. The number of fields gradually decreased in notion with the increasing size, this was similar for both groups.

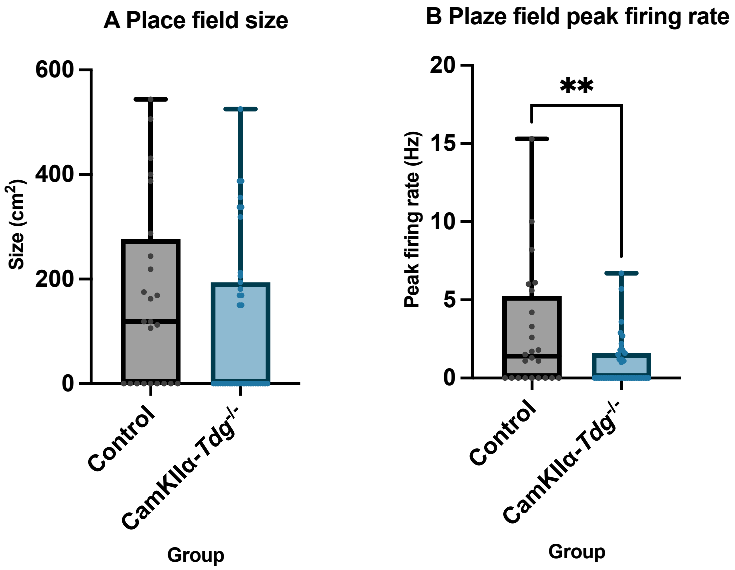

***Figure 12. Boxplot presenting the specificity of the spatial representations of place cells.*** **A|** place field size of the control group (grey) and the CamKIIα-*Tdg*$^{-/-}$ group (blue). **B|** Place field peak firing rate of the control group (grey) and the CamKIIα-*Tdg*$^{-/-}$ group (blue). Single samples as represented by dots, in the color of their respective group. Results are presented as arithmetic mean and standard deviation. * = *p* < .05; ** = *p* < .01; *** = *p* < .001. The figure was made in GraphPad Prism.

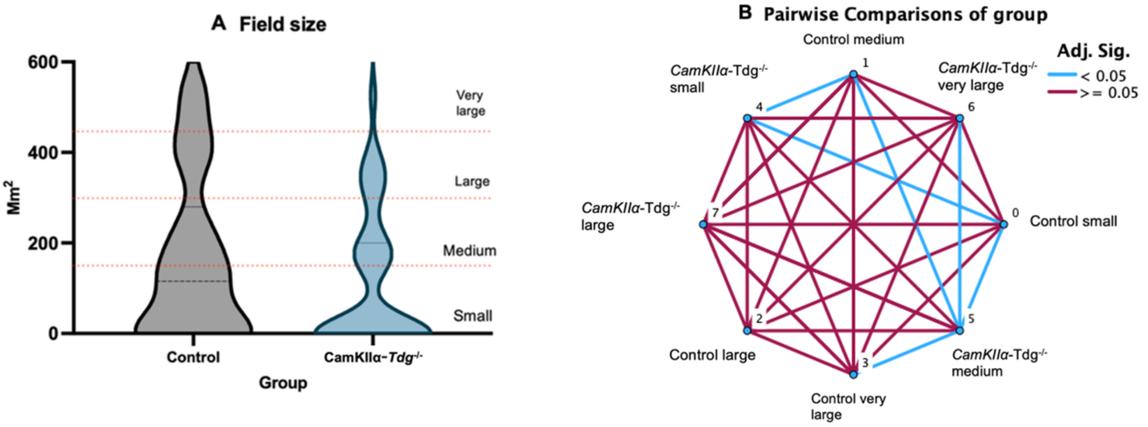

***Figure 13. Violin plot of place field size sample distributions and pairwise field size interval comparison.*** **A|** Violin plot illustrating the distribution of place fields as a function of four 150 mm$^2$ intervals (small, medium, large, very large) between the place field control group (grey) and the place field CamKIIα-*Tdg*$^{-/-}$ group (blue). Red dotted lines indicate the distinctions between intervals. Black dotted lines indicate median and quartiles in each group. The figure was made in GraphPad Prism. **B|** Line chart showing pairwise comparison of average rank place field size

(mm^2) from each group categorized in 150 mm^2 (0-600) intervals from control group and the CamKIIα-$Tdg^{-/-}$ group. Each node shows the sample average rank of the interval group. Alpha levels is presented in Adj. Sig., adjusted by a Bonferroni test (blue lines indicate $p > .050$, red lines indicate $p > .050$; se Appendix B for test statistics). The figure was made in SPSS. Small = < 150, medium = 150 ≤ x ≤ 300, large = 300 ≤ x ≤ 450, very large = > 450.

**Table 3**

*General electrophysiological properties of place cells in control versus Tdg KO mice.*

| | Control | CamKIIa-$Tdg^{-/-}$ | Central tendency comparison. Test statistics. |
|---|---|---|---|
| Within-session stability (*r; M* ± *SD*) | .32 ± .33 (*n* = 20) | .34 ± .29 (*n* = 39) | *U* = 401.00 |
| Spatial information content (bits/spike; *M* ± *SD*) | 1.10 ± .54 (*n* = 20) | 1.22 ± .52 (*n* = 38) | *t* = -.78 |
| Spatial information rate (bits/sec; *M* ± *SD*) | 0.29 ± 0.38 (*n* = 20) | 0.09 ± 0.12 (*n* = 39) | *t* = 2.25 ** |
| Average firing rate | .26 ± .34 (*n* = 20) | .10 ± .10 (*n* = 39) | *t* = 2.09* |
| Cells in total (*N*) | 20 | 39 | |
| Place cells with multiple fields | *.10 ± .31* (n = *2)* | *.05 ± .22* (n = *2)* | $X^{2\,=}$ *.50* |
| Place field size (mm2) | 106.53 ± 182.56 (*n* = 22) | 110.53 ± 150.06 (*n* = 41) | *t* = 1.10 |
| Place field peak firing rate (Hz) | 3.03 ± 4.06 (*n* = 22) | .98 ± 1.56 (*n* = 41) | *t* = 2.29** |
| Place fields in total | 22 | 41 | |

*Note.* *M* = arithmetic mean, *SD* = standard deviation, *r* = Pearson correlation coefficient, *U* = Mann-Whitney U value, *t* = t-value, *X*^2 = Chi square value
* $p < .050$ ** $p < .010$, *** $p < .001$

### 3.1.4.2 Remapping

To investigate the global remapping capabilities of the place cells between the genotypes, a correlation analysis of rate maps between the two boxes in the two global remapping conditions (A1 and B1 (A1B1), and B2 and A2 (B2A2); Figure 7A) was conducted. In order to calculate the correlations between the rate maps, each map was binned to 2 cm bins. The summed value of the bins for each value of the y-axis was subsequently correlated. Subsequently, an average total Pearson correlation coefficient for the whole map was calculated by the y-axis iterations. Then, I calculated descriptive and inferential statistics from the computed correlation coefficients. Assuming that the cells display normal global remapping, correlation coefficients close to 0 are expected. The mice from the control group took part in 21 recording sessions with remapping and stability-testing, collectively. The mice from the CamKIIα-$Tdg^{-/-}$ group took part in 20 recording sessions with remapping and stability-testing, collectively. A total of 27 place cells were analyzed for the A1B1 condition, of these 37,04% (*n* = 10) belonged to the control group and 62,96% (*n* = 17) belonged to the CamKIIα-*Tdg*$^{-/-}$ group. A total of 24 place cells were analyzed for the B2A2 condition, of these 41,67% (*n* = 10) belonged to the control group and 58,33% (*n* = 14) belonged to the CamKIIα-*Tdg*$^{-/-}$ group. An example of a single-cell remapping from both genotypes is presented in Figure 16.

In the A1 to B1 condition place cells from both the control group, *r* = -.10, and the CamKIIα-*Tdg*$^{-/-}$ group, *r* = .06, showed a notably weak negative correlation between the A1 and the B1 condition. An independent samples t-test was performed to evaluate the difference in rate map correlation coefficient means (A1B1; Figure 7A) between the control group (*n* = 10, *M* = -.10, *SD* = .17) and the CamKIIα-*Tdg*$^{-/-}$ group (*n* = 17, *M* = .06, *SD* = .29). The results indicated that there was not a significant difference between the genotypes, *t*(26) = -1.65, *p* = .110 (Figure 14A). A Shapiro-Wilk test showed a small deviation from normal distribution in the control group for the A1B1 condition, but this was not adequate to warrant a non-parametric test. For relevant statistics, see Appendix B.

In the B2 to A2 condition, like the A1 to B1 condition both the control group, *r* = -.16, and the CamKIIα-*Tdg*$^{-/-}$ group, *r* = .15, showed a weak correlation between the A1 and the B1 condition. An independent samples t-test was performed to evaluate difference in rate map correlation coefficient means (B2A2; Figure 7A) between the control group (*n* = 10, *M* = -.16, *SD* = .15) and the CamKIIα-*Tdg*$^{-/-}$ group (*n* = 14, *M* = .15, *SD* = .29). The results indicated that there was a significant difference between the genotypes, *t*(22) = -3.11*, p* = .005 (Figure 14B). A Shapiro-Wilk test showed a normal distribution for both samples in the B2A2 condition. For relevant statistics, see Appendix B.

In summary, both place cell groups from the control mice and CamKIIα-*Tdg*$^{-/-}$ mice showed normal global remapping in both remapping conditions. There were no statistically significant differences in performance between the genotype groups in the A1B1 condition, but the CamKIIα-*Tdg*$^{-/-}$ cells displayed predominantly higher mean stability in the B2A2 condition than the control cells. However, the correlation was weak.

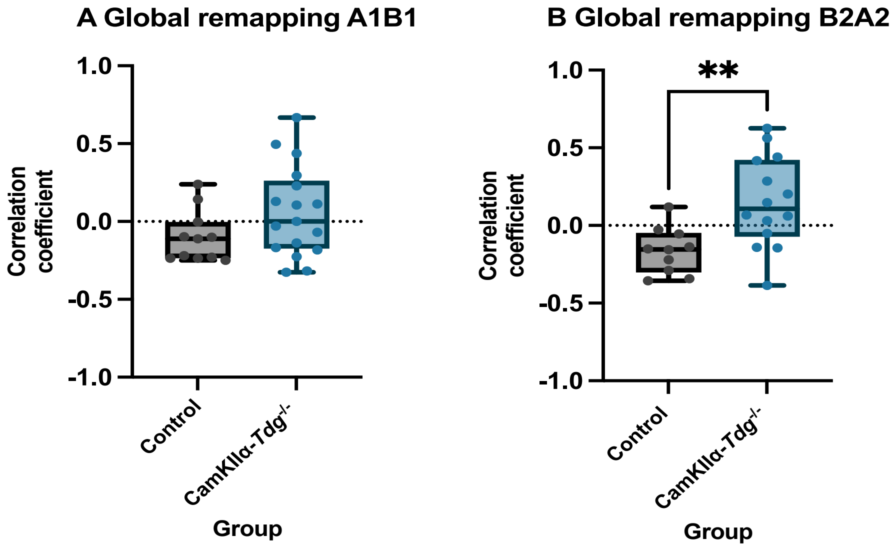

***Figure 14. Boxplot presenting results of place cells from two global remapping conditions.*** **A|** Global remapping in the A1B1 condition of the control group (grey) and the CamKIIα-*Tdg*$^{-/-}$ group (blue). **B|** Global remapping in the B2A2 condition of the control group (grey) and the CamKIIα-*Tdg*$^{-/-}$ group (blue). Single samples as represented by dots, in the color of their respective group. Results are presented as arithmetic mean and standard deviation. * = $p < .05$; ** = $p < .01$; *** = $p < .001$. The figure was made in GraphPad Prism.

### 3.1.4.3 Short-Term Stability

To investigate the short-term stability of the place cell spatial representations, a similar analysis of rate maps was performed as for the global remapping condition. In total, 27 cells were included in the short-term stability testing, in which 48,14% (*n* = 13) belonged to the control group and 51,85% (*n* = 14) belonged to the CamKIIα-*Tdg*$^{-/-}$ group. The correlation coefficients between the A1 and A2 rate maps (Figure 7A) were compared to investigate the short-term stability performance of the two genotypes. Strong correlations between the maps indicate normal short-term stability. An example of a single-cell short-term stability from both genotypes is presented in Figure 16.

A moderate positive mean correlation between the A1 and A2 (A1A2; Figure 7A) rate maps was detected for the control group cells *r* = .39. The positive correlation between A1 and A2 rate maps was low for the CamKIIα-*Tdg*$^{-/-}$ group, *r* = .07. An independent samples t-test was performed to evaluate difference in rate map correlation coefficient between the control group (*n* = 13, *M* = .39, *SD* = .42) and the CamKIIα-*Tdg*$^{-/-}$ group (*n* = 14, *M* = .07, *SD* = .27). The difference was significant between the genotypes, *t*(31) = 2.68*, p* = .012 (Figure 15A). A Shapiro-Wilk test controlled for normally distributed samples. For relevant statistics, see Appendix B.

In summary, the control group cells displayed moderate short-term stability, whereas the cells of the CamKIIα-*Tdg*$^{-/-}$ mice displayed weak stability. A significant difference between the groups in place cell short-term stability was detected. The control group display slightly lower short-term stability scores than what is expected from normal place cells.

### 3.1.4.4 Long-Term Stability

To investigate the long-term stability of the place cell spatial representations, a similar analysis of rate map correlation coefficients was performed as for the short-term stability and the global remapping condition. In total, 30 cells were included in the long-term stability condition, of these, 43,33% (*n* = 13) were from the control group and 56,67% (*n* = 17) were from the CamKIIα-*Tdg*$^{-/-}$ group. The correlation coefficients between the A0 and A1 conditions (A0A1; Figure 7B) was compared. If the cells display normal long-term stability, we can expect to see strong correlations between the rate maps. An example of a single-cell long-term stability from both genotypes is presented in Figure 16.

A moderate positive correlation between the A0 and A1 rate maps was detected for the control group, *r* = .33, and a weak positive correlation for the CamKIIα-*Tdg*$^{-/-}$ group, *r* = .04. An independent samples t-test was performed to evaluate difference in rate map correlation coefficient (A0A1; Figure 7B) between the control group (*n* = 10, *M* = .33, *SD* = .44) and the CamKIIα-*Tdg*$^{-/-}$ group (*n* = 14, *M* = .04, *SD* = .23). The results indicated a significant difference between the genotypes, in which the CamKIIα-*Tdg*$^{-/-}$ displayed lower stability scores and less variability, *t*(22) = 2.20*,* *p* = .039 (Figure 15B). Outliers was detected with a Tukey's test and removed. A Shapiro-Wilk test showed normal distribution in both groups. For relevant statistics, see Appendix B.

In summary, cells from both genotypes displayed abnormal long-term stability capabilities. No differences below alpha levels (.05) were detected, but the CamKIIα-*Tdg*$^{-/-}$ cells had lower stability scores than the control group cells. Of note, the spatial stability of place cells in my control group was much weaker than what is known for wild-type place cells.

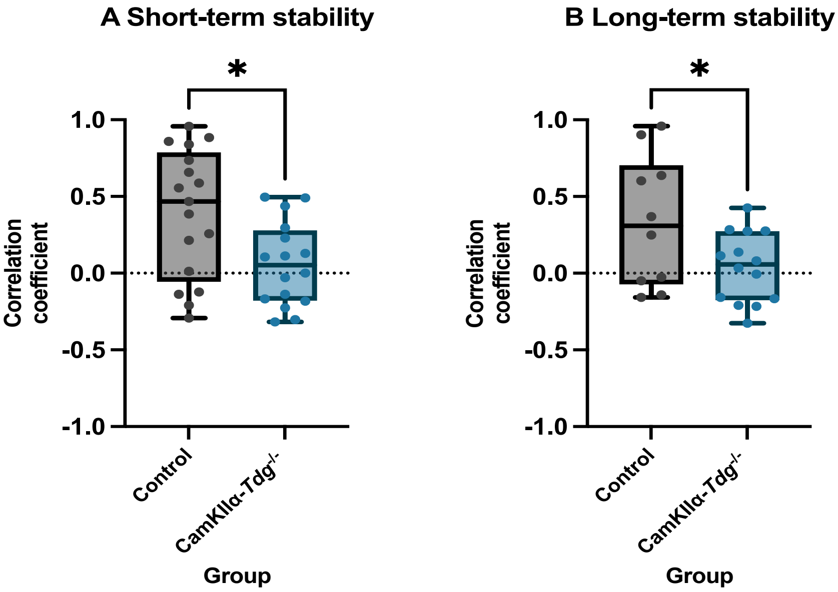

***Figure 15. Boxplot presenting results of place cells from two stability conditions.*** **A|** short-term stability of the control group (grey) and the CamKIIα-*Tdg*$^{-/-}$ group (blue). **B|** Long-term stability of the control group (grey) and the CamKIIα-*Tdg*$^{-/-}$ group (blue). Single samples as represented by dots, in the color of their respective group. Results are presented as arithmetic mean and standard deviation. * = *p* < .05; ** = *p* < .01; *** = *p* < .001. The figure was made in GraphPad Prism.

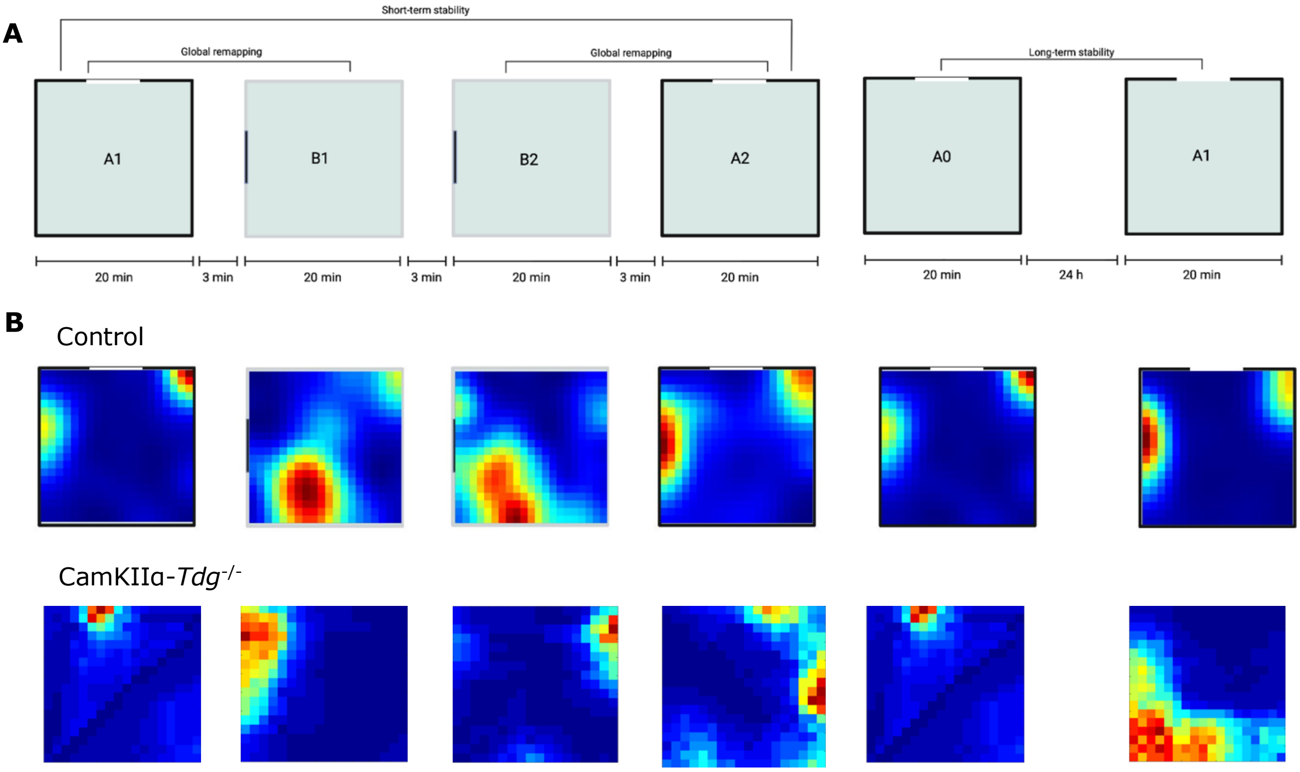

***Figure 16. Rate maps from CamKIIα-Tdg$^{-/-}$ cells control cells from each trial in the remapping and stability paradigm.*** **A|** Global remapping and stability experimental design. The figure was made in BioRender. **B|** Smoothed rate maps from an example place cell from each group in corresponding recoding arena presented in A. Upper: Control cell. Lower: CamKIIα-*Tdg*$^{-/-}$ cell. Figure was made in MATLAB.

## 4 Discussion

The findings of this study comprise electrophysiological data aiming to elucidate whether TDG impacts the proportion of spatial cells and the specific functional properties of place cells in the CA1 of the hippocampus. The findings indicate that TDG does impact some features of the functional plasticity of place cells in the CA1. Furthermore, one of the main findings suggests that TDG could have a role in forming and maintaining the stability of spatial representation in the place cells.

Knowledge about the functional correlates of TDG depletion in spatial cells can provide further insight into the epigenetic mechanisms governing functional plasticity in the spatial navigation system. Additionally, assessment of the molecular correlates of CA1 excitatory cell TDG depletion can provide a more comprehensive understanding of spatial cognition in general. A notable limitation of this study is the small and heterogenous sample size. Hence, the accumulation of more data might significantly change the results. The following section will first deliberate on the results obtained from electrophysiological data, aiming to assess the functional properties of TDG-depleted spatial cells. Secondly, results regarding place cell properties will be discussed in the context of TDG regulation of gene expression before providing an assessment of the main shortcomings in this research project and consequential considerations for future perspectives will be presented.

### 4.1 Mouse Model

The mouse model used in the current study had hippocampal-specific conditional knockout of *Tdg*. This transgenic mouse model was developed using a time and tissue-specific promotor, CamKIIα, which mainly control gene expression in excitatory neurons (Wang et al., 2013). Primarily, CamKIIα targets the pyramidal layer of the CA1 area. Introduction of Cre allows excision of genes flanked by LoxP sites. Hence the TDG enzyme will mainly be depleted in the anatomical area of interest, containing the spatial cells which are foremost located in the pyramidal layer of the CA1. Furthermore, the knockout is restricted to excitatory neurons, being the regional spatial cells. Given exact knockout of *Tdg*, precise anatomical and morphological experimental regulation of gene expression in the mouse brain is highly beneficial when assessing spatial memory, and the following results are thus reinforced. However, the indispensability of the CamKIIα promoter's specificity in regulating Cre expression is central in achieving a precise conditional *Tdg* knockout. Leakage in Cre expression can occur, which could lead to extensive recombination. An inadvertent germline deletion of floxed genes in Cre-mouse lines could lead to heritable transmission of the knockout allele across subsequent generations, resulting in a persistent absence of the targeted genes in the offspring (Hardeland et al., 2001). As the promotor is mainly active in CA1, other hippocampal structures only undergo partial *Tdg* knockout. The partial depletion of TDG could affect hippocampal spatial representation, by, for example altering navigation-specific functions grounded in the hippocampal circuitry.

Conversely, as the hippocampus holds strong empirical correlates with spatial memory, and the CA1 place cells are extensively studied and highly accessible, assessment of these exact cells would provide grounding observations for future investigation. Specific alternation of gene expression allows for the investigation of the effects of structure- and cell-specific methylation and demethylation patterns on spatial memory, while at the same time not altering behavior and cell functionality associated with other anatomical structures, that otherwise could lead to confounding effects. The genotyping of the mice used in this study was performed twice, both before and after *in vivo* experimentation, providing dual validation of the gen pattern of the mice used for neural recording.

## 4.2 Cell Physiology

Cells from the CA1 of 4 mice were clustered and included in the analysis. The low number of mice used in recording may limit the current findings. The low sample size increases the chance of insufficient statistical power, inflated false discovery rate and effect size estimation, and might reduce the reproducibility of the results. Too small a sample may prevent the findings from being inferred. For example, a small behavioral difference or abnormal genetic expression in one of the 4 experimental subjects could have a greater effect on the outcome variable of the respective place cells, compared to the case of an appropriate sample size. Finally, when the total number of cells recorded from each of the animals varies, the data from certain animals may be weighted more heavily than the data from others.

A total number of 506 recorded cells were clustered. Some possible issues with the process of clustering are present. If a given cell cluster contains spikes originating from a different cell, the validity of the cells' features is compromised. Moreover, if a cluster lacks spikes from the targeted cell, the validity is also reduced. It is also probable that some place cells were overlooked due to infrequent firing in one environment compared to another, leading to a small number of data points in the clustering feature space of the A1 recording area. This could be a result of spatial cell remapping and becomes an issue when initially clustering and determining spatial tuning of cells recorded in a single environment. Alme et al. (2014) found that CA3 place cells are not necessarily active in multiple environments, which could be the case for the observations of CA1 place cells. This underpins a limitation of the respective recording design. To address these issues concerning cell categorization, a possible solution could be the involvement of two or more independent experimenters in data clustering, followed by examining the internal consistency of the clustered data points. An impaired channel in one of the drives implanted in a control mouse proposed a notable challenge for the manual clustering process.

Furthermore, PCA was used to cluster distributions in the feature space that were particularly challenging. As PCA is known to be sensitive to outliers, PCA may not provide accurate results, and the clusters based on principal components may be easily affected by noise. To handle these issues, one could use more robust computational techniques to eliminate outliers or noise. Given that the cells are correctly clustered, the size of the cell sample are notably low compared to what is typically seen in the neural recording literature and what might have been appropriate according to a power analysis. In a low cell sample size, individual differences and outliers will have prominent effects on the observed outcomes.

### 4.2.1 Cell Classification and Proportion

The cells were classified into 10 groups, including place cells, HD cells, speed cells, boundary cells, and various conjunctive cells (Table 2). In the populations of recorded place cells, HD cells and boundary cells were not distributed differently across the CamKIIα-*Tdg*$^{-/-}$ mice and the control mice. The distribution of identified speed cells on the other hand was prominently higher in the control mice, while the fraction of place cells was higher in the CamKIIα-*Tdg*$^{-/-}$ mice. To my knowledge, the relationship between spatial cell distribution and TDG has not been examined previously.

The classification of place cells was performed using the mutual information equation developed in accordance with information theory. The calculated information outcome will be influenced by several parameters used to preprocess the data, such as the defined bin size and data smoothing, which can affect the detection of place cells. Selecting an inappropriate bin size or smoothing parameter can lead to false positives or false negatives. The method of calculating mutual information to detect place cells will also be sensitive to the data point sample size in each cluster. In the case of this study, this limitation is controlled for by setting the threshold for number of spikes in a cluster to 100 spikes, in accordance with previous research (Kunath et al., 2021). This could lead to neglection of some cells, particularly those that display low firing rates in the A1 environment (Figure 7A), but at the same time controlling for the sensitivity of the mutual information classification method. The fact that the average within-session stability of the total amount of cells was moderate and that there were no differences between the genotypes in the number of cells displaying low or moderate correlation across the session halves (Figure 10B), points to clustering errors. Moreover, not all place cells displayed place fields, but did still hold information content above threshold (P95; Figure 10A). The quantity of recorded cells in the control group categorized as place cells but lacking important place cell characteristics, such as strong within-session stability and place fields, might imply that the filtering parameters were inadequate in their level of stringency. Including spatial within-session stability as a filter could potentially resolve this issue.

It is possible that the population of speed cells is different between the two genotypes, and there is in fact a smaller proportion of speed-selective cells present in the CA1 of TDG-depleted mice. The low sample size disputes this result. The observed speed cell distribution as an effect of genotype might also be due to disruptions in the amount of speed information being encoded by the CamKIIα-*Tdg*-/- cells. In that case, the definite quantity of pyramidal neurons with speed cell properties could be the same for both genotypes, but the spatial information carried out by the cells would be impeded, and not succeed the 95th percentile cut-off for being classified as speed cells. This observation could also point to the sparse firing of speed cells in TDG-depleted mice, thus resulting in low detected numbers of these cells in the conditional knockout mice compared to control mice.

The low number of conjunctive cells observed in both genotypes is consistent with what is typically observed in normal spatial cells. Spatial cells have been found to predominantly display invariant spatial tuning (Muller et al., 1994; Burgess et al., 2005). This is for example, true for the speed cells, found to mainly be invariant to both the HD and the location of the animal (Burgess et al., 2005).

The classification and determined distribution of spatial cells in the CA1 of the two district genotypic groups might be influenced by the small sample of mice included in this study. The trajectory and placement of tetrodes in the brain of the mice will have considerable effects on the outcome. The significantly large proportion of speed cells in the control group compared to the CamKIIα-*Tdg*$^{-/-}$ group might give an indication that the tetrode of one or both control mice was misplaced and located externally of the structure of interest. Speed cells are present in both the mEC and the hippocampus (Ye et al., 2018), making it difficult to determine the location of the recording without a definite tetrode position analysis. An examination of the scanned brain slices from each mouse would provide the opportunity to control for this possible determinant error. Furthermore, pyramidal cells in the ventral parts of the CA1 are more likely to be active compared to more dorsal parts of the CA1 (Malik et al., 2016; Milor et al., 2016). Moreover, the deeper neurons are more likely to display place cell characteristics (Mizuseki et al., 2011). Differentiated placement of tetrodes across the genotypes could also account for the observed difference in place cell proportion.

### 4.2.2 Functional Properties of Place Cells

To my knowledge, this is the first time the spatial representations of CA1 place cells have been investigated in a mouse model with hippocampus-restricted *Tdg* knockout. Similar numbers of place cells were recorded in control and CamKIIα-*Tdg*$^{-/-}$ CA1. In the place cell populations of the two groups, there was found a predominant difference in the spatial information rate and filtered average firing rate, in which the CamKIIα-*Tdg*$^{-/-}$ cells carried out less information about spatial location than the control cells (Figure 11B-C). This result suggests that there is a difference in the mutual information carried by the place cells across the genotypes. The outcome of this analysis could also be inferred by the low within-session stability observed in the place cells. However, if this is the case, equal effects would be observed for the control group as well as for the CamKIIα-*Tdg*$^{-/-}$, as the within-session stability was invariant between the groups.

However, no significant difference was observed in terms of the spatial information content. The two cell populations held spatial representations for approximately the same amount of information about the animal's position in terms of information content (Figure 11A). As the information content of the cell is closely related to information rate of the cell, and these are expected to correlate positively in normal place cells (Souza et al., 2018), the results are overall inconsistent. These results might be affected by potential errors in cluster cutting and effects caused by the sample size.

Disregarding evident methodological shortcomings, the observations of place cell spatial information does point to the impact of TDG on CA1 place cell spatial functionality, in terms of filtered average firing rate and information rate.

### 4.2.3 Specificity

A series of analyses were conducted to examine the relationship between TDG and place cell spatial specificity. The spatial specificity was invariable between the groups in the quantity of cells with multiple place fields and the mean size of the place fields, whereas the CamKIIα-*Tdg*$^{-/-}$ cells had a lower place field peak firing rate than the control cells.

The fraction of place cells with multiple place fields as a function of genotype, implies that TDG does not impact the specificity of place cells in terms of cells developing more or less place fields than expected from *Tdg*-intact cells. Furthermore, as the integration of information in the CA1 seems intact, this might give an indication that the scale of the hippocampal spatial representation is unaffected by the TDG depletion. Previously, Park et al. (2011) and Fenton et al. (2008) observed that expansion of the recording area was related to increasement in the number of fields. The results of the current study might have been different in a larger and more representative environment. Assessment of place cell ability to increase place field number in relation to space expansion could be of interest for future research.

Furthermore, no apparent differences in place field size as an effect of TDG depletion was detected (Figure 12A). Consistent with the findings concerning the relation between genotype and the number of cells with multiple fields, discussed in the preceding paragraph, this finding strengthens the notion of an intact spatial representational scale in the TDG-depleted CA1.

The observed invariance in place field size implies preserved structural connections between the CA1 and adjacent areas. Given that there is no difference in place field size between the two genotypes, this might imply that the schaffer collateral pathway from the CA3 cells to the CA1 is not impaired by the TDG depletion. In the case of inhibition of the CA3 vesicle release, previous findings have indicated that this disruption leads to increased place field size in the CA1 (Davoudi & Foster, 2019). Whereas, in accordance with Hussaini et al. (2011), this specific result will not exclude the possibility that synapses between the CA1, and the EC are disrupted. Hippocampal place cells are thought to integrate input from the mEC dorsoventral grid scale, but previous findings indicate that CA1 place cells are more reliant on their local circuitry than input from the EC grid cells (Hussaini et al., 2011). The invariance in place field size for the two genotypes, will thus not have a disturbing effect on the CA1 input connections from the mEC. The amount of optic flow and number of cues presented to rodents has been found to correlate with the place field size. This pattern is similar to the correlation between the size of the recording area and the number of place fields, as discussed in the previous paragraph. The outcome of the current analysis might have been different in a more stimulating and representative environment.

Differences in tetrode location among the small subject sample could account for the invariances in place field size and single cell field number. As the place cell representational scale increases along the longitudinal hippocampal axis hippocampus (Kjelstrup et al., 2008), the observed results could be due to a difference in recording location on the longitudinal axis. Thus, recording of cells from different locations on the hippocampal representational scale could account for invalid results.

Furthermore, there was no observable difference in the frequency of small ($< 150$ mm$^2$), medium ($150 \leq x \leq 300$), large ($300 \leq x \leq 450$), and very large ($> 450$) place fields across the CamKIIα-*Tdg*$^{-/-}$ and the control cells (Figure 13). However, both the CamKIIα-*Tdg*$^{-/-}$ and the control place cells had a larger fraction of small place fields, compared to the other size intervals (Figure 13B). Features of the recording enclosure could account for this tendency to display small place fields, as cumulative stimulation in a given environment correlates with the observed place fields size (Lu & Bilkey, 2010; Sharif et al., 2021). The observed quantity of small fields compared to larger fields might also be influenced by the modest sample size and clustering errors, as many of the fields appear closer to 0 mm$^2$. The modest within-session stability supports this assumption. To explore this issue, it could be feasible to review the correlation between low firing rates and small fields.

The peak place field firing rate was observed to be lower and more variable for the TDG-depleted cells than the control cells (Figure 12B). The place field peak firing rate is not necessarily related to the field size (Hussaini et al., 2011; Davoudi & Foster, 2019; Lu & Bilkey, 2010), thus, the possibility of one being affected by experimentally alternating demethylation enzymes and not the others are likely. This promotes the possibility that TDG might be related to certain spatial representational properties of place cells.

In summary, no effects of genotype were observed for the information content carried out by the place cells, the number of cells with multiple place fields, or the average place field size displayed by the cells. However, disregarding the small sample size and possible clustering issues, certain general functional properties (spatial information rate, average firing rate, and place field peak firing rate) of cells from the CamKIIα-*Tdg*$^{-/-}$ group display deviations from normality.

### 4.2.4 Global Remapping

An investigation of the effect of TDG on the global remapping capacities of CA1 place cells was performed with distinct results. The global remapping capabilities of the two current place cell populations were significantly invariant, and the TDG-depleted mice remapped as normal between the two environments (Figure 14).

The control cells performed as expected from normal place cells (Latuske et al., 2018), implying that the remapping condition itself is reliable. This will depend on potential clustering issues. If the cell in the second condition is clustered differently than the original cell from the first condition, or if it is a different cell altogether, this would lead to a false global remapping result, as there would be low to no correlation between them. Given that the clustering is correct, and the test is reliable, the TDG-depleted cells maintain intact global remapping compared to the control cells. This result is consistent with what we expect in terms of plasticity in place cells deficient in TDG, as its main effect would be related to gene expression for protein synthesis in long-term plasticity alternation. This will be further elaborated on in a later section. As the respective remapping paradigm is performed in a time frame associated with short-term plasticity, the results could have been different for a long-term conditioned remapping paradigm aimed at assessing synaptic strengthening by protein synthesis.

The remapping capabilities in the hippocampal cells can also be influenced by activity in the mEC, according to the finding of Kanter et al. (2017), who observed that activation of mEC cells correlated with remapping in CA1. The mEC is suggested to function as a noise reducer and place cell synchronizer (Rennó-Costa & Tort, 2017; Fyhn et al., 2007). The results of my project showed that TDG-depleted hippocampal cells holds intact global remapping. Hence the function of the mEC could be preserved. Thus, potentially implying that TDG does not have a functional effect on the local circuitry of the mEC or in one of the mEC input pathways to the hippocampus. On the other hand, it is of importance to note that the result does not exclude the possibility of a significant effect between CA1-specific TDG depletion and the mEC activity and hippocampal connections. In more recent studies hippocampal place cell remapping has been observed to be intact in the instance of experimental mEC impairment (Schleiger et al., 2018; Jun et al., 2020). Given this conclusion, alternations in the signals from the mEC input could account for the observed effects in the *Tdg* knockout cells of the CA1 as well. As the mEC might act as a remapping modulator (Rennó-Costa & Tort, 2017; Fyhn et al., 2007) rather than a direct executive structure, the two proposals do not exclude each other. The role of the mEC in TDG-depleted place cell performance is thus elusive.

Intact remapping capabilities might be related to the conserved ability of the cells to carry spatial information content and spatial specificity. Intact remapping capabilities indicate that the population of cells representing the different spaces are unique. If a subset of place cells does not remap when exposed to a novel environment, it is possible that certain aspects of the given memory template are encoded into the incorrect memory substrate. This could lead to the interference of memory fragments. From the perspective of cognitive map theory, this could be the mistakenly encoding of memory coordinates onto the wrong map, leading to the disorganization of the spatial content on the map. The TDG-depleted place cells seem to withhold the ability to map novel environments. However, as will be discussed in a later section, the spatial representation of the given environment does not remain stable over time.

The observation of invariance between genotypes in remapping capabilities might be an effect of heterogeneous and low sample size, as discussed for previously presented variables. It is a possibility that the findings could be attributed to an inaccuracy within the experimental setup. However, if there indeed was a determinant issue with the experimental setup, it should have affected the results observed in both groups since they were subjected to identical experimental conditions and analyses.

Furthermore, it should be noted that there was an irregular level of familiarity between the two recording enclosures used in this study. The mice were recorded more times in area A, which was the enclosure used in most of the experiments, whereas area B was only used for remapping conditions. This discrepancy in recording time corresponds to the notion that the cells had the most opportunities to consolidate their neural representations of the space in arena A, which may have resulted in stronger spatial associative learning.

### 4.2.5 Stability

Results from the two stability conditions showed that the CamKIIα-*Tdg*$^{-/-}$ place cells have significantly lower mean positive correlation between exposure to equivalent environments with 50 min and 24 h inter-trial intervals, compared to the control cells (Figure 15). The mean correlation was weak for the TDG-depleted cells and moderate for the control cells in both conditions. Despite the observation that CA1 place cells tend to be less stable than place cells of other hippocampal regions (Dong et al., 2021), the control cell stability deviates substantially from what is expected from normal place cells and is largely inconsistent with previous observations (Thompson & Best, 1990; Kinsky et al., 2018). This observation might imply weak test reliability, and could thus point to methodological errors, such as a small sample size or inaccuracies in the performance of the experimental procedure. Issues with clustering and spike sorting will potentially influence the results considerably. So will a potentially insufficient sample size, both in terms of mouse subjects in each group and cell number. The samples did have a slight deviation from normal distribution, but a non-parametric test was not implemented, this could have had a modulatory effect on the results.

In the investigation of place cell stability, the CamKIIα-*Tdg*$^{-/-}$ cells displayed weaker short-term and long-term stability compared to the control cells. During the experiment, it was observed that CamKIIα-*Tdg*$^{-/-}$ place cells consistently remapped to the novel environment similarly to control cells, suggesting their ability to generate new maps was intact. However, in the familiar environment, a higher proportion of CamKIIα-*Tdg*$^{-/-}$ place cells continued to remap across different trials separated by either 50 min or 24 h, indicating impaired short- and long-term spatial stability. Of note, within each recording session, the place fields were found to be unstable and lacking coherence. This implies that the place cells did not reliably maintain their spatial maps once they were selected and might justify the observed abnormality in control cell performance.

The CamKIIα-*Tdg*$^{-/-}$ cells remap as expected for wild-type cells between changing environments but do not display normal short- and long-term stability across familiar environments. It is plausible to assume that the observed discrepancy between the global remapping and stability is due to the fact that assessment of stability was performed using an environment frequently presented to the mice (box A). This could mean that the cells display more stability in their firing patterns because they are in a profoundly familiar environment, where the animal has stronger associations to specific environmental indicators, compared to the less frequently presented environment (box B). Thus, the stability between the more familiar environment (box A) may not necessarily translate to other environments, leading to spatial remapping when the mice are placed in a more novel environment (box B). Overall, the observation may suggest that the observed instability may be specific to the familiar environment in which the mice were tested and may not be generalizable to other environments. The reliability of the implemented short-term stability test could also be assessed by comparing stability as a function of genotype between the B1 and B2 environments (Figure 7A).

Normal place cell stability is found to vary substantially across the radial axis of CA1 (Danielson et al., 2016). Thus, the location of the recording tetrode in the CA1 might influence results. More superficially situated CA1 neurons has previously been reported to encode the stable features, whereas deeper neurons encode the changing features of the environment. The tetrodes being located more superficially in CA1 in one or two of the control mice compared to the CamKIIα-*Tdg*$^{-/-}$ mice, could account for the observed difference in correlations between familiar boxes in the two genotypes. Given a significant difference in placement of the tetrodes along the radial axis of the control and CamKIIα-*Tdg*$^{-/-}$ mice, the small sample size would have a determinant influence.

On the other hand, the difference in correlation was highly significant between the groups, with CamKIIα-*Tdg*$^{-/-}$ cells displaying notable weak correlations. TDG-depleted cells showed predominantly weaker spatial stability than in the TDG intact control cells. If the observation of TDG-depleted cells having impaired spatial stability is reliable, this result suggests that TDG is functionally related to CA1 place cell short- and long-term stability. Based on what is known about typical place cells, the CamKIIα-*Tdg*$^{-/-}$ cells display abnormal spatial stability. Normal place cells have been observed to display stable spatial representations for up to 153 days (Thompson & Best, 1990), and, more recently been observed to remain spatially coherent for up to 6 days, even in rotating arenas (Kinsky et al., 2018). These results highlight the ability of the hippocampus to retain consistent relationships between place cells across long timescales. Hence, the TDG-depleted cells stability deviates predominantly from what is evident for normal place cells, and TDG might have a role in altering the genetic expression in these cells, resulting in spatial instability.

Considering the high significance of correlational differences in place-field maps between the CamKIIα-*Tdg*$^{-/-}$ cells and the control cells, the TDG-depleted mice show lower stability than the control cells. Alternations in stability over time have recently been suggested to rely on the mEC input. The impaired spatial stability in TDG-depleted cells could alternatively be a result of functional impairments in the mEC cell circuitry or in the direct or indirect input pathway from the mEC to the CA1. mEC lesions companied by sensory cue deprivation have been reported to correlate with reduction in typical place cell stability (Jacob et al., 2020). Impairments in normal mEC function, by HCN1 channel blockage, have been hypothesized to influence the ability of the mEC to convey spatial signals by observing correlated reduction in long-term spatial CA1 stability (Cholvin et al., 2018). Impairments in other structures have also been associated with disruption in hippocampal place cell stability (Colvin et al. 2018) and might be an effector of the current finding. This suggests that the observed instability in TDG-depleted place cells might not exclusively be a result of alternations of CA1 cell properties but might be influenced by disruption in other brain structures.

### 4.3 TDG and Place Cell Functionality

Place cells are among the most remarkable neuronal correlates for spatial cognition and have been extensively studied to comprehend hippocampus-dependent memory mechanisms. These cells are known to be selectively active in a particular location within a given environment and maintain their specific place tuning, or place field, for long periods of time, suggesting their role in encoding short-term and long-term memories of learned environments and locations. Moreover, they collectively alter their firing patterns in response to environmental changes, allowing differentiation between dissimilarities and construction of new maps for novel environments. These excitatory neurons of the hippocampus rely on synaptic plasticity varying in time-dependency to structurally alter the neural circuitry functional properties. Regulation of methylation patterns causing genetic downregulation (Miller and Sweatt, 2007; Duke et al., 2017; Miller et al., 2011; Day & Sweatt, 2010) and upregulation (Kaas et al., 2014; Rudenko et al., 2015) is of importance in expression of genes related to synaptic plasticity. The evident role of TDG in genetic demethylation has been established in more recent years and provides plausibility to the hypothesis of TDG playing a role in memory. The extent and route of impact (direct or indirect effect) TDG has on synaptic plasticity have not yet been conclusively demonstrated, as potential confounding factors and secondary mechanisms may overlap or compensate for the functionality in neural correlates of memory. In this project, I investigated whether the CA1 place cells of conditional TDG-deficient mice were functionally normal by recording the activity of hippocampal neurons while the animals freely explored and mapped an open field environment. The observed functional impairments in CA1 place cell spatial tuning properties could thus be a result of impairment in protein synthesis processes facilitating synaptic plasticity between hippocampal cells.

The results from the electrophysiological data analysis were somewhat contradicting. Some differences from normal cell function were observed in the TDG-depleted CA1 place cells. The CamKIIα-*Tdg*$^{-/-}$ place cell population displayed somewhat lower mutual spatial information and less specificity than expected from typical place cells. These observations could be an effect of transcriptional alternations through reduced demethylation and consequential structural changes in the CA1 circuitry. The TDG depletion appeared to influence certain aspects of the general electrophysiological properties of the CA1 place cells, such as information rate, average firing rate, and peak firing rate of place fields. However, the inconsistency in present results makes any definite assumptions of the direct or indirect relation to the knockout of *Tdg* unviable.

Given current evidential grounding, neural correlates of long-term memory, such as late-phase LTP (Baltaci et al., 2019), rely on protein synthesis processes. Based on previous findings, one would expect TDG-depleted spatial selective place cells to primarily show impairments in long-term synaptic alternation (Duke et al., 2017). When the gene transcription pattern involved in place cell protein synthesis is altered by experimentally changing the expression of demethylation enzymes, in this case, TDG, this would reconstruct the expression of genes and thus alter the long-term capabilities of storing a memory through synaptic plasticity (Baltaci et al., 2019). The current finding is not fully consistent with this premise, as the short-term stability of TDG-depleted place cells was impaired to the same extent as the long-term stability. Despite instability independent of time frame, the observations of significant long-term instability in CamKIIα-*Tdg*$^{-/-}$ cells are compatible with Duke et al. (2017) reports of coordinated increasing DNA methylation changes in CA1 in long-term learning and what is reasonable to expect from TDG-depleted cells. This interpretation discounts the weak stability test reliability and small sample size. However, place cell global remapping was found to be unaffected by the reduction of available TDG, being consistent with what was expected for the CamKIIα-*Tdg*$^{-/-}$ cells.

Furthermore, as previously stated, the hippocampal formation is a highly interconnected structure (Figure 2), and the fact that *Tdg* is mainly knocked out in areas where the CamKIIα promotor is active, being the pyramidal CA1 layer supports the possibility that other spatially correlated areas compensate for the depletion of TDG in CA1 place cells. The CA1 spatial cells rely on their connections to other parts of the hippocampal formation to compose their full spatial representation. In the case of incomplete hippocampal knockout of *Tdg*, intact functional properties of CA1 place cells could be a result of spatial input from other hippocampal areas completing the spatial representation and compensating for the loss of transcriptional regulation properties in the CA1 place cells. Thus, a complete TDG depletion in other regions associated with spatial memory could enhance the validity of the current results.

### 4.4 Limitations and Future Perspectives

The current research project has provided preliminary support for the role of TDG, a demethylation enzyme, in regulating gene transcription related to neuronal function in the spatial representational system. However, this study has several limitations.

Firstly, a number of methodological shortcomings were present. The sample sizes of mouse subjects and recorded cells were lower than ideally preferred. Individual differences might affect the outcome significantly, which could reduce the effect of genotype. As more data is collected and available for analysis and additional experiments are planned, the research group will address this issue further. Moreover, several of the classified place cells did not display typical place cell characteristics. These methodological issues could justify the low test reliability observed in the place cell stability paradigm. Implementation of more strict filtering for categorizing different spatial cells, as well as closer verification of the manual clustering work before analyzing the data, would significantly advance future investigations.

Secondly, this study tested the functional influence of place cells on the hippocampal representation of space, but the possibility that non-spatially tuned pyramidal cells and other cell types may also play a substantial role, as suggested by Stefanini et al. (2020), is present. Future studies utilizing a recording technique designed to investigate a greater number of cells concurrently would be of value.

Thirdly, my investigation was limited to a mouse model with conditional knockout of *Tdg*, and it is possible that the observed impaired functions of CA1 place cells were due to undetermined changes in the entire hippocampus or even in the whole brain networks following complete TDG depletion in mice. Moreover, it is essential to explore the consequential impact of a potential disturbance of the mEC. An examination of grid modules and their impact on the local CA1 circuitry could contribute to clarifying the grid cell's role in shaping spatial representations in the hippocampus. The mEC and its hippocampal connections are believed to serve as an error-corrector and noise-reducing mechanism. Any disruption to this system may be associated with impairments in spatial functions observed in the TDG-depleted cells.

Finally, TDG has been implicated in epigenetic mechanisms involving DNA modifications and genomic architecture, but this study did not explore the molecular interplay of TDG with epigenetic markers and transcription in hippocampal neurons. Electrophysiological methods are not sufficient to establish a detailed molecular mechanism of how TDG directly regulates synaptic function, which considerably should be an eminent aim for future research.

## 5 Conclusion

This study aimed to elucidate whether the functional specificity and plasticity of CA1 place cells were affected in TDG-depleted hippocampal neurons. To achieve this goal, I (I) wired microdrives to be implanted into the mouse hippocampus, (II) recorded the activity of hippocampal CA1 cell populations in four conditional *Tdg* knockout mice and four control mice, and (III) clustered and analyzed all recorded cell. Of the total 506 clustered cells, I identified 10 categories of spatial cells, in which place cells were further investigated. Some tendencies were observed, in disregard of the small sample size. Overall, the results showed that a larger proportion of place cells and a smaller proportion of speed cells were recorded in the conditional *Tdg* knockout mice, than in the control mice. Regarding the place cells, the average spatial information content was equally high in both genotypes, but within-session stability scores deviated from normality in both groups. TDG-depleted place cells displayed lower spatial information rate and firing rate on average compared to the control cells. This may be an indication of impairments in spatial functionality. To address the second research question, whether TDG impacts the spatial specificity of hippocampal place cells, I extracted information about the place fields of the place cells. The TDG-depleted cells displayed a higher place field peak firing rate, but the number of place fields per cell and field size was invariable across genotypes. The inconsistency in the results makes any conclusions about place cell specificity unreliable. To address the third research question, whether TDG impacts the spatial remapping of hippocampal place cells, I employed a remapping experiment where the mice were recorded while shifting between a familiar and a novel environment twice. No deviances from normality were observed in global remapping capabilities, with low or negative stability scores for both groups, implying intact global remapping in TDG-depleted place cells. To investigate the fourth research question, whether TDG impacts the spatial stability of hippocampal place cells, I tested the mice in the same box with a short-term stability condition (50 min inter-trial intervals) and a long-term condition (24 h inter-trial intervals). In both the short-term and the long-term conditions, the groups had low or moderate correlation coefficients between familiar environments, but the TDG-depleted cells were significantly more unstable compared to the control cells. This might suggest that both the groups had impaired stability, pointing to methodological errors, but that the *Tdg* knockout mice had less stability in CA1 place cell spatial representation. The inconsistency in the results makes any definite conclusions regarding place cell spatial stability unreliable.

## 6 References

Abraham, W. C., Jones, O. D., & Glanzman, D. L. (2019). Is plasticity of synapses the mechanism of long-term memory storage?. *npj Science of Learning, 4*(1), 9.

Alme, C. B., Miao, C., Jezek, K., Treves, A., Moser, E. I., & Moser, M. B. (2014). Place cells in the hippocampus: eleven maps for eleven rooms. *Proceedings of the National Academy of Sciences*, *111*(52), 18428-18435.

Andersen, P. (2006). Inhibitory circuits in the thalamus and hippocampus—an appraisal after 40 years. *Progress in neurobiology*, *78*(3-5), 264-271.

Baltaci, S. B., Mogulkoc, R., & Baltaci, A. K. (2019). Molecular mechanisms of early and late LTP. *Neurochemical research*, *44*, 281-296.

Bannerman, D. M., Bus, T., Taylor, A., Sanderson, D. J., Schwarz, I., Jensen, V., ... & Sprengel, R. (2012). Dissecting spatial knowledge from spatial choice by hippocampal NMDA receptor deletion. *Nature neuroscience*, *15*(8), 1153-1159.

Bannerman, D. M., Sprengel, R., Sanderson, D. J., McHugh, S. B., Rawlins, J. N. P., Monyer, H., & Seeburg, P. H. (2014). Hippocampal synaptic plasticity, spatial memory and anxiety. *Nature reviews neuroscience*, *15*(3), 181-192.

Basu, J., & Siegelbaum, S. A. (2015). The corticohippocampal circuit, synaptic plasticity, and memory. *Cold Spring Harbor perspectives in biology*, *7*(11), a021733.

Bikbaev, A., Neyman, S., Ngomba, R. T., Conn, J., Nicoletti, F., & Manahan-Vaughan, D. (2008). MGluR5 mediates the interaction between late-LTP, network activity, and learning. *PloS one*, *3*(5), e2155.

Bittner, K. C., Milstein, A. D., Grienberger, C., Romani, S., & Magee, J. C. (2017). Behavioral time scale synaptic plasticity underlies CA1 place fields. *Science*, *357*(6355), 1033-1036.

Bliss, T. V. P., Collingridge, G. L., & Morris, R. G. M. (2014). Synaptic plasticity in health and disease: introduction and overview. *Philosophical Transactions of the Royal Society B: Biological Sciences*, *369*(1633), 20130129.

Bliss, T. V., & Lømo, T. (1973). Long-lasting potentiation of synaptic transmission in the dentate area of the anaesthetized rabbit following stimulation of the perforant path. *The Journal of physiology*, *232*(2), 331-356.

Bochtler, M., Kolano, A., & Xu, G. L. (2017). DNA demethylation pathways: additional players and regulators. *Bioessays*, *39*(1), 1-13.

Buchanan, K., & Mellor, J. (2010). The activity requirements for spike timing-dependent plasticity in the hippocampus. *Frontiers in synaptic neuroscience*, 11.

Burgess, N., Cacucci, F., Lever, C., & O'keefe, J. (2005). Characterizing multiple independent behavioral correlates of cell firing in freely moving animals. *Hippocampus, 15*(2), 149-153.

Castillo, P. E., Younts, T. J., Chávez, A. E., & Hashimotodani, Y. (2012). Endocannabinoid signaling and synaptic function. *Neuron*, *76*(1), 70-81.

Cembrowski, M. S., Bachman, J. L., Wang, L., Sugino, K., Shields, B. C., & Spruston, N. (2016). Spatial gene-expression gradients underlie prominent heterogeneity of CA1 pyramidal neurons. *Neuron*, *89*(2), 351-368.

Chai, X. J., & Jacobs, L. F. (2010). Effects of cue types on sex differences in human spatial memory. *Behavioural brain research*, *208*(2), 336-342.

Chi, A. S., & Bernstein, B. E. (2009). Pluripotent chromatin state. *Science*, *323*(5911), 220-221.

Cholvin, T., Hok, V., Giorgi, L., Chaillan, F. A., & Poucet, B. (2018). Ventral midline thalamus is necessary for hippocampal place field stability and cell firing modulation. *Journal of Neuroscience*, *38*(1), 158-172.

Chrobak, J. J., Lörincz, A., & Buzsáki, G. (2000). Physiological patterns in the hippocampo-entorhinal cortex system. *Hippocampus*, *10*(4), 457-465.

Collingridge, G. L., Kehl, S. J., & McLennan, H. T. (1983). Excitatory amino acids in synaptic transmission in the Schaffer collateral-commissural pathway of the rat hippocampus. *The Journal of physiology, 334*(1), 33-46.

Cortázar, D., Kunz, C., Saito, Y., Steinacher, R., & Schär, P. (2007). The enigmatic thymine DNA glycosylase. *DNA repair, 6*(4), 489-504.

Cortázar, D., Kunz, C., Selfridge, J., Lettieri, T., Saito, Y., MacDougall, E., ... & Schär, P. (2011). Embryonic lethal phenotype reveals a function of TDG in maintaining epigenetic stability. *Nature, 470*(7334), 419-423.

Cortellino, S., Xu, J., Sannai, M., Moore, R., Caretti, E., Cigliano, A., ... & Bellacosa, A. (2011). Thymine DNA glycosylase is essential for active DNA demethylation by linked deamination-base excision repair. *Cell*, *146*(1), 67-79.

Crestani, A. P., Krueger, J. N., Barragan, E. V., Nakazawa, Y., Nemes, S. E., Quillfeldt, J. A., ... & Wiltgen, B. J. (2019). Metaplasticity contributes to memory formation in the hippocampus. *Neuropsychopharmacology*, *44*(2), 408-414.

Danielson, N. B., Zaremba, J. D., Kaifosh, P., Bowler, J., Ladow, M., & Losonczy, A. (2016). Sublayer-specific coding dynamics during spatial navigation and learning in hippocampal area CA1. *Neuron*, *91*(3), 652-665.

Daumas, S., Halley, H., Francés, B., & Lassalle, J. M. (2005). Encoding, consolidation, and retrieval of contextual memory: differential involvement of dorsal CA3 and CA1 hippocampal subregions. *Learning & memory*, *12*(4), 375-382.

Davoudi, H., & Foster, D. J. (2019). Acute silencing of hippocampal CA3 reveals a dominant role in place field responses. *Nature neuroscience*, *22*(3), 337-342.

Dawlaty, M. M., Breiling, A., Le, T., Barrasa, M. I., Raddatz, G., Gao, Q., ... & Jaenisch, R. (2014). Loss of Tet enzymes compromises proper differentiation of embryonic stem cells. *Developmental cell, 29*(1), 102-111.

Dekeyzer, S., De Kock, I., Nikoubashman, O., Vanden Bossche, S., Van Eetvelde, R., De Groote, J., ... & Achten, E. (2017). "Unforgettable"–a pictorial essay on anatomy and pathology of the hippocampus. *Insights into imaging*, *8*, 199-212.

Di Prisco, G. V., Huang, W., Buffington, S. A., Hsu, C. C., Bonnen, P. E., Placzek, A. N., ... & Costa-Mattioli, M. (2014). Translational control of mGluR-dependent long-term depression and object-place learning by eIF2α. *Nature neuroscience*, *17*(8), 1073-1082.

Doeller, C. F., Barry, C., & Burgess, N. (2010). Evidence for grid cells in a human memory network. *Nature*, *463*(7281), 657-661.

Dong, C., Madar, A. D., & Sheffield, M. E. (2021). Distinct place cell dynamics in CA1 and CA3 encode experience in new environments. *Nature communications*, *12*(1), 2977.

Duan, Z., & Lu, J. (2020). DNA methyltransferases in depression: an update. *Frontiers in psychiatry*, *11*, 538683.

Duke, C. G., Kennedy, A. J., Gavin, C. F., Day, J. J., & Sweatt, J. D. (2017). Experience-dependent epigenomic reorganization in the hippocampus. *Learning & memory, 24*(7), 278-288.

Eagle, A. L., Gajewski, P. A., & Robison, A. J. (2016). Role of hippocampal activity-induced transcription in memory consolidation. *Rev Neurosci, 27*(6):559–73.

Ekstrom, A. D., Kahana, M. J., Caplan, J. B., Fields, T. A., Isham, E. A., Newman, E. L., & Fried, I. (2003). Cellular networks underlying human spatial navigation. *Nature*, *425*(6954), 184-188.

Fusi, S., Drew, P. J., & Abbott, L. F. (2005). Cascade models of synaptically stored memories. *Neuron, 45*(4), 599-611.

Fyhn, M., Hafting, T., Treves, A., Moser, M. B., & Moser, E. I. (2007). Hippocampal remapping and grid realignment in entorhinal cortex. *Nature*, *446*(7132), 190-194.

Fyhn, M., Molden, S., Witter, M. P., Moser, E. I., & Moser, M. B. (2004). Spatial representation in the entorhinal cortex. *Science*, *305*(5688), 1258-1264.

Gibney, E. R., & Nolan, C. M. (2010). Epigenetics and gene expression. *Heredity*, *105*(1), 4-13.

Gil, M., Ancau, M., Schlesiger, M. I., Neitz, A., Allen, K., De Marco, R. J., & Monyer, H. (2018). Impaired path integration in mice with disrupted grid cell firing. *Nature neuroscience*, *21*(1), 81-91.

Goode, T. D., Tanaka, K. Z., Sahay, A., & McHugh, T. J. (2020). An integrated index: engrams, place cells, and hippocampal memory. *Neuron*, *107*(5), 805-820.

Grienberger, C., Milstein, A. D., Bittner, K. C., Romani, S., & Magee, J. C. (2017). Inhibitory suppression of heterogeneously tuned excitation enhances spatial coding in CA1 place cells. *Nature neuroscience*, *20*(3), 417-426.

Hafting, T., Fyhn, M., Molden, S., Moser, M. B., & Moser, E. I. (2005). Microstructure of a spatial map in the entorhinal cortex. *Nature*, *436*(7052), 801-806.

Hardcastle, K., Maheswaranathan, N., Ganguli, S., & Giocomo, L. M. (2017). A multiplexed, heterogeneous, and adaptive code for navigation in medial entorhinal cortex. *Neuron*, *94*(2), 375-387.

Hardeland, U., Bentele, M., Lettieri, T., Steinacher, R., Jiricny, J., & Schär P. (2001). Thymine DNA glycosylase. In *Progress in Nucleic Acid Research and Molecular Biology,* 235–53.

Hartley, T., Burgess, N., Lever, C., Cacucci, F., & O'keefe, J. (2000). Modeling place fields in terms of the cortical inputs to the hippocampus. *Hippocampus*, *10*(4), 369-379.

He, S., Sun, H., Lin, L., Zhang, Y., Chen, J., Liang, L., ... & Zheng, H. (2017). Passive DNA demethylation preferentially up-regulates pluripotency-related genes and facilitates the generation of induced pluripotent stem cells. *Journal of Biological Chemistry, 292*(45), 18542-18555.

He, Y. F., Li, B. Z., Li, Z., Liu, P., Wang, Y., Tang, Q., ... & Xu, G. L. (2011). Tet-mediated formation of 5-carboxylcytosine and its excision by TDG in mammalian DNA. *Science*, *333*(6047), 1303-1307.

Hebb, D. O. (1949). The first stage of perception: growth of the assembly. *The Organization of Behavior*, *4*(60), 78-60.

Hussaini, S. A., Kempadoo, K. A., Thuault, S. J., Siegelbaum, S. A., & Kandel, E. R. (2011). Increased size and stability of CA1 and CA3 place fields in HCN1 knockout mice. *Neuron*, *72*(4), 643-653.

Inoue, A., & Zhang, Y. (2011). Replication-dependent loss of 5-hydroxymethylcytosine in mouse preimplantation embryos. *Science, 334*(6053), 194-194.

Ito, S., Shen, L., Dai, Q., Wu, S. C., Collins, L. B., Swenberg, J. A., ... & Zhang, Y. (2011). Tet proteins can convert 5-methylcytosine to 5-formylcytosine and 5-carboxylcytosine. *Science*, *333*(6047), 1300-1303.

Jacob, P. Y., Van Cauter, T., Poucet, B., Sargolini, F., & Save, E. (2020). Medial entorhinal cortex lesions induce degradation of CA1 place cell firing stability when self-motion information is used. *Brain and neuroscience advances*, *4*, 2398212820953004.

Jacobs, J., Kahana, M. J., Ekstrom, A. D., Mollison, M. V., & Fried, I. (2010). A sense of direction in human entorhinal cortex. *Proceedings of the National Academy of Sciences*, *107*(14), 6487-6492.

Jeffery, K. J. (2011). Place cells, grid cells, attractors, and remapping. *Neural plasticity*, *2011*.

Jinno, S., & Kosaka, T. (2006). Cellular architecture of the mouse hippocampus: a quantitative aspect of chemically defined GABAergic neurons with stereology. *Neuroscience research*, *56*(3), 229-245.

Jun, H., Bramian, A., Soma, S., Saito, T., Saido, T. C., & Igarashi, K. M. (2020). Disrupted place cell remapping and impaired grid cells in a knockin model of Alzheimer's disease. *Neuron*, *107*(6), 1095-1112.

Kaminsky, Z. A., Tang, T., Wang, S. C., Ptak, C., Oh, G. H., Wong, A. H., ... & Petronis, A. (2009). DNA methylation profiles in monozygotic and dizygotic twins. *Nature genetics*, *41*(2), 240-245.

Kanter, B. R., Lykken, C. M., Avesar, D., Weible, A., Dickinson, J., Dunn, B., ... & Kentros, C. G. (2017). A novel mechanism for the grid-to-place cell transformation revealed by transgenic depolarization of medial entorhinal cortex layer II. *Neuron*, *93*(6), 1480-1492.

Kentros, C., Hargreaves, E., Hawkins, R. D., Kandel, E. R., Shapiro, M., & Muller, R. V. (1998). Abolition of long-term stability of new hippocampal place cell maps by NMDA receptor blockade. *Science*, *280*(5372), 2121-2126.

Kesner, R. P., & Rolls, E. T. (2015). A computational theory of hippocampal function, and tests of the theory: new developments. *Neuroscience & Biobehavioral Reviews*, *48*, 92-147.

Kim, J., & Tsien, R. W. (2008). Synapse-specific adaptations to inactivity in hippocampal circuits achieve homeostatic gain control while dampening network reverberation. *Neuron*, *58*(6), 925-937.

Kinsky, N. R., Sullivan, D. W., Mau, W., Hasselmo, M. E., & Eichenbaum, H. B. (2018). Hippocampal place fields maintain a coherent and flexible map across long timescales. *Current Biology*, *28*(22), 3578-3588.

Kjelstrup, K. B., Solstad, T., Brun, V. H., Hafting, T., Leutgeb, S., Witter, M. P., ... & Moser, M. B. (2008). Finite scale of spatial representation in the hippocampus. *Science*, *321*(5885), 140-143.

Knierim, J. J. (2015). The hippocampus. *Current Biology*, *25*(23), R1116-R1121.

Knierim, J. J., & Zhang, K. (2012). Attractor dynamics of spatially correlated neural activity in the limbic system. *Annual review of neuroscience*, *35*, 267-285.

Knudsen, E. B. and Wallis, J. D. (2021) Hippocampal neurons construct a map of an abstract value space, Cell, 184(18), pp. 4640-4650.e4610. doi: https://doi.org/10.1016/j.cell.2021.07.010.

Kolb, B., & Gibb, R. (2014). Searching for the principles of brain plasticity and behavior. *Cortex, 58*, 251-260.

Kriaucionis, S., & Heintz, N. (2009). The nuclear DNA base 5-hydroxymethylcytosine is present in Purkinje neurons and the brain. *Science*, *324*(5929), 929-930.

Krokan, H. E., & Bjørås, M. (2013). Base excision repair. *Cold Spring Harbor perspectives in biology, 5*(4), a012583.

Kropff, E., & Treves, A. (2008). The emergence of grid cells: Intelligent design or just adaptation?. *Hippocampus*, *18*(12), 1256-1269.

Krupic, J., Burgess, N., & O’Keefe, J. (2012). Neural representations of location composed of spatially periodic bands. *Science*, *337*(6096), 853-857.

Kunath, N., Bugaj, A. M., Bigonah, P., Fernandez-Berrocal, M. S., Bjørås, M., & Ye, J. (2021). DNA repair enzyme NEIL3 enables a stable neural representation of space by shaping transcription in hippocampal neurons. *Iscience, 24*(12), 103470.

Landgrave-Gómez, J., Mercado-Gómez, O., & Guevara-Guzmán, R. (2015). Epigenetic mechanisms in neurological and neurodegenerative diseases. *Frontiers in cellular neuroscience*, *9*, 58.

Latuske, P., Kornienko, O., Kohler, L., & Allen, K. (2018). Hippocampal remapping and its entorhinal origin. *Frontiers in behavioral neuroscience*, *11*, 253.

Lee, I., & Kesner, R. P. (2004). Differential contributions of dorsal hippocampal subregions to memory acquisition and retrieval in contextual fear-conditioning. *Hippocampus*, *14*(3), 301-310.

Lein, E. S., Zhao, X., & Gage, F. H. (2004). Defining a molecular atlas of the hippocampus using DNA microarrays and high-throughput in situ hybridization. *Journal of Neuroscience, 24*(15), 3879-3889.

Leutgeb, S., Leutgeb, J. K., Barnes, C. A., Moser, E. I., McNaughton, B. L., & Moser, M. B. (2005). Independent codes for spatial and episodic memory in hippocampal neuronal ensembles. *Science*, *309*(5734), 619-623.

Leutgeb, S., Ragozzino, K. E., & Mizumori, S. J. (2000). Convergence of head direction and place information in the CA1 region of hippocampus. *Neuroscience, 100*(1), 11-19.

Lever, C., Burton, S., Jeewajee, A., O'Keefe, J., & Burgess, N. (2009). Boundary vector cells in the subiculum of the hippocampal formation. *Journal of Neuroscience*, *29*(31), 9771-9777.

Li, T., Arleo, A., & Sheynikhovich, D. (2020). Modeling place cells and grid cells in multi-compartment environments: Entorhinal–hippocampal loop as a multisensory integration circuit. *Neural Networks*, *121*, 37-51.

Li, Y. Q., Zhou, P. Z., Zheng, X. D., Walsh, C. P., & Xu, G. L. (2007). Association of Dnmt3a and thymine DNA glycosylase links DNA methylation with base-excision repair. *Nucleic acids research, 35*(2), 390-400.

Li, Y., Xu, J., Liu, Y., Zhu, J., Liu, N., Zeng, W., ... & Zhang, X. (2017). A distinct entorhinal cortex to hippocampal CA1 direct circuit for olfactory associative learning. *Nature neuroscience*, *20*(4), 559-570.

Lu, X., & Bilkey, D. K. (2010). The velocity-related firing property of hippocampal place cells is dependent on self-movement. *Hippocampus*, *20*(5), 573-583.

Magee, J. C., & Grienberger, C. (2020). Synaptic plasticity forms and functions. *Annual review of neuroscience*, *43*, 95-117.

Maiti, A., & Drohat, A. C. (2011). Thymine DNA glycosylase can rapidly excise 5-formylcytosine and 5-carboxylcytosine: potential implications for active demethylation of CpG sites. *Journal of Biological Chemistry*, *286*(41), 35334-35338.

Malfatti, M. C., Antoniali, G., Codrich, M., & Tell, G. (2021). Coping with RNA damage with a focus on APE1, a BER enzyme at the crossroad between DNA damage repair and RNA processing/decay. *DNA repair, 104*, 103133.

Malik, R., Dougherty, K. A., Parikh, K., Byrne, C., & Johnston, D. (2016). Mapping the electrophysiological and morphological properties of ca 1 pyramidal neurons along the longitudinal hippocampal axis. *Hippocampus*, *26*(3), 341-361.

Mankin, E. A., Diehl, G. W., Sparks, F. T., Leutgeb, S., & Leutgeb, J. K. (2015). Hippocampal CA2 activity patterns change over time to a larger extent than between spatial contexts. *Neuron*, *85*(1), 190-201.

Masurkar, A. V., Srinivas, K. V., Brann, D. H., Warren, R., Lowes, D. C., & Siegelbaum, S. A. (2017). Medial and lateral entorhinal cortex differentially excite deep versus superficial CA1 pyramidal neurons. *Cell reports, 18*(1), 148-160.

Mazher, K. M., & Hassan, R. M. (2021). Histological, histochemical, and immunohistochemical studies of hippocampus in male New Zealand rabbits. *The Anatomical Record*, *304*(2), 393-399.

Mercer, A., & Thomson, A. M. (2017). Cornu Ammonis Regions–Antecedents of Cortical Layers?. *Frontiers in neuroanatomy*, *11*, 83.

Meyer, A. H., Katona, I., Blatow, M., Rozov, A., & Monyer, H. (2002). In vivo labeling of parvalbumin-positive interneurons and analysis of electrical coupling in identified neurons. *Journal of Neuroscience, 22*(16), 7055-7064.

Milior, G., Di Castro, M. A., Sciarria, L. P., Garofalo, S., Branchi, I., Ragozzino, D., ... & Maggi, L. (2016). Electrophysiological properties of CA1 pyramidal neurons along the longitudinal axis of the mouse hippocampus. *Scientific reports*, *6*(1), 1-9.

Mizuseki, K., Diba, K., Pastalkova, E., & Buzsáki, G. (2011). Hippocampal CA1 pyramidal cells form functionally distinct sublayers. *Nature neuroscience*, *14*(9), 1174-1181.

Montchal, M. E., Reagh, Z. M., & Yassa, M. A. (2019). Precise temporal memories are supported by the lateral entorhinal cortex in humans. *Nature neuroscience*, *22*(2), 284-288.

Moore, L. D., Le, T., & Fan, G. (2013). DNA methylation and its basic function. *Neuropsychopharmacology*, *38*(1), 23-38.

Morris, R. G. M., Anderson, E., Lynch, G. A., & Baudry, M. (1986). Selective impairment of learning and blockade of long-term potentiation by an N-methyl-D-aspartate receptor antagonist, AP5. *Nature, 319*(6056), 774-776.

Moser, E. I., Moser, M. B., & McNaughton, B. L. (2017). Spatial representation in the hippocampal formation: a history. *Nature neuroscience*, *20*(11), 1448-1464.

Muller, R. U., & Kubie, J. L. (1987). The effects of changes in the environment on the spatial firing of hippocampal complex-spike cells. *Journal of Neuroscience*, *7*(7), 1951-1968.

Muller, R. U., Bostock, E., Taube, J. S., & Kubie, J. L. (1994). On the directional firing properties of hippocampal place cells. *Journal of Neuroscience*, *14*(12), 7235-7251.

Müller, U., Bauer, C., Siegl, M., Rottach, A., & Leonhardt, H. (2014). TET-mediated oxidation of methylcytosine causes TDG or NEIL glycosylase dependent gene reactivation. *Nucleic acids research*, *42*(13), 8592-8604.

Naber, P. A., Lopes da Silva, F. H., & Witter, M. P. (2001). Reciprocal connections between the entorhinal cortex and hippocampal fields CA1 and the subiculum are in register with the projections from CA1 to the subiculum. *Hippocampus, 11*(2), 99-104.

Neher, T., Azizi, A. H., & Cheng, S. (2017). From grid cells to place cells with realistic field sizes. *PLoS One*, *12*(7), e0181618.

Neunuebel, J. P., & Knierim, J. J. (2012). Spatial firing correlates of physiologically distinct cell types of the rat dentate gyrus. *Journal of Neuroscience*, *32*(11), 3848-3858.

Nilssen, E. S., Doan, T. P., Nigro, M. J., Ohara, S., & Witter, M. P. (2019). Neurons and networks in the entorhinal cortex: A reappraisal of the lateral and medial entorhinal subdivisions mediating parallel cortical pathways. *Hippocampus*, *29*(12), 1238-1254.

Nishiyama, M., Hong, K., Mikoshiba, K., Poo, M. M., & Kato, K. (2000). Calcium stores regulate the polarity and input specificity of synaptic modification. *Nature*, *408*(6812), 584-588.

O'Keefe, J. (1976). Place units in the hippocampus of the freely moving rat. *Experimental neurology*, *51*(1), 78-109.

O'Keefe, J. and Nadel, L. (1978) The hippocampus as a cognitive map. Oxford university press.

O'Keefe, J., & Burgess, N. (1996). Geometric determinants of the place fields of hippocampal neurons. *Nature*, *381*(6581), 425-428.

O'Keefe, J., & Dostrovsky, J. (1971). The hippocampus as a spatial map: preliminary evidence from unit activity in the freely-moving rat. *Brain research.*

Ohno-Shosaku, T., Tanimura, A., Hashimotodani, Y., & Kano, M. (2012). Endocannabinoids and retrograde modulation of synaptic transmission. *The Neuroscientist*, *18*(2), 119-132.

Onodera, A., González-Avalos, E., Lio, C. W. J., Georges, R. O., Bellacosa, A., Nakayama, T., & Rao, A. (2021). Roles of TET and TDG in DNA demethylation in proliferating and non-proliferating immune cells. Genome Biology, 22(1), 1-27.

Park, E., Dvorak, D., & Fenton, A. A. (2011). Ensemble place codes in hippocampus: CA1, CA3, and dentate gyrus place cells have multiple place fields in large environments. *PloS one*, *6*(7), e22349.

Park, S. A., Miller, D. S. and Boorman, E. D. (2021) Inferences on a multidimensional social hierarchy use a grid-like code. *Nat Neurosci, 24*(9), pp. 1292-1301. doi: 10.1038/s41593-021-00916-3.

Parmar, S. K., Pruthi, N., Ravindranath, R., Ravindranath, Y., Somanna, S., & Philip, M. (2018). Anatomical variations of the temporomesial structures in normal adult brain-A cadaveric study. *Journal of neurosciences in rural practice*, *9*(03), 317-325.

Pastalkova, E., Serrano, P., Pinkhasova, D., Wallace, E., Fenton, A. A., & Sacktor, T. C. (2006). Storage of spatial information by the maintenance mechanism of LTP. *Science*, *313*(5790), 1141-1144.

Pedrosa, V., & Clopath, C. (2020). The interplay between somatic and dendritic inhibition promotes the emergence and stabilization of place fields. *PLoS computational biology*, *16*(7), e1007955.

Péterfi, Z., Urbán, G. M., Papp, O. I., Németh, B., Monyer, H., Szabó, G., ... & Katona, I. (2012). Endocannabinoid-mediated long-term depression of afferent excitatory synapses in hippocampal pyramidal cells and GABAergic interneurons. *Journal of Neuroscience*, *32*(41), 14448-14463.

Poon, C. H., Chan, Y. S., Fung, M. L., & Lim, L. W. (2020). Memory and neuromodulation: A perspective of DNA methylation. *Neuroscience & Biobehavioral Reviews, 111*, 57-68.

Portela, A., & Esteller, M. (2010). Epigenetic modifications and human disease. *Nature biotechnology*, *28*(10), 1057-1068.

Qazi, T. J., Quan, Z., Mir, A., & Qing, H. (2018). Epigenetics in Alzheimer's disease: perspective of DNA methylation. *Molecular Neurobiology*, *55*, 1026-1044.

Reagh, Z. M., & Yassa, M. A. (2014). Object and spatial mnemonic interference differentially engage lateral and medial entorhinal cortex in humans. *Proceedings of the National Academy of Sciences*, *111*(40), E4264-E4273.

Rennó-Costa, C., & Tort, A. B. (2017). Place and grid cells in a loop: implications for memory function and spatial coding. *Journal of Neuroscience*, *37*(34), 8062-8076.

Rennó-Costa, C., Lisman, J. E., & Verschure, P. F. (2010). The mechanism of rate remapping in the dentate gyrus. *Neuron*, *68*(6), 1051-1058.

Rueckemann, J. W., DiMauro, A. J., Rangel, L. M., Han, X., Boyden, E. S., & Eichenbaum, H. (2016). Transient optogenetic inactivation of the medial entorhinal cortex biases the active population of hippocampal neurons. *Hippocampus*, *26*(2), 246-260.

Sargolini, F., Fyhn, M., Hafting, T., McNaughton, B. L., Witter, M. P., Moser, M. B., & Moser, E. I. (2006). Conjunctive representation of position, direction, and velocity in entorhinal cortex. *Science*, *312*(5774), 758-762.

Schacter, D. L., Addis, D. R., & Buckner, R. L. (2007). Remembering the past to imagine the future: the prospective brain. *Nature reviews neuroscience*, *8*(9), 657-661.

Schiller, D., Eichenbaum, H., Buffalo, E. A., Davachi, L., Foster, D. J., Leutgeb, S., & Ranganath, C. (2015). Memory and space: towards an understanding of the cognitive map. Journal of Neuroscience, 35(41), 13904-13911.

Schlesiger, M. I., Boublil, B. L., Hales, J. B., Leutgeb, J. K., & Leutgeb, S. (2018). Hippocampal global remapping can occur without input from the medial entorhinal cortex. *Cell reports, 22*(12), 3152-3159.

Schuermann, D., Weber, A. R., & Schär, P. (2016). Active DNA demethylation by DNA repair: Facts and uncertainties. *DNA repair, 44*, 92-102.

Schwarz, S. D., Grundbacher, E., Hrovat, A. M., Xu, J., Kuśnierczyk, A., Vågbø, C. B., ... & Schuermann, D. (2020). Inducible TDG knockout models to study epigenetic regulation. *F1000 research, 9*, 1112-1112

Sharif, F., Tayebi, B., Buzsáki, G., Royer, S., & Fernandez-Ruiz, A. (2021). Subcircuits of deep and superficial CA1 place cells support efficient spatial coding across heterogeneous environments. *Neuron*, *109*(2), 363-376.

Sheffield, M. E., & Dombeck, D. A. (2019). Dendritic mechanisms of hippocampal place field formation. *Current opinion in neurobiology*, *54*, 1-11.

Sheffield, M. E., Adoff, M. D., & Dombeck, D. A. (2017). Increased prevalence of calcium transients across the dendritic arbor during place field formation. *Neuron*, *96*(2), 490-504.

Skaggs, W., Mcnaughton, B., & Gothard, K. (1992). An information-theoretic approach to deciphering the hippocampal code. *Advances in neural information processing systems, 5*.

Solstad, T., Boccara, C. N., Kropff, E., Moser, M. B., & Moser, E. I. (2008). Representation of geometric borders in the entorhinal cortex. *Science, 322*(5909), 1865-1868.

Solstad, T., Boccara, C. N., Kropff, E., Moser, M. B., & Moser, E. I. (2008). Representation of geometric borders in the entorhinal cortex. *Science*, *322*(5909), 1865-1868.

Solstad, T., Moser, E. I., & Einevoll, G. T. (2006). From grid cells to place cells: a mathematical model. *Hippocampus*, *16*(12), 1026-1031.

Souza, B. C., Pavão, R., Belchior, H., & Tort, A. B. (2018). On information metrics for spatial coding. *Neuroscience, 375*, 62-73.

Stefanini, F., Kushnir, L., Jimenez, J. C., Jennings, J. H., Woods, N. I., Stuber, G. D., ... & Fusi, S. (2020). A distributed neural code in the dentate gyrus and in CA1. *Neuron, 107*(4), 703-716.

Steinacher, R., & Schär, P. (2005). Functionality of human thymine DNA glycosylase requires SUMO-regulated changes in protein conformation. *Current Biology, 15*(7), 616-623.

Sugar, J., & Moser, M. B. (2019). Episodic memory: Neuronal codes for what, where, and when. *Hippocampus, 29*(12), 1190-1205.

Tahiliani, M., Koh, K. P., Shen, Y., Pastor, W. A., Bandukwala, H., Brudno, Y., ... & Rao, A. (2009). Conversion of 5-methylcytosine to 5-hydroxymethylcytosine in mammalian DNA by MLL partner TET1. *Science*, *324*(5929), 930-935.

Tatu, L., & Vuillier, F. (2014). Structure and vascularization of the human hippocampus. *The Hippocampus in Clinical Neuroscience*, *34*, 18-25.

Taube, J. S., Muller, R. U., & Ranck, J. B. (1990). Head-direction cells recorded from the postsubiculum in freely moving rats. I. Description and quantitative analysis. *Journal of Neuroscience*, *10*(2), 420-435.

Tavares, R. M. et al. (2015) A Map for Social Navigation in the Human Brain, *Neuron, 87*(1), pp. 231-243. doi: 10.1016/j.neuron.2015.06.011.

Ten Donkelaar, H. J., Tzourio-Mazoyer, N., & Mai, J. K. (2018). Toward a common terminology for the gyri and sulci of the human cerebral cortex. *Frontiers in Neuroanatomy*, *12*, 93.

Thompson, C. L., Pathak, S. D., Jeromin, A., Ng, L. L., MacPherson, C. R., Mortrud, M. T., ... & Lein, E. S. (2008). Genomic anatomy of the hippocampus. *Neuron*, *60*(6), 1010-1021.

Thompson, L. T., & Best, P. J. (1990). Long-term stability of the place-field activity of single units recorded from the dorsal hippocampus of freely behaving rats. *Brain research*, *509*(2), 299-308.

Tolman, E. C. (1948). Cognitive maps in rats and men. *Psychological review, 55*(4), 189.

Tsao, A., Sugar, J., Lu, L., Wang, C., Knierim, J. J., Moser, M. B., & Moser, E. I. (2018). Integrating time from experience in the lateral entorhinal cortex. *Nature*, *561*(7721), 57-62.

Tsien, J. Z., Huerta, P. T., & Tonegawa, S. (1996). The essential role of hippocampal CA1 NMDA receptor–dependent synaptic plasticity in spatial memory. *Cell*, *87*(7), 1327-1338.

Tulving, E. (1985). Memory and consciousness. *Canadian Psychology/Psychologie canadienne*, *26*(1), 1.

Uhlén, M., Fagerberg, L., Hallström, B. M., Lindskog, C., Oksvold, P., Mardinoglu, A., ... & Pontén, F. (2015). Tissue-based map of the human proteome. *Science, 347*(6220), 1260419.

Valero, M., Cid, E., Averkin, R. G., Aguilar, J., Sanchez-Aguilera, A., Viney, T. J., ... & De La Prida, L. M. (2015). Determinants of different deep and superficial CA1 pyramidal cell dynamics during sharp-wave ripples. *Nature neuroscience*, *18*(9), 1281-1290.

Wang, X., Zhang, C., Szábo, G., & Sun, Q. Q. (2013). Distribution of CaMKIIα expression in the brain in vivo, studied by CaMKIIα-GFP mice. *Brain research, 1518*, 9-25.

Whitlock, J. R., Heynen, A. J., Shuler, M. G., & Bear, M. F. (2006). Learning induces long-term potentiation in the hippocampus. *Science*, *313*(5790), 1093-1097.

Wiebauer, K., & Jiricny, J. (1990). Mismatch-specific thymine DNA glycosylase and DNA polymerase beta mediate the correction of GT mispairs in nuclear extracts from human cells. Proceedings of the National Academy of Sciences, 87(15), 5842-5845.

Winter, S. S., & Taube, J. S. (2014). Head direction cells: from generation to integration. *Space, time and memory in the hippocampal formation*, 83-106.

Witter, M. (2012). Hippocampus. In *The mouse nervous system*(pp. 112-139). Academic Press.

Witter, M. P. (2006). Connections of the subiculum of the rat: topography in relation to columnar and laminar organization. *Behavioural brain research*, *174*(2), 251-264.

Witter, M. P. (2018). Connectivity of the hippocampus. *Hippocampal microcircuits: a computational modeler's resource book*, 5-28

Witter, M. P., Kleven, H., & Flatmoen, A. K. (2017). Comparative contemplations on the hippocampus. *Brain, Behavior and Evolution*, *90*(1), 15-24.

Witter, M. P., Wouterlood, F. G., Naber, P. A., & Van Haeften, T. (2000). Anatomical organization of the parahippocampal-hippocampal network. *Annals of the New York Academy of Sciences*, *911*(1), 1-24.

Xu, W., & Wilson, D. A. (2012). Odor-evoked activity in the mouse lateral entorhinal cortex. *Neuroscience*, *223*, 12-20.

Xue, Z., & Demple, B. (2022). Knockout and inhibition of Ape1: Roles of Ape1 in base excision DNA Repair and modulation of gene expression. *Antioxidants, 11*(9), 1817.

Ye, J., Witter, M. P., Moser, M. B., & Moser, E. I. (2018). Entorhinal fast-spiking speed cells project to the hippocampus. *Proceedings of the National Academy of Sciences*, *115*(7), E1627-E1636.

Younts, T. J., & Castillo, P. E. (2014). Endogenous cannabinoid signaling at inhibitory interneurons. *Current opinion in neurobiology*, *26*, 42-50.

Yu, N. K., Baek, S. H., & Kaang, B. K. (2011). DNA methylation-mediated control of learning and memory. *Molecular brain, 4*(1), 1-9.

Zusso, M., Barbierato, M., Facci, L., Skaper, S. D., & Giusti, P. (2018). Neuroepigenetics and Alzheimer’s disease: an update. *Journal of Alzheimer's Disease*, *64*(3), 671-688.

# 7 Appendix

## Appendix A

***Table 4. Resistance of all channels from each microdrive used for neural recording.***

| Drive | Mouse genotype | Electrode | Recoding before plating (kΩ) | Recording after plating (kΩ) |
|---|---|---|---|---|
| **1** | LoxP-miniTdg | A1 | 900 | 260 |
| | | A2 | 810 | 250 |
| | | A3 | 940 | 270 |
| | | A4 | 1100 | 250 |
| | | B1 | 850 | 250 |
| | | B2 | 1230 | 240 |
| | | B3 | 1050 | 260 |
| | | B4 | 800 | 230 |
| | | C1 | 900 | 200 |
| | | C2 | 850 | 240 |
| | | C3 | 1020 | 250 |
| | | C4 | 950 | 240 |
| | | D1 | 1100 | 130 |
| | | D2 | 840 | 140 |
| | | D3 | 940 | 130 |
| | | D4 | 850 | 150 |
| **2** | LoxP-miniTdg | A1 | 630 | 270 |
| | | A2 | 560 | 240 |
| | | A3 | 700 | 240 |
| | | A4 | 650 | 230 |
| | | B1 | 990 | 270 |
| | | B2 | 650 | 270 |
| | | B3 | 740 | 230 |
| | | B4 | 980 | 260 |
| | | C1 | 920 | 180 |
| | | C2 | 890 | 150 |
| | | C3 | 710 | 170 |
| | | C4 | 1000 | 160 |
| | | D1 | 720 | 150 |
| | | D2 | 400 | 180 |

| | | | | |
|---|---|---|---|---|
| | | D3 | 1100 | 160 |
| | | D4 | 920 | 150 |
| **3** | CamKIIα-Tdg-/- | A1 | 805 | 280 |
| | | A2 | 930 | 270 |
| | | A3 | 905 | 240 |
| | | A4 | 930 | 260 |
| | | B1 | 730 | 170 |
| | | B2 | 600 | 220 |
| | | B3 | 700 | 230 |
| | | B4 | 715 | 180 |
| | | C1 | 450 | 150 |
| | | C2 | 450 | 150 |
| | | C3 | 800 | 230 |
| | | C4 | 810 | 230 |
| | | D1 | 410 | 150 |
| | | D2 | 820 | 150 |
| | | D3 | 710 | 230 |
| | | D4 | 880 | 180 |
| **4** | CamKIIα-Tdg-/- | A1 | 1000 | 250 |
| | | A2 | 680 | 210 |
| | | A3 | 800 | 200 |
| | | A4 | 700 | 250 |
| | | B1 | 750 | 170 |
| | | B2 | 910 | 180 |
| | | B3 | 780 | 240 |
| | | B4 | 700 | 200 |
| | | C1 | 950 | 180 |
| | | C2 | 750 | 190 |
| | | C3 | 800 | 220 |
| | | C4 | 850 | 230 |
| | | D1 | 500 | 200 |
| | | D2 | 580 | 200 |
| | | D3 | 960 | 250 |
| | | D4 | 1000 | 260 |

**Appendix B**

***Table 5. Descriptive and inferential statistics of place cell data.***

| | | ***Control group*** | | ***CamKIIa-Tdg-/- group*** | | | |
|---|---|---|---|---|---|---|---|
| | ***N*** | ***M ± SD*** | ***n*** | ***M ± SD*** | ***n*** | ***t* value*** | **Mean difference** |
| Spatial information content (bits/spike) | 59 | 1.10 ± .54 | 20 | 1.28 ± .65 | 39 | -1.05 | .18 |
| Spatial information rate (bits/sec) | 59 | .29 ± .38 | *20* | .09 ± .12 | 39 | 2.25* | .20 |
| Speed filtered average firing rate | 59 | .26 ± .34 | *20* | .10 ± .10 | 39 | 2.09* | .16 |
| Proportion of cells with multiple fields | | .05 ± .22 | | .10 ± 31 | | .70 | .05 |
| Average size of the place fields ($mm^2$; sample of place fields) | 53 | 106.53± 182.56 | *22* | 110.53 ± .06 | 41 | 1.10 | 4.00 |
| Peak firing rate within the place fields (Hz; sample of place fields) | 53 | 3.03 ± .06 | *22* | .98 ± .56 | 41 | 2.29* | 2.05 |
| Remapping A1B1 (*r*) | 110 | .04 ± .37 | 52 | .19 ± .30 | 58 | -.71 | .05 |
| Remapping B2A2 (*r*) | 130 | .08 ± .34 | 67 | .11 ± .31 | 63 | -.60 | .03 |
| Short-term Stability A1A2 (*r*) | 114 | .30 ± .40 | 56 | 11 ± .30 | 58 | 2.94** | .19 |
| Long-term Stability A0A1 (*r*) | | .22 ± 39 | 71 | .21 ± .38 | 72 | -.23 | .01 |

*Note. r refers Pearson's correlation coefficient*

*Note. M = arithmetic mean, SD = standard deviation*

* $p \leq .05$, ** $p \leq .01$, *** $p \leq .001$

***Table 6. Pairwise comparison of size interval groups for camKIIα-Tdg$^{-/-}$ and control fields.***

| **Sample 1-Sample 2** | **Test Statistic** | **Std. Error** | **Std. Test Statistic** | **Sig.** | **Adj. Sig.**[a] |
|---|---|---|---|---|---|
| Small camKIIα-*Tdg*$^{-/-}$ - small control | 4.038 | 5.761 | .701 | .483 | 1.000 |
| Small camKIIα-*Tdg*$^{-/-}$ - medium camKIIα-*Tdg*$^{-/-}$ | 26.060 | 7.222 | 3.608 | <.001 | .009 |
| Small camKIIα-*Tdg*$^{-/-}$ -medium control | 27.596 | 9.109 | 3.029 | .002 | .069 |
| Small camKIIα-*Tdg*$^{-/-}$ -large ko | 35.060 | 7.222 | 4.855 | <.001 | .000 |
| Small camKIIα-*Tdg*$^{-/-}$ -large control | 40.013 | 10.342 | 3.869 | <.001 | .003 |
| Small camKIIα-*Tdg*$^{-/-}$ - very large camKIIα-*Tdg*$^{-/-}$ | -43.346 | 17.283 | -2.508 | .012 | .340 |
| Small camKIIα-*Tdg*$^{-/-}$ - very large control | -43.346 | 12.445 | -3.483 | <.001 | .014 |
| Small cotrol-medium camKIIα-*Tdg*$^{-/-}$ | 22.022 | 7.951 | 2.770 | .006 | .157 |
| Small cotrol-medium control | 23.558 | 9.697 | 2.429 | .015 | .424 |
| Small cotrol-large camKIIα-*Tdg*$^{-/-}$ | 31.022 | 7.951 | 3.902 | <.001 | .003 |
| Small cotrol-large control | 35.974 | 10.863 | 3.312 | <.001 | .026 |
| Small cotrol- very large camKIIα-*Tdg*$^{-/-}$ | -39.308 | 17.601 | -2.233 | .026 | .715 |
| Small cotrol- very large control | -39.308 | 12.882 | -3.051 | .002 | .064 |
| Medium camKIIα-*Tdg*$^{-/-}$ -medium control | 1.536 | 10.630 | .144 | .885 | 1.000 |
| Medium camKIIα-*Tdg*$^{-/-}$ -large camKIIα-*Tdg*$^{-/-}$ | 9.000 | 9.066 | .993 | .321 | 1.000 |
| Medium camKIIα-*Tdg*$^{-/-}$ -large control | 13.952 | 11.704 | 1.192 | .233 | 1.000 |
| Medium camKIIα-*Tdg*$^{-/-}$ - very large camKIIα-*Tdg*$^{-/-}$ | -17.286 | 18.131 | -.953 | .340 | 1.000 |
| Medium camKIIα-*Tdg*$^{-/-}$ - very large control | -17.286 | 13.599 | -1.271 | .204 | 1.000 |
| Medium control-large camKIIα-*Tdg*$^{-/-}$ | 7.464 | 10.630 | .702 | .483 | 1.000 |

| | | | | | |
|---|---|---|---|---|---|
| Medium control-large control | 12.417 | 12.954 | .959 | .338 | 1.000 |
| Medium control- very large camKIIα-*Tdg*$^{-/-}$ | -15.750 | 18.962 | -.831 | .406 | 1.000 |
| Medium control- very large control | -15.750 | 14.688 | -1.072 | .284 | 1.000 |
| Large camKIIα-*Tdg*$^{-/-}$ -large control | 4.952 | 11.704 | .423 | .672 | 1.000 |
| Large camKIIα-*Tdg*$^{-/-}$ - very large ko | -8.286 | 18.131 | -.457 | .648 | 1.000 |
| Large camKIIα-*Tdg*$^{-/-}$ - very large control | -8.286 | 13.599 | -.609 | .542 | 1.000 |
| Large control- very large camKIIα-*Tdg*$^{-/-}$ | -3.333 | 19.584 | -.170 | .865 | 1.000 |
| Large control- very large control | -3.333 | 15.483 | -.215 | .830 | 1.000 |
| Very large control- very large camKIIα-*Tdg*$^{-/-}$ | .000 | 20.772 | .000 | 1.000 | 1.000 |

*Each row tests the null hypothesis that the Sample 1 and Sample 2 distributions are the same. Asymptotic significances (2-sided tests) are displayed. The significance level is .050.*

*a. Significance values have been adjusted by the Bonferroni correction for multiple tests.*

## Appendix C

***Table 7. Primers for genotyping***

| **Allele** | **Primer** | **Sequence** | **Product size** |
|---|---|---|---|
| mini*Tdg* | Compl Forward | AAATACTCTGAGTCCAAACCGGG | 0.65 kb |
| | Tdg C Reverse | TGGTGAATCCGATGCCGTACTTG | |
| CAG-gfp | CAG-St-eGFP-Forward | CTTCAGCCGCTACCCCGACCACA | 0.5 kb |
| | CAG-St-eGFP-Reverse | ATCGCGCTTCTCGTTGGGGTCTTT | |
| *Tdg* WT | GT Tdg D Forward | TTGCGTGGGAGTAACCGAGC | 0.6 kb |
| | GT Tdg B Reverse | GATGCACTCGGGAGACTTACAG | |
| CamKIIα-Cre | JAX_10884_Forward | GTTCTCCGTTTGCACTCAGG | 0.3 kb |
| | JAX_oIMR8990_Reverse | CAGGTTCTTGCGAACCTCAT | |

## Appendix E

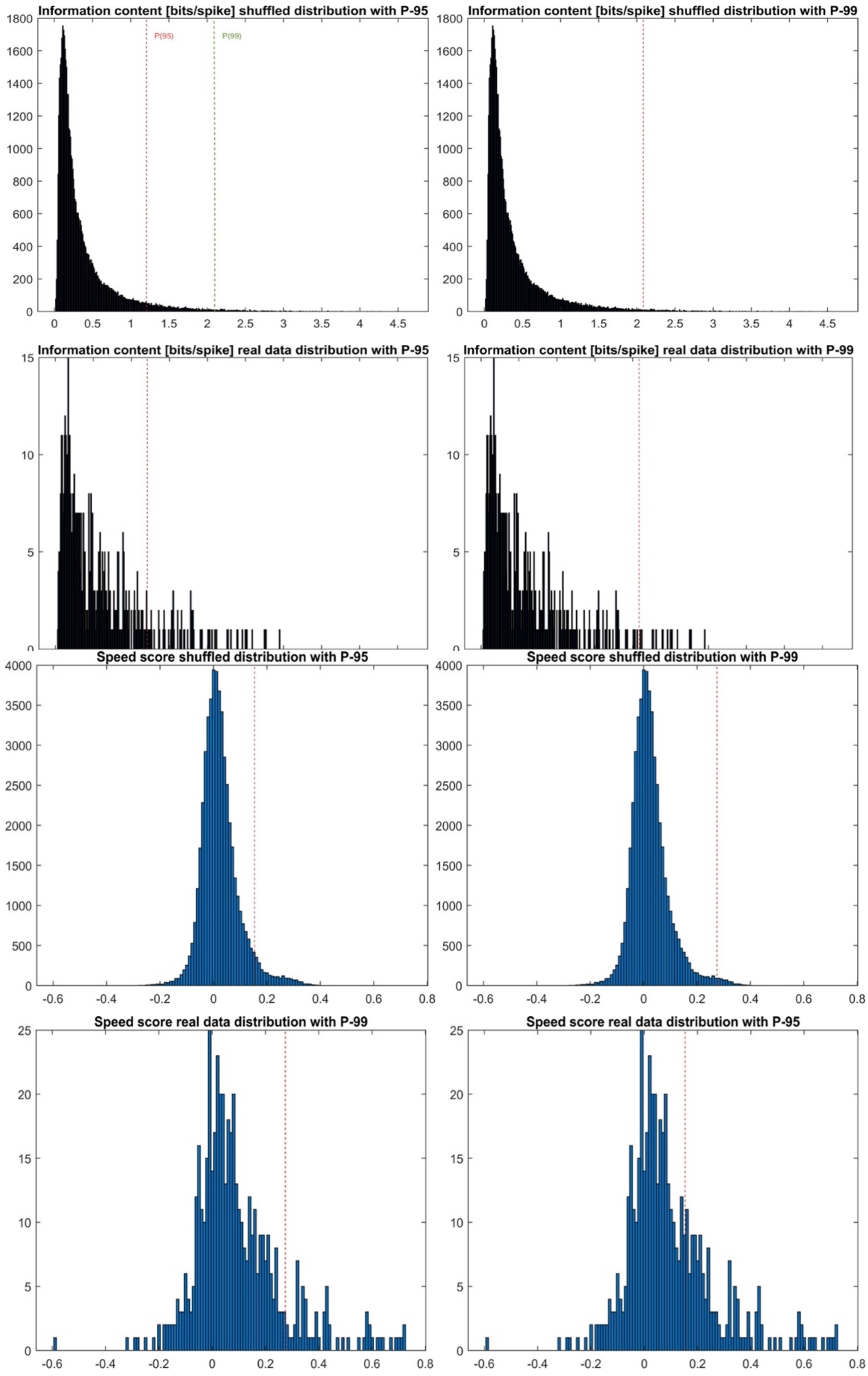
Information content [bits/spike] shuffled distribution with P-95
P(95)
P(99)
0
200
400
600
800
1000
1200
1400
1600
1800
0
0.5
1
1.5
2
2.5
3
3.5
4
4.5
Information content [bits/spike] shuffled distribution with P-99
Information content [bits/spike] real data distribution with P-95
Information content [bits/spike] real data distribution with P-99
0
5
10
15
Speed score shuffled distribution with P-95
Speed score shuffled distribution with P-99
0
500
1000
1500
2000
2500
3000
3500
4000
-0.6
-0.4
-0.2
0
0.2
0.4
0.6
0.8
Speed score real data distribution with P-99
Speed score real data distribution with P-95
0
5
10
15
20
25

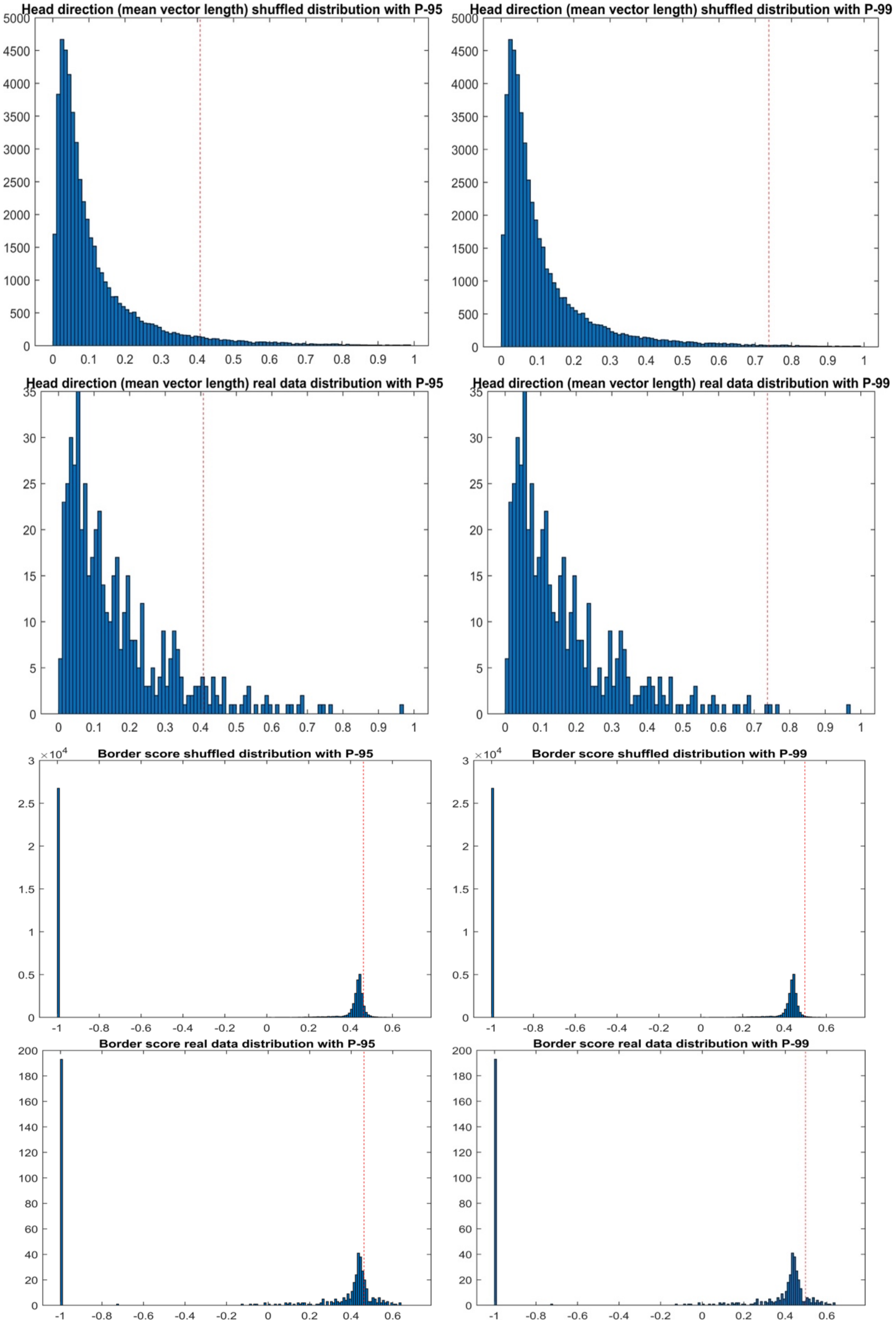

***Figure 17. Real and shuffled cell distribution as a function of information content score, speed score, head direction score and (P95 and P99)***

# Appendix F

CamKIIα-*Tdg*$^{-/-}$:

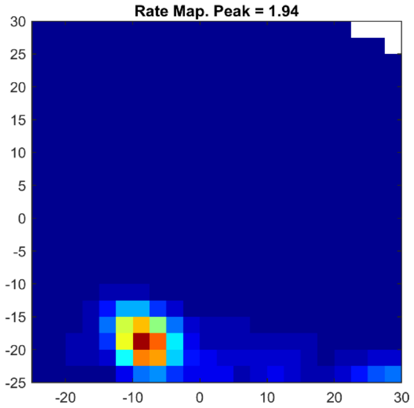
Rate Map. Peak = 1.94

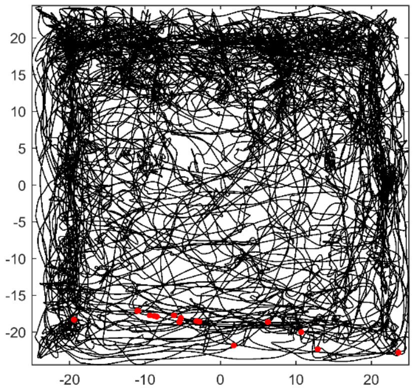

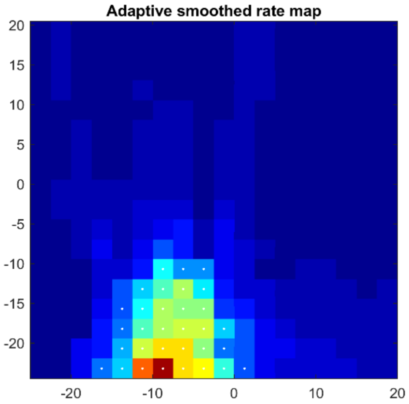
Adaptive smoothed rate map

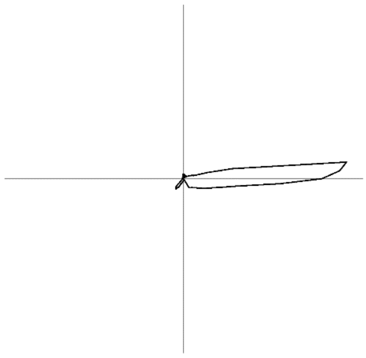

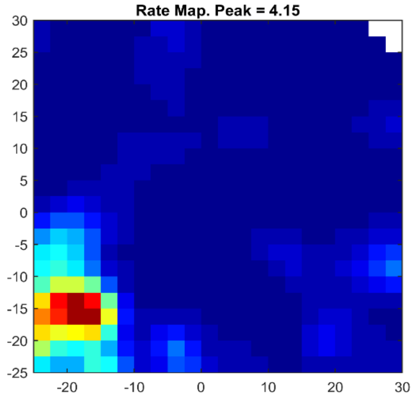
Rate Map. Peak = 4.15

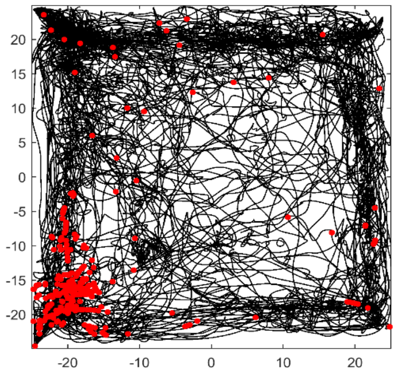

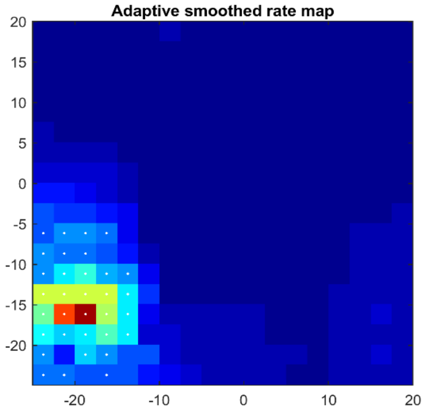
Adaptive smoothed rate map

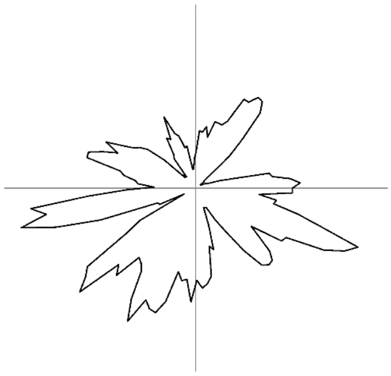

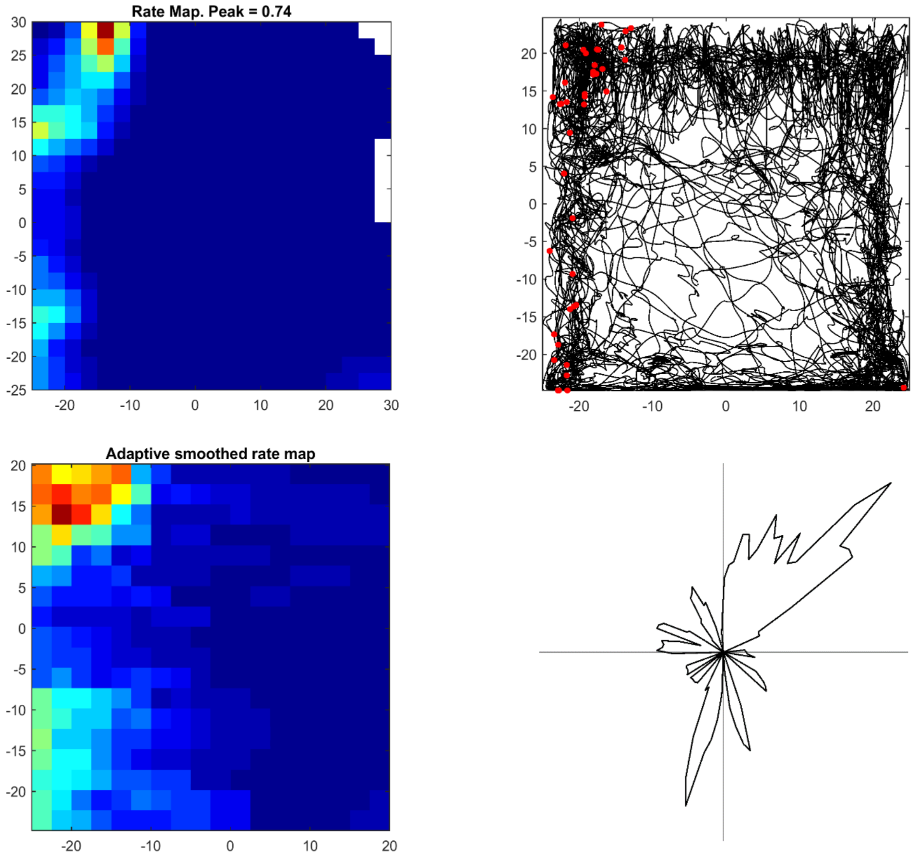
Rate Map. Peak = 0.74
30
25
20
15
10
5
0
-5
-10
-15
-20
-25
-20
-10
0
10
20
30
Adaptive smoothed rate map

Control:

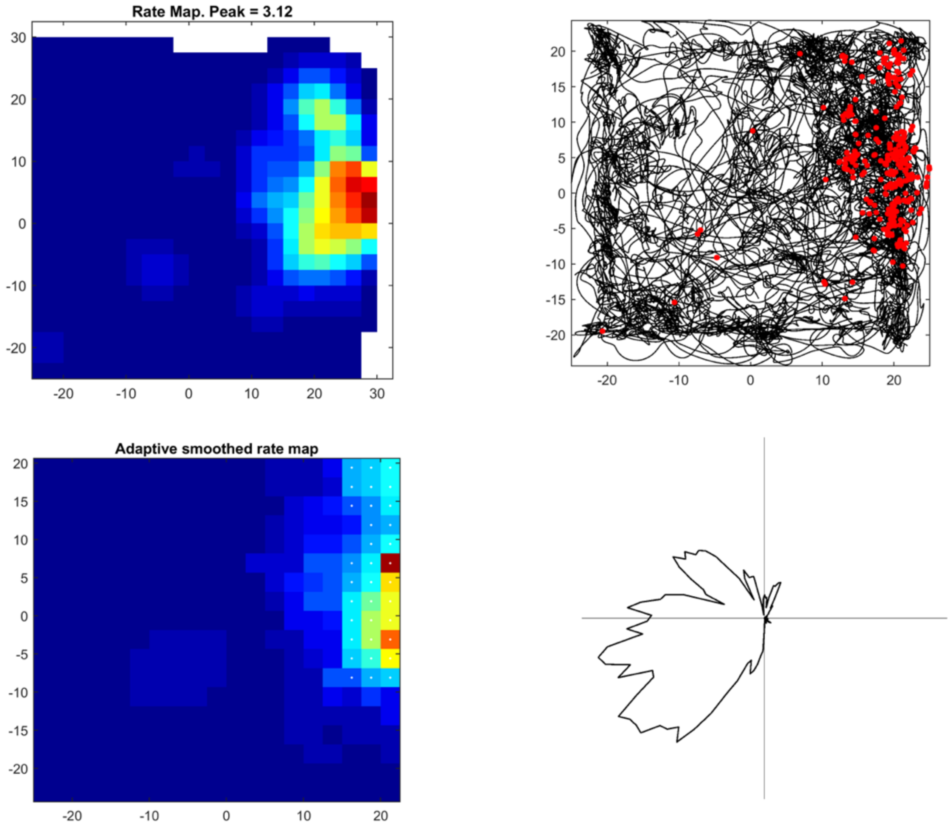
Rate Map. Peak = 3.12
30
20
10
0
-10
-20
-20
-10
0
10
20
30
Adaptive smoothed rate map

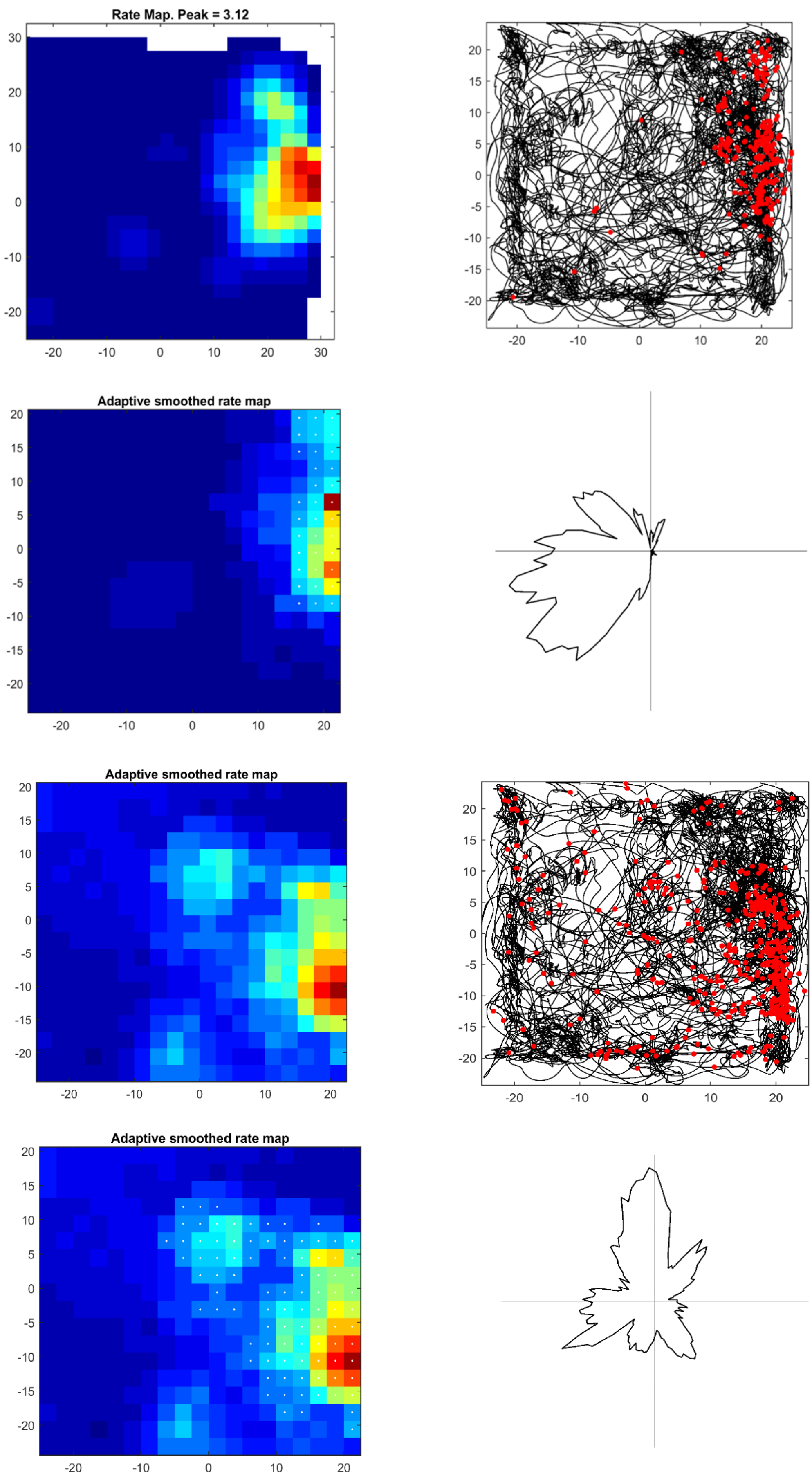

***Figure 27. A sample of rate maps, adaptive smoothed rate maps, trajectory maps and polar maps from camKIIα-Tdg$^{-/-}$ and control cells in A1.*** Examples of tree cells from *camKIIα-*Tdg$^{-/-}$ mice (upper) and control mice (lower) presented in groups of four maps. Each group contains a rate map (upper left), an adaptive smoothed map (lower left), a trajectory map (upper right), and a polar map (lower right).

# Appendix G
## Parameters used for classification of cell types

```
% Percentile value for the head direction arc calculation. Arc is between two
points with
% values around globalPeak * (p.percentile / 100). Value is in percentage.
p.percentile = 50; % [%]

% Width of the line that marks the outline of the head direction rate map (polar
plot).
% Value is set in points. (1 point = 1/72 inch)
% Default width is 0.5 points.
p.hdMapLineWidth = 1;

% Bin width for turning curves (head direction, moving direction rate maps).
p.hdBinWidth = 3; % [degrees]

% Smoothing size in bins for turning curves (head direction, trajectory, moving
direction maps).
% (0 = no smoothing)
p.hdSmooth = 1; % [bins]

% Head direction measurements are separated in 3 different groups:
% 1) clockwise direction (CW). Samples with angular velocity v >
p.hdTurnSpeedThreshold.
% 2) counterclockwise direction (CCW). Samples with angular velocity v < -
p.hdTurnSpeedThreshold.
% 3) still. Samples with abs(v) < p.hdStillSpeedThreshold.
% If p.hdStillSpeedThreshold < abs(v) < p.hdTurnSpeedThreshold, then the sample is
discarded.
p.hdTurnSpeedThreshold = 90; % [degrees/sec]

% See p.hdTurnSpeedThreshold.
p.hdStillSpeedThreshold = 15; % [degrees/sec]

% Format of the output images
% format = 'bmp' (24 bit)
% format = 'png'
% format = 'eps'
% format = 'jpg'
% format = 'tiff' (24 bit)
% format = 'fig' (Matlab figure)
% format = 'pdf'
p.imageFormat = 'jpg';

% DPI setting for stored images
p.imageDpi = 600;

% Number of time shifts during the time shift analysis.
% Example. We have recording sampling rate 50 Hz = 20 msec. With
% p.numTimeShifts == 5, we will include time from -5*20 msec up to 5*20 msec.
p.numTimeShifts = 5;

% Length of area at the left hand side of track that have to be cut off.
p.leftCutOff = 0; % [cm]

% Length of area at the right hand side of track that have to be cut off.
p.rightCutOff = 0; % [cm]

% Bin width for firing rate maps
p.binWidth = 2.5; % [cm]

% Controls the colour-scaling of a rate map plot. You can use this parameter if you
want to
% plot several rate maps with the same colour scale.
%
% Format is p.rateMapScalling = [lower_end higher_end], where both values are given
in Hz.
```

```
% When empty ([]) or NaN, then the plot is autoscaled: the lowest value of
% the map is represented by dark blue and the highest value of the map is
represented by brown.
% Otherwise everything which is below or equal 'lower_end' value is represented by
dark blue,
% and 'higher_end' is represented by brown. It's possible to set only one value to
NaN:
% p.rateMapScalling = [NaN 15] will scale from the minimum value of the map up to
15 Hz.
% Default is p.rateMapScalling = [];, which means autoscale is used.
p.rateMapScalling = []; % Hz

% Smoothing size in bins for firing rate maps. (0 = no smoothing)
p.smooth = 2; % [bins]

% Determines how to deal with bins with no animal activity on the rate map.
% 'on' means that these bins will be blank and white (nan values are used).
% 'off' means that these bins will be 0 (results in deep blue colour).
% See help of function analyses.map.
p.rateMapShowBlanks = 'off';

% Low and high speed thresholds. Defines segments of path where animal moves
slower/faster
% than the threshold. Such segments are removed from the processing. Set it to zero
(0)
% to keep everything. Values are in centimetres per second.
% Common values found in GridnessScript are [2.5 100]
p.speedFilter = [2 100]; % [cm/s]

% Number of bins for a rate map. Sometimes it is more desirable to create
% rate maps in fixed number of bins, independently of bin width in
% centimetres. The parameter numBins could be either a single value or a
% two-element vector, i.e. [20 30]. If a single value is provided, then
% the map is divided in equal number of bins along both axes.
% !!! Most of the scripts doesn't use this value. Instead bin numbers is calculated
% through p.binWidth. Check the script you are running if it uses p.numBins. !!!
p.numBins = 20; % [20x20] for 2D maps

% Threshold for how far a rat can move (150cm/s) in one sample
p.distanceThreshold = 100;

% Set the maximum time gap in the position data that should be interpolated.
% If there are gaps with duration longer than this, then the samples will be left
as NaN.
p.maxInterpolationGap = 3; % [sec]% default 1

% There could be outliers in tracked position samples. These are commonly several
% values between longer list of NaNs. They lie far away from 'good' points, so
% we discard everything that is further away than p.posStdThreshold*STD. If your
% data is somehow truncated strangely, then try to increase this threshold.
% Default value is 2.5
p.posStdThreshold = 2.5;

% This parameter is used during firing rate map calculation. Minimum time an animal
% must spend in a bin, in order to include this bin in the resulting firing map.
% In other words if an animal has spent less than p.binMinTime in a bin, the value
% of this bin is set to NaN. Default value is 0, meaning that all bins matter.
p.binMinTime = 0;

% During light stimulation analysis we are interested in spikes that occur some
% time before and after an event. This parameter defines this 'some time'. First
% value is how much milliseconds we should look back. Second value is how much
% milliseconds we should include after the event.
% Default values are 50 ms before the event and 100 ms after the event.
p.lightPulseOffset_ms = [50 100]; % [ms], millisecond

% Duration of stimulation phase in seconds. In use only for certain scripts!
% Example: There are light pulses of some frequency for total duration of
```

```
% stimulationDuration_sec == 5 seconds.
% Default value is 5, but you should really adjust it to your experiment;
p.stimulationDuration_sec = 5;

% Alpha value for adaptive smoothing rate map calculation. Also in use for
% the spatial information calculation.
p.alphaValue = 10000;

% Nx2 matrix of session name pairs that should be used for rate map cross-
correlation.
% Session name for NeuraLynx data is the name of the folder where data is located.
% Consider this example:
%   You have data in folders (and they appear in exact same order in your input
file)
%       N:\wernle\LOOP_Project\18914\Recordings\050913_rec1\02. s1 To ends1
%       N:\wernle\LOOP_Project\18914\Recordings\050913_rec1\04. s2 To ends2
%       N:\wernle\LOOP_Project\18914\Recordings\050913_rec1\06. s3 To ends3
%   which are referenced as A, B, C correspondingly. So you want to correlate
%   A vs. C and B vs. C. Your parameter should be:
%   p.correlationSessionNames = {'02. s1 To ends1' '06. s3 To ends3'; '04. s2 To
ends2' '06. s3 To ends3'};
% You can divide long line into smaller ones by using ellipses (...). Example:
% p.correlationSessionNames = {'02. s1 To ends1' '06. s3 To ends3'; ...
% '04. s2 To ends2' '06. s3 To ends3'; ...
% '02. s1 To ends1' '04. s2 To ends2'};
% DO NOT FORGET to divide pairs with ; character!
p.correlationSessionNames = {};

% Number of bins that are used as 'a single' entity during the correlation of rate
maps.
% Example. We have two maps of size 20x20. If we do correlation with
p.numCorrelationBins == 1,
% then the result is a single value. However, for p.numCorrelationBins == 2, the
result will be
% an array with 20/2 = 10 elements.
p.numCorrelationBins = 1;

% Some scripts need to divide position data into smaller groups. This value
specifies the time
% duration of each group, so that position data is divided into groups of
p.posSampleTime seconds.
p.posSampleTime = 0.2; % [sec]

% Some scripts need to divide position data into smaller number of group. This
value specifies
% number of these groups. For example, p.posNumGroups == 2 will result in division
of position
% data in to halves. It's better to divide into even number of groups, i.e.
multiple of 2
p.posNumGroups = 2;

% Threshold that is used to define place field in a 2D firing map.
% Value above threshold*peak belong to a field (default = 0.2).
p.fieldThreshold2D = 0.2;

% Minimum number of bins in a place field. Fields with fewer bins are not
considered as place
% fields. Remember to adjust this value when you change the bin width (default =
9).
p.fieldMinBins = 8;

% Fields with peak value less than p.fieldMinPeak are considered spurious and
ignored.
% Default value is 1. If this value is zero, then all fields are processed.
% Peak value is normally a rate, however, it's units are not necessary Hz.
p.fieldMinPeak = 1;

% Threshold type, see analyses.placefield1D.
```

```
% Default is '%'
p.fieldThresholdType_1d = '%';

% Threshold value, see analyses.placefield1D.
% Default is 0.2
p.fieldThreshold_1d = 0.2;

% Minimum number of row bins in a place field. See analyses.placefield1D.
% Default is 3
p.fieldMinRows_1d = 3;

% Minimum number of spikes in a place field. See analyses.placefield1D.
% Default is 0
p.fieldMinSpikes_1d = 0;

% Minimum number of bins between adjacent fields. See analyses.placefield1D.
% Default is 0
p.fieldMinDistance_1d = 0;

% Cell array of Lineseries Properties which are passed to Matlab's plot function
% when path plot is created. See Matlab's help (search for Lineseries Properties)
% for a complete list of possible values.
% Default values are: grey color and line width of 0.5 points.
p.plotPath = {'Color', [0.5 0.5 0.5], 'LineWidth', 0.5};

% Cell array of Lineseries Properties which are passed to Matlab's plot function
% in order to plot spikes. Here you can define the color of spikes, their shape
% and size.
% Defaults are: red point of size 15, no line between spikes
p.plotSpikes = {'Marker', '.', 'Color', [1 0 0], 'MarkerSize', 15, 'LineStyle',
'none'};

% Direction of increasing values along y-axis for plots. The value
% could be either 'normal' or 'reverse'. 'Normal' means that values increase from
% bottom to top, 'reverse' means that values decrease from bottom to top.
% Default value is 'normal'. Set to 'reverse' if you want to flip your rate maps
vertically.
% This will also affect path plots.
p.plotYDir = 'normal';

% Trajectory plot is normalized to make it smaller. This happens because trajectory
% is often plotted on the same image as turning curve. Turning curve is normalized,
% i.e. it's maximum value is 1.
% Trajectory plot size is p.trajectoryNorm of 1.
p.trajectoryNorm = 1/4;

% Properties of a trajectory circular plot. Trajectory plot is a histogram of
animal's
% positions binned to degrees 0..360.
% The parameter is a cell array if Lineseries Properties which are passed to
Matlab's
% plot function. See Matlab's help (search for Lineseries Properties) for a
complete
% list of possible values.
% Default values are: blue color
p.trajectoryPlot = {'Color', [0.28 0.6 0.75294]};

% If set to true, data in each group (see p.posNumGroups) is additionally filtered
% by moving direction. Animal should move in all four quadrants of a circle during
% a short period of time. Default is false.
p.filterByMovement = false;

% Value of the average firing rate filter. Each group of data (see p.posNumGroups)
% is additionally filtered by firing rate. If average rate of a group is lower
% than this value, then this group is skipped from the analysis.
% Value of 0 means that the filter is not used. Value units are Hz.
p.averageRateFilter = 0; % [Hz]
```

```
% Search width for the border score calculation. If map is not perfect, but
contains NaN values
% along borders, then the search for border pixels can have NaNs. To mitigate this,
we check
% searchWidth rows/columns near border and if the closest to the border pixel
equals to NaN,
% we search for first non-NaN value in searchWidth rows-columns. Default value is
8.
p.borderSearchWidth = 8;

% Definition of walls along which the border score is calculated. Provided by a
string which
% contains characters that stand for walls:
% T - top wall (we assume the bird-eye view on the arena)
% R - right wall
% B - bottom wall
% L - left wall
% Characters are case insensitive. Default value is 'TRBL' meaning that border
% score is calculated along all walls. Any combination is possible, e.g.
% 'R' to calculate along right wall, 'BL' to calculate along two walls, e.t.c.
p.borderWalls = 'TRBL';

% Recordings are stored in folders that correspond to animal's name or number.
% This function returns part of the stored data path, which is believed
% to be animal's name.
% Consider these example of sessions from an input file:
% * (Axona)       C:\work\recordings\<animal_name>\07040501
% * (Axona)       C:\work\recordings\<animal_name>\trials\07040501
% * (NeuraLynx)   C:\work\recordings\Ivan\050913_rec1\02. s1 To ends1
% * (NeuraLynx)   C:\work\recordings\Ivan\050913_rec2
% To extract animal name from the first path, you have to set animalNameLevel to 1.
% To extract animal name from the second path, you have to set animalNameLevel to
2.
% Third - 2, fourth - 1.
% Some scripts always use animal name in their output even if p.animalNameLevel is
set
% to 0. These scripts treat value 0 as 1.
p.animalNameLevel = 1;

% This parameter controls whether an animal name should be added to the output
folder or not.
% Possible values are 'true' or 'false'. Default is false.
% Animal name is extracted from the data path. For example, if you have data path
like this
% c:\work\recordings\hafting\120814
% then the animal name is 'hafting'.
p.addAnimalNameToOutput = true;

% Normalized threshold value used to search for peaks on an autocorrelogram.
% Ranges from 0 to 1, default value is 0.2. See also analyses.gridnessScore
p.gridnessThreshold = 0.2;

% Value of minimal difference of inner fields orientation (in degrees). If there
are fields
% that differ in orientation for less than this value, then only the closest to the
centre field are left.
% Default value is 15. See also analyses.gridnessScore
p.gridnessMinOrientation = 15;

% Number of iterations to do in the shuffling analysis. The shuffling is
% done to calculate expected values.
p.numShuffleIterations = 100;

% Shuffling is performed by making a circular shift of spikes timestamps starting
from a random point.
% Circular shift happens on top of position data. p.shuffleCircOffset defines a
valid interval for
```

```
% a starting point of the shift. If N is the time of last position sample and
p.shuffleCircOffset == 20,
% then a starting point will be a random number in interval [20 N-20]. Default
value is 20.
p.shuffleCircOffset = 20; % [sec]

% Shuffling scramble mode. Set the way the spikes are scrambled when calculating
the
% expected values.
% 'random'  Takes a real number of spikes of a cell and redistributes them randomly
across
%           the animal's path. Does it for each shuffle iteration.
p.scrambleMode = 'random';

% Table that defines what values to shuffle.
% Each line consists of 3 items:
%   <entry name>        name of the shuffling entry which is used internally in the
scripts. Do not change!
%   <description>       Description string (column name) that will be in the
resulting Excel file.
%                       Could be changed, but not recommended.
%   <shuffle flag>      TRUE or FALSE. If TRUE then shuffling of this variable will
be performed.
%                       Change to your needs.
% By default all shuffling is set to FALSE.
p.shuffleTable = {...
    'doGridnessScore', 'Gridness score', false; ...
    'doInformationContent', 'Information content [bits/spike]', true; ...
    'doBorderScore', 'Border score', true; ...
    'doHeadDirection', 'Head direction (mean vector length)', true; ...
    'doSpeedScore', 'Speed score', true; ...
    'doCoherence', 'Coherence (unsmoothed map)', true; ...
    };

% List of percentile values that should be calculated on shuffled data.
% Default value [95 99].
p.shufflePercentiles = [95 99];

p.shuffleNumBins = 50;

% Flag that specifies whether to use dual criterion (<one variable> + information
content)
% on gridness score and border score distribution. Possible values: false or true.
% Default is false.
p.shuffleGridnessDualCriterion = false;

% This parameter controls how rectangular rate maps are plotted. Rectangular rate
maps have one
% side shorter than the other side. If p.plotMapsSquare is set to true, then the
map will be extended
% to a square (based on the value of maximum side). Otherwise maps are plotted as
is.
% Default value is false.
p.plotMapsSquare = false;

% For analysis that uses EEG specifies what kind of EEG file to use. For example,
Axona
% outputs two files one with 250 Hz sampling, and another one with 4800 Hz. p.eegFs
parameter
% is used to select one of the file. You have two options:
% 1. set eegFs to a desired Fs value in Hz. Example, p.eegFs = 300. Then, the
closest match will be selected.
% 2. set eegFs to a string 'best', then the eeg file with highest sampling will be
used.
% Default value is 'best'.
p.eegFs = 'best';

% Argument for analyses.movingDirection function, [n1 n2].
```

```
% The moving direction for current sample is calculated using the mean value of
it's neighbours.
% mdwindowPoints specifies how many points will be taken before the current sample
(n1) and
% how many after (n2). Default value is [1 1], which means that the moving
direction for
% sample i is determined by samples i-1 and i+1. Note that [1 1] gives you a
histogram with
% very sharp bins at [0 90 180 270] degrees.
p.mdWindowPoints = [1 1];

% Argument for analyses.movingDirection function.
% Moving direction can be calculated not for every position sample, but for every
'mdStep' sample.
% Default is 1.
p.mdStep = 1;

% Width of a bin for speed data binning.
p.speedBinWidth = 2; % [cm/s]

% Limits of values for speed data binning. This parameter is used along with
p.speedBinWidth.
% For example, if p.speedBinLimits = [0 50] and p.speedBinWidth = 2, then
% the data is binned on range from 0 to 50 cm/s in 2 cm/s bins.
% If value [0] is provided, then the limits is extracted from the data (min and max
values).
p.speedBinLimits = [5 100]; % [cm/s]

% This parameter is used during speed rate map calculation. Minimum time an animal
% must spend in a bin, in order to include this bin in the resulting speed map.
% In other words if an animal has spent less than p.speedBinMinTime in a bin, the
value
% of this bin is set to NaN. Default value is 10, meaning that only bins in which
% animal spent more than 10 seconds are included.
% Value of 0 means that all bins matter.
p.speedBinMinTime = 0; % [sec]

% Line height for plots that use vertical lines (e.g. spike density on a linear
track).
% Could be any positive number, but practical value is somewhere between 0 and 1.
% Default value is 0.2.
p.lineHeight = 0.2;

% Axis limits for speed plots. For example, in speed vs rate plot firing rate
values lie
% along y-axis and speed values lie along x-axis. y-axis limits are [0
max(firingRate)+3].
% p.speedPlotLimits allows you to set fixed limit for x-axis. Default value ([])
uses autoscaling.
% Otherwise, you should provide both min and max value: p.speedPlotLimits = [min
max].
p.speedPlotLimits = [0 50];

% Experimental! Used during shuffling of gridness score. Number of expanding
circles taken before
% and after the radius which corresponds to gridness score for real data. Seems
% that smaller values work better. At least one number must be > 0!
p.gridShuffleRadii = [1 1];

% Defines the search zone around the border of a track.
% The value should be given in range 0.5-1. It corresponds to
% the percentage of the track length. For example, if track length is 100 cm
% and borderThreshold is 0.6 (track is zero centred), then the function
% will look for peaks in two zones: 30..50 cm and -30..-50 cm. Useful
% if animal doesn't run until the very end of the track.
% Default value is 0.6.
p.runDetectionBorderThreshold = 0.6; % [perc]
```

```
% Sometimes animal doesn't immediately run back on the track, rather
% stays at the end/beginning of the track for some time. If you don't
% want to include such activities in the final left/right runs, then set
% this property to 'on'. Otherwise set it to 'off'. Default value is 'on'.
p.runDetectionOmitEdgeActivity = 'on';

% Value of a minimum run duration in seconds. If provided, then runs that are
% shorter than this value, are discarded. Default value is 0, meaning all
% runs are stored.
p.runDetectionMinDuration = 0; % [sec]

% Value of a minimum run length in cm. If provided, then runs that
% are shorter than this value will be discarded.
% Default value is 0, meaning that all runs are kept.
p.runDetectionMinLength = 0; % [cm]

% Type of the value in p.runDetectionThreshold. Can be either '%' or 'direct'.
% '%' means that the p.runDetectionThreshold is given as percentage of track
length.
% 'direct' means that p.runDetectionThreshold has the same units as your positions
(normally cm),
% and it is the offset from track edges.
% See examples in description of p.runDetectionThreshold.
% Usage of 'direct' value might be helpfull if you have recordings on a linear
track of different
% lengths and you always want to remove exact amount of cm from your tracks.
p.runDetectionThresholdType = '%';

% The detection of runs on linear track is based on peak detection of animal's
% x-axis trajectory. This parameter controls the amount above surrounding data
% for a peak to be identified. Larger values mean the algorithm is more selective
% in finding peaks. Default value is 1, which will result in all peaks
% identification (for example if animal stops, moves backwards a bit and then
% goes forward again). Another possible value is [], which equals to (max(x0)-
min(x0))/4).
% If your runs are detected incorrectly, you can try to modify this parameter.
% Start by setting it to [].
p.runDetectionSelectivity = 1;

% The percentage of the total linear track length that will be ignored in each end
% of the track. Animal activity at the end zones of the track will not be
% included in the analyses. For example, if your linear track is 100 cm and
% p.runDetectionThreshold = 5, then runs will be detected in range -95..95 cm.
% Note! This parameter is different and independent of
p.runDetectionBorderThreshold.
% Valid range: 0 - 49.
% Default value is 5.
p.runDetectionThreshold = 5; % [perc]

% One or several thresholds to separate grids in different modules based on their
spacing.
% It's primary purpose is to colour-code dots on plot that shows distribution of
grid spacing
% and distance. If 0, then no colour-coding is used.
% If for example p.spacingModuleThresholds = [10], then all dots that have spacing
0-10 cm will
% have identical colour. Other dots (10+) will have a different colour.
% If p.spacingModuleThresholds = [10 20], then three colours will be used. One for
0-10 spacing,
% another for 10-20, and another one for 20+.
p.spacingModuleThresholds = [0]; % [cm]

% This parameter is used during analysis of prospective firing of speed cells.
% It defines the minimum and maximum offset for spikes. Spikes are shifted
% backwards and forward. For each shift a correlation between firing rate
% and speed is calculated.
% Default value is [-400 400].
p.speedProspectiveLimit_ms = [-400 400];
```

```
% This parameter is linked to p.speedProspectiveLimit_ms. It defines
% the step size for spike shift. Spikes are shifted by values defined by vector:
%
p.speedProspectiveLimit_ms(1):p.speedProspectiveBinWidth_ms:p.speedProspectiveLimit
_ms(2)
% Default value is 20.
p.speedProspectiveBinWidth_ms = 20;

% Controls the colour-scaling of a speed map plot. You can use this parameter if
you want to
% plot several speed maps with the same colour scale.
%
% Format is p.speedMapScalling = [lower_end higher_end], where both values are
given in cm/s.
% When empty ([]) or NaN, then the plot is autoscaled: the lowest value of
% the map is represented by dark blue and the highest value of the map is
represented by brown.
% Otherwise everything which is below or equal 'lower_end' value is represented by
dark blue,
% and 'higher_end' is represented by brown. It's possible to set only one value to
NaN:
% p.speedMapScalling = [NaN 15] will scale from the minimum value of the map up to
15 Hz.
% Default is p.speedMapScalling = [];, which means autoscale is used.
p.speedMapScalling = []; % cm/s

% Width of the Gaussian smoothing kernel applied to during calculation of speed
score(s).
% Smoothing of instantaneous firing rate is affected by this value.
% Default value is 400 ms.
p.speedSmoothing_sec = 0.4;

% Defines filter that is applied to position data. Possible values are:
% 'off' - no filtering is done
% 'mean' - median filter by Matlab function medfilt1. Default order is 15.
% Default is 'mean'.
p.posFilter = 'mean';
```

NTNU

Norwegian University of
Science and Technology